

# **Volumetric characterization of the nano- and microconfiguration of nanocomposites with conductive fillers by dielectric spectroscopy**

Zur Erlangung des akademischen Grades eines

DOKTORS DER INGENIEURWISSENSCHAFTEN (Dr.-Ing.)

von der KIT-Fakultät für Maschinenbau des

Karlsruher Instituts für Technologie (KIT)

angenommene

DISSERTATION

von

Dipl.-Ing- José Francisco Blanco Villalba

Tag der mündlichen Prüfung:

01.02.2021

Hauptreferent:

Prof. Dr.-Ing. Peter Elsner

Korreferent:

Prof. Dr.-Ing. habil. Kay André Weidenmann

## **DECLARATION**

---

I declare that this dissertation is the product of my own work and it has not been submitted before for any degree or examination elsewhere. All the sources and contributions to this work have been indicated or acknowledged particularly.

José Francisco Blanco Villalba

To Susana

## Acknowledgement

I have been fortunate to receive the support and guidance of many people during the course of this work. I would like to thank Susana for her invaluable love and support, and my family, that always stayed close in spite of the distance.

I would like to thank Prof. Dr.-Ing. Peter Elsner for accepting me as a doctoral candidate and supervising this work. His comments and suggestions have contributed to deepen my knowledge and improving this dissertation. I would also like to thank the members of the dissertation jury for their valuable time.

I would like to express my sincere gratitude to Dr. Christof Hübner. From the beginning, he was always ready to dedicate a great amount of time for discussion. His numerous ideas and suggestions have greatly contributed to shape this work. He had always a wise word of advice to keep the work on track and help me keep a clear vision of the ultimate goals.

I would like to thank Prof. Dr.-Ing. habil. Kay André Weidenmann for his comments and suggestions that have greatly improve this thesis.

Thanks to Hon.-Prof. Dr. Helfried Urban for his generous support. His technical discussions with Dr. Matthias Graf on the fundamentals of electromagnetism and dielectric measurements were invaluable.

Thanks to Dr. Wolfgang Menesklou, from *IAM-WET* in *KIT* for kindly providing the setup for dielectric spectroscopy. Thanks to Dr. Dirk Wilmer from Novocontrol Technologies, for sharing his expertise on instrumentation for dielectric spectroscopy and to Prof. Friedrich Kremer from the University of Leipzig and Prof. Bernhard Røling from the Philipps University of Marburg for sharing their deep knowledge on dielectric spectroscopy.

Special thanks to Carolyn Fisher for her support. Together with Dr. Christof Hübner, she managed brilliantly *TheLink*, the European Marie- Curie project in which this dissertation was framed.

I would like to thank the members of *TheLink* and their colleagues: Prof. Milo Schaffer, Dr. Hanna Leese, Sandy Fisher, Jacek Gołębowski, Miguel Matos and their colleagues in *Imperial College London*, for kindly letting me work in their labs and sharing invaluable knowledge on

nanocomposite characterization; Dr. Julio Gómez Cordón, Imanol Recio Erquicia and their colleagues in *Avanzare Innovación Tecnológica S.L.*, for kindly letting me use their facilities and sharing knowledge on graphene production and composite processing; Daniel Vlasveld, Chris de Ruijter and Rosério Valente from *Promolding BV* for providing nanocomposites and interesting discussions; Prof. Marta Ramos, Prof. Luis Marques, Miguel Jiménez Redondo, Veniero Lenzi and Stylianos Tsopanidis from the *University of Minho*, for their support and interesting discussions about composite simulations; Dr. Drik Dijkstra and Dr. Piet Driest from *Covestro / Bayer MaterialScience*, Denis Ganin from *KIT*, Christianos Stiapis and Roberto Refoyo Cabezas from the *Foundation for Research and Technology of Hellas*, Sergio Quesada from *GVS SPA*, and Ilaria Geremia from *University of Twente* for their great fellowship and collaboration.

I am glad I could share my time with numerous supportive colleagues at the Fraunhofer Institute for Chemical technologies. Hoping not to forget anyone, I would like to thank: Patrick Weiss, for his technical support, he was always ready to help; Irma Mikonsaari, her vast knowledge of technologies and network of contacts proved to be useful several times; Dr. Burak Çağlar, he provided guidance and advice in the PhD journey; Carmen Eißler and Birgit Eickershoff for their assistance in sample preparation; Melanie Klemenz, for his assistance in compounding nanocomposites; Manuel Morais and Marco Marcellan for providing epoxy nanocomposites; Robin Reidel, for his meticulous work producing reference samples; Dr. Jens Noack for kindly providing impedance measurement systems; Markus Schönwald, for his technical assistance in sample preparation; Kevin Moser, for providing invaluable advice and PLA composites; Kevin Moritz, for his assistance in microscopy; Dr. María del Mar Juez Lorenzo provided invaluable support with SEM and together with Vladi, Jorge, Giancarlo, Andrei, Jan, Ute, Claudia, Uli, Sascha, Matthias, Brenda, Nak and many others made my time at Fraunhofer more enjoyable.

This project has received funding from the European Union's Horizon 2020 research and innovation programme under the Marie Skłodowska-Curie Grant Agreement no. 642890.

## Abstract

An effective medium model (Polder/van Santen/Böttcher model or PvSB model) was considered to describe the dielectric properties of composites as a function of their filler dispersion and orientation. The model was experimentally validated using reference samples with controlled conditions of dispersion and orientation.

In addition to the PvSB model, the finite element method (FEM) was applied to simulate the dielectric properties of composites. When simulating under the special conditions assumed by the PvSB model, both simulations and model agree accurately, except for high concentrations, where both start to deviate. Special features that are ignored by the model, like the relative distance among fillers or the network formation of fillers, were simulated. Most of these features were found to have a negligible impact on the total permittivity of the composite. Only the network formation of fillers resulted in a considerable effect.

Consequently, an extension to the PvSB model (e-PvSB) was proposed to account for the contact or networking formation of the fillers in a composite. A new parameter was defined for this purpose, the network factor.

A method was proposed to use the e-PvSB model to obtain morphological information from experimental data. The method was applied to estimate, on the basis of permittivity measurements, the morphology of polymer nanocomposites with carbon nanotubes and carbon black under different conditions of dispersion and alignment.

## Zusammenfassung

Ein Effektiv-Medium-Modell (Polder/van Santen/Böttcher-Modell oder PvSB-Modell) wurde verwendet, um die dielektrischen Eigenschaften von Verbundwerkstoffen in Abhängigkeit von ihrer Füllstoffdispersion und -orientierung zu beschreiben. Das Modell wurde experimentell anhand von Referenzproben mit definiert eingestellter Dispersion und Orientierung der Füllstoffe validiert.

Neben der Verwendung des PvSB-Modells, wurde zur Simulation der dielektrischen Eigenschaften von Verbundwerkstoffen die Finite-Elemente-Methode (FEM) angewandt. Bei geringen Füllstoffkonzentrationen stimmen die Ergebnisse von Simulation und Modell sehr gut überein. Bei hohen Konzentrationen beginnen die Ergebnisse voneinander abzuweichen. Die vom PvSB Modell nicht berücksichtigten Parameter, wie der relative Abstand zwischen den Füllstoffen oder die Netzwerkbildung von Füllstoffen, wurden mit Hilfe der FEM simuliert. Es wurde festgestellt, dass die meisten dieser Parameter einen vernachlässigbaren Einfluss auf die Gesamtpermittivität des Komposits haben. Lediglich die Netzwerkbildung der Füllstoffe führte zu einem erheblichen Effekt.

Eine Erweiterung des PvSB-Modells (e-PvSB) wurde folglich vorgeschlagen, um die Kontakt- oder Netzwerkbildung der Füllstoffe in einem Komposit zu berücksichtigen. Zu diesem Zweck wurde ein neuer Parameter definiert, der Netzwerkfaktor.

Darauf aufbauend wurde eine Methode zur Verwendung des e-PvSB-Modells vorgeschlagen, um morphologische Informationen aus experimentellen Daten zu erhalten. Die Methode wurde angewandt, um anhand von Messdaten der Permittivität, die Morphologie von Polymer-Nanokompositen mit Kohlenstoff-Nanoröhren und Ruß unter verschiedenen Zuständen von Dispersion und Ausrichtung abzuschätzen.

## Table of Contents

<b>Acknowledgement</b> .....	<b>iv</b>
<b>Abstract</b> .....	<b>vi</b>
<b>Zusammenfassung</b> .....	<b>vii</b>
<b>Table of Contents</b> .....	<b>viii</b>
<b>List of Abbreviations</b> .....	<b>xi</b>
<b>List of Symbols</b> .....	<b>xii</b>
<b>1. Introduction</b> .....	<b>1</b>
1.1 Motivation and goals .....	1
1.2 Outline .....	1
<b>2. State of Research</b> .....	<b>3</b>
2.1 Fundamentals of Dielectric Spectroscopy .....	3
2.1.1 Polarization of Materials.....	3
2.1.2 Maxwell Equations .....	4
2.1.3 Mathematical Description.....	5
2.1.4 Complex Notation and Immitances .....	7
2.1.5 Polarization processes.....	8
2.1.5.1 Dipolar Fluctuations.....	9
2.1.5.2 Fluctuations of Mobile Charges.....	11
2.1.5.3 Separation of Charges: Maxwell/Wagner Polarization.....	13
2.1.5.4 Separation of Charges: Electrode Polarization .....	15
2.1.6 Reorientation of CNTs in an Electric Field .....	15
2.2 Fundamentals of Effective Medium Models .....	16
2.2.1 Mixture Rules for Composites.....	16
2.2.2 Theoretical Bounds: Voigt and Reuss Models .....	16
2.2.3 Effective Medium Models .....	18
2.2.3.1 Polder/van Santen/Böttcher (PvSB) model.....	18
2.2.4 Derivation of the PvSB Model .....	20
2.2.5 Convention for Orientation.....	24
<b>3. Experimental</b> .....	<b>27</b>
3.1 Materials .....	27
3.1.1 Multi-Walled Carbon Nanotubes.....	27
3.1.2 Single-Walled Carbon Nanotubes .....	27
3.1.3 Carbon Black .....	27
3.1.4 Polylactide .....	27
3.1.5 Epoxy.....	28



3.1.6 Wax.....	28
3.2 Production.....	28
3.2.1 Compounding of Composites from PLA with MWNT or CB ....	28
3.2.2 Sample Preparation of PLA Composites .....	29
3.2.3 Three-Roll Milling of Epoxy/SWNT Suspensions.....	30
3.2.4 Sample Preparation of Epoxy Composites .....	30
3.2.5 Reference Samples with Controlled Morphology .....	31
3.3 Characterization.....	32
3.3.1 Volume versus Mass Concentrations .....	32
3.3.1.1 Dielectric Measurements .....	33
3.3.1.2 Optimal Sample Dimensions for Dielectric Measurements....	34
3.3.1.2.1 Border Effects on Dielectric Measurements .....	34
3.3.1.2.2 Instrumental Accuracy for Conductive Samples .....	36
3.3.2 Scanning Electron Microscopy (SEM).....	37
3.3.3 Transmission Optical Microscopy (TOM) .....	37
<b>4. Modelling and Simulation of Dielectric Properties .....</b>	<b>39</b>
4.1 PvSB Model for Composites with Conductive Fillers .....	39
4.1.1 Reformulation of the PvSB Model .....	39
4.1.2 PvSB Model Simplification.....	41
4.2 Experimental Validation of the PvSB Model.....	42
4.2.1 Effect of Orientation .....	43
4.2.2 Effect of Concentration.....	44
4.2.3 Effect of Material.....	44
4.3 Simulations .....	45
4.3.1 The Finite Element Method.....	45
4.3.2 Simulating Ideal Conditions .....	46
4.3.2.1 Spherical fillers .....	46
4.3.2.2 Ellipsoidal fillers.....	47
4.3.3 Simulating Non-Ideal Features .....	49
4.3.3.1 Gap between Fillers .....	49
4.3.3.2 Distance to Electrodes.....	50
4.3.3.3 Number of Layers .....	52
4.3.3.4 Curvature.....	53
4.3.3.5 Network of Fillers .....	55
4.3.3.5.1 Agglomerates of Spherical Particles .....	55
4.3.3.5.2 Chains of Ellipsoidal Fillers.....	57
4.4 Extended PvSB Model (e-PvSB).....	58
4.5 Method to Obtain Morphological Information from Experimental Data	63
4.5.1 Method Applied to Simulated Composites.....	65

4.5.1.1	Spherical Fillers with Varying Degrees of Dispersion .....	65
4.5.1.2	Reference Network Factor .....	68
4.5.1.3	Ellipsoidal Fillers with Varying Degrees of Alignment .....	69
4.6	Discussion.....	72
<b>5.</b>	<b>Analysis of dispersion.....</b>	<b>75</b>
5.1	Nanocomposites .....	75
5.2	Microscopy .....	75
5.2.1	Scanning Electron Microscopy .....	75
5.2.1.1	PLA/MWNT Composites .....	75
5.2.1.2	PLA/CB Composites.....	76
5.2.2	Transmission Optical Microscopy .....	77
5.2.2.1	PLA/MWNT Composites .....	77
5.2.2.2	PLA/CB Composites.....	78
5.3	Dielectric Spectroscopy .....	79
5.3.1	Dielectric Spectra.....	80
5.3.2	Permittivity versus Concentration .....	80
5.3.3	Analysis with e-PvSB Model.....	82
5.3.3.1	PLA/MWNT Composites .....	82
5.3.3.2	PLA/CB Composites.....	83
5.4	Discussion.....	85
<b>6.</b>	<b>Analysis of Alignment .....</b>	<b>87</b>
6.1	Nanocomposites .....	87
6.2	In-situ Characterization .....	87
6.2.1	Monitorization of the Electric Treatment .....	87
6.2.2	Monitorization of the curing process .....	88
6.3	Ex-situ characterization .....	90
6.4	Analysis with e-PvSB Model .....	92
6.5	Discussion.....	95
<b>7.</b>	<b>Conclusions.....</b>	<b>97</b>
	<b>References .....</b>	<b>99</b>
	<b>List of Publications.....</b>	<b>111</b>
	<b>Appendix A: Proof of the Multiplicity of Solutions in the Regression Analysis on the e-PvSB Model.....</b>	<b>112</b>
	<b>Appendix B: Matrices of Coefficients of Determination .....</b>	<b>114</b>
	<b>Appendix C: Conductivity Spectra of Epoxy Composites.....</b>	<b>118</b>
	<b>List of Figures .....</b>	<b>119</b>
	<b>List of Tables.....</b>	<b>127</b>

## List of Abbreviations

AC	Alternating current
AFM	Atomic force microscopy
CB	Carbon black
CNTs	Carbon nanotubes
DC	Direct current
EHT	Extra high tension or accelerating tension
e-PvSB	Extended Polder/van Santen/Böttcher model
FEM	Finite element method
MFI	Melting flow index
MWNT	Multi-walled carbon nanotubes
MWS	Maxwell/Wagner/Sillars model
PLA	Poly lactide
PLLA	Poly-L-lactide
PvSB	Polder/van Santen/Böttcher model
SWNT	Single-walled carbon nanotubes
TEM	Transmission electron microscopy
TGA	Thermogravimetric analysis
TOM	Transmission optical microscopy

## List of Symbols

$A$	Area of electrodes
$a$	Alignment parameter
$a_a$	Alignment parameter of agglomerates
$a_f$	Alignment parameter of fillers
$A_{a\parallel}$	Depolarization factor of the agglomerates parallel to the electric field
$A_{a\perp}$	Depolarization factor of the agglomerates perpendicular to the electric field
$a_{C-C}$	Distance between carbon atoms
$A_J$	Empirical parameter for the Jonscher function
$A_k$	Depolarization factor of the filler in the $k$ direction
$A_n$	Depolarization factor of the equivalent ellipsoid of the network, parallel to the electric field
$AR_{eell}$	Aspect ratio of the equivalent ellipsoid parallel to the electric field
$AR_f$	Aspect ratio of the filler
$\mathbf{B}$	Magnetic induction field
$C^*$	Complex capacitance
$C_0$	Capacity of empty space
$F_n$	Network factor
$d$	Dispersion: volume fraction of fillers that are isolated in the matrix
$\mathbf{D}$	Dielectric displacement field
$D_{CNT}$	Average diameter of the CNTs

---

$D_e$	Diameter of electrode
$d_e$	Distance between electrodes
$D_i$	Depth of the layer $i$
$\bar{E}$	Effective electric field
$E$	Electric field
$\bar{E}_i$	Mean electric field inside a particle
$e_o$	Eccentricity of an oblate ellipsoid
$e_p$	Eccentricity of a prolate ellipsoid
$f$	Frequency
$H$	Magnetic field
$I$	Intensity of current
$I_0$	Amplitude of sinusoidal intensity of current
$j$	Current density
$L_{CNT}$	Average length of the CNTs
$M^*$	Electric modulus function
$m_a$	Atomic mass of carbon
$m_{CNT}$	Average mass of CNTs
$N$	Number of layers in CNTs
$P$	Polarization
$R^2$	Coefficient of determination
$s$	Empirical parameter for the Jonscher function

---

$S_{tot}$	Total surface of layers
$t$	Time
$t_e$	Thickness of the electrodes
$U$	Voltage
$U_0$	Amplitude of sinusoidal voltage
$V$	Volume
$V_{CNT}$	Average volume of CNTs
$w$	Mass concentration
$\bar{y}$	Average of observed values
$Y'$	Real part of the admittance or conductance
$Y''$	Imaginary part of the admittance or susceptance
$\hat{y}_i$	Predictions of the model
$y_i$	Experimentally observed values
$Z'(\omega)$	Real part of the impedance or resistance
$Z''(\omega)$	Imaginary part of the impedance or reactance
$\alpha$	Curvature angle
$\alpha$	Tensor of proportionality for the effective electric field
$\beta$	Empirical parameter that accounts for the symmetrical broadening of the complex dielectric function
$\gamma$	Empirical parameter that accounts for the non-symmetrical broadening of the complex dielectric function
$\delta$	Distance between layers in CNTs

---

$\Delta\varepsilon$	Dielectric strength
$\bar{\varepsilon}$	Effective relative permittivity of a composite
$\varepsilon^*$	Complex dielectric function
$\varepsilon'$	Real part of the complex dielectric function
$\varepsilon''$	Imaginary part of the complex dielectric function or dielectric loss
$\varepsilon_0$	Permittivity of empty space
$\varepsilon_\infty$	Relative permittivity at the high frequency limit
$\varepsilon_a$	Relative permittivity of agglomerates
$\varepsilon_f$	Relative permittivity of the filler
$\varepsilon_m$	Relative permittivity of the matrix
$\varepsilon_s$	Static relative permittivity
$\lambda$	Parameter describing the fractal nature of a process
$\mu$	Conversion factor for immitances
$\nu$	Volume concentration of fillers
$\nu_a$	Volume concentration of fillers in agglomerates
$\nu_f$	Volume concentration of dispersed fillers
$\rho_{CNT}$	Average density of CNTs
$\rho_e$	Density of charges
$\rho_{filler}$	Density of the filler
$\rho_{polymer}$	Density of the polymer
$\sigma^*$	Complex conductivity

---

$\sigma_C$	Surface density of carbon
$\sigma_{DC}$	DC conductivity
$\tau$	Time constant
$\tau_D$	Debye relaxation time
$\tau_{MW}$	Relaxation time of the Maxwell/Wagner interfacial polarization
$\chi^*$	Complex susceptibility
$\omega$	Angular frequency
$\omega_C$	Critical frequency



# 1. Introduction

## 1.1 Motivation and goals

The extraordinary electrical and mechanical properties of nanomaterials like carbon nanotubes (CNTs) or graphene make them prime candidates for the development of new nanocomposite materials with applications in a wide range of industries [1]–[5].

The use of CNTs as high strength, high conductivity, thermoplastic polymer reinforcements has been widely reported [6]–[12]. However, the challenge of achieving a good dispersion of CNTs in polymeric matrices (due to their tendency to agglomerate) must be overcome in order to fully exploit their potential use in such applications.

The relationship among processing parameters, achieved nanostructure and resulting properties of polymer nanocomposites is so far not fully understood [13], [14]. Dielectric spectroscopy is a promising volumetric technique to characterise the nanoparticle distribution of polymer nanocomposites in industrial environments, as it can be used in a fast and non-destructive way, unlike high resolution characterisation techniques, like atomic force microscopy [15] or electron microscopy [16].

In this thesis, dielectric spectroscopy is explored as a tool to characterize polymer nanocomposites with conductive fillers. The experimental requirements and limitations of this technique are discussed. A method based on effective medium models is proposed to obtain information about the distribution of nanoparticles in polymer composites.

## 1.2 Outline

In chapter 2, the fundamentals of dielectric spectroscopy and effective medium models applied to composites are explained. The materials, as well as the fabrication and characterization techniques used in this thesis are described in chapter 3. Chapter 4 proposes an effective medium model to predict the electrical properties of polymer nanocomposites with conductive fillers and provides a method to obtain morphological information from them. In chapters 5 and 6, this method is applied to experimental data of composites with different degrees of dispersion and alignment, respectively.



## 2. State of Research

### 2.1 Fundamentals of Dielectric Spectroscopy

#### 2.1.1 Polarization of Materials

Dielectric spectroscopy (also known as impedance spectroscopy) is a characterization technique in which an alternating electric field is applied to a material. The material's response at different frequencies provides information of its internal structure.

When an external electric field is applied to a material, there are several mechanisms through which it can react to it, creating an internal electric field opposing the external one. Some of these mechanisms are [17]:

- **Electronic displacement:** The electronic orbitals around atomic nuclei are distorted, so that atoms obtain a dipole moment.
- **Ionic displacement:** The relative position of anions and cations in a crystalline structure changes.
- **Dipole orientation:** Molecules or functional groups with a dipole moment get aligned or partially aligned to the electric field.
- **Charge migration:** Mobile charges (ions, electrons) in the material migrate in the direction of the electric field.

Each of these mechanisms have a characteristic time scale, i.e., their effect on the material is dependent on the frequency of the external electric field. Nowadays, dielectric spectroscopy measurements can be performed between  $10^{-6}$  and  $10^{12}$  Hz, for which it is often known as broadband dielectric spectroscopy [18], [19].

When an internal electric field is generated opposing the external electric field, the material is effectively storing energy. A measure of how much energy the material can store is permittivity (also known as dielectric constant), which directly depends on the mechanisms previously described. The frequency dependence of the permittivity of a material can be explained as follows (see Figure 1). At low frequencies, all the mechanisms contribute to the permittivity of the material. When the frequency is increased, the slower mechanisms can no longer follow the electric field and they stop storing energy, thus decreasing permittivity. Eventually, at a high

enough frequency, all mechanisms will be unable to follow the electric field and the permittivity of empty space will remain.

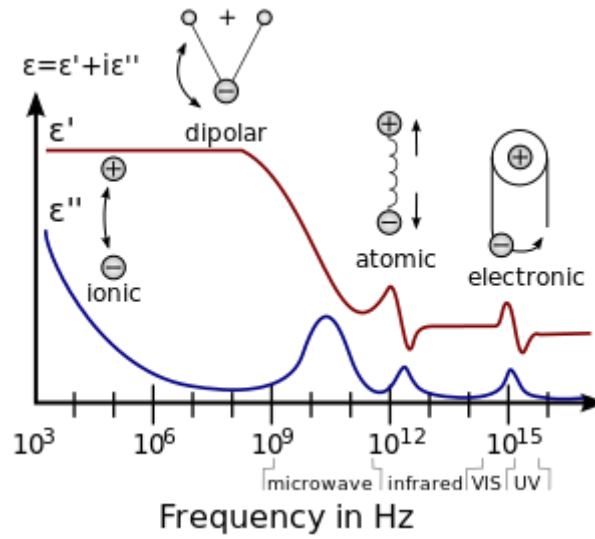


Figure 1. Characteristic frequency dependence of the real (red) and imaginary (blue) parts of permittivity for different dielectric mechanisms. (Reproduced from [20]).

### 2.1.2 Maxwell Equations

Maxwell equations (2-1 to 2-4) must be considered to study the interaction of a material with an electric field:

$$\nabla \times \mathbf{E} = -\frac{\partial \mathbf{B}}{\partial t} \quad 2-1$$

$$\nabla \times \mathbf{H} = \mathbf{j} + \frac{\partial \mathbf{D}}{\partial t} \quad 2-2$$

$$\nabla \cdot \mathbf{D} = \rho_e \quad 2-3$$

$$\nabla \cdot \mathbf{B} = 0 \quad 2-4$$

Where  $\mathbf{E}$  is the electric field,  $\mathbf{B}$  the magnetic induction,  $\mathbf{H}$  the magnetic field,  $\mathbf{j}$  the current density and  $\rho_e$  the density of charges.

The dielectric displacement ( $\mathbf{D}$ ) is defined as:

$$\mathbf{D} = \varepsilon^* \varepsilon_0 \mathbf{E} \quad 2-5$$

Where  $\varepsilon_0$  is the permittivity of empty space and  $\varepsilon^*$  is the complex dielectric function or relative permittivity. The relative permittivity is a frequency-dependent magnitude, as described in section 2.1.3. In general,  $\varepsilon^*$  is a tensor ( $\mathbf{D}$  and  $\mathbf{E}$  are vectors), but in this thesis it will be considered as a scalar magnitude for the sake of simplicity.

### 2.1.3 Mathematical Description

In dielectric spectroscopy, samples are typically excited with a sinusoidal signal, i.e., an alternating voltage<sup>1</sup> is applied:

$$U(\omega, t) = U_0 \cos(\omega t) \quad 2-6$$

$U(\omega, t)$  is the applied voltage at time  $t$ ,  $U_0$  is the amplitude of the signal and  $\omega$  is the angular frequency, related to frequency ( $f$ ) by  $\omega = 2\pi f$ .

In some cases, considering electric field and polarization as input and output, instead of voltage and electric current, respectively, is mathematically more convenient (see Table 1).

The response of the material produces, for linear, causal, time-invariant systems, a sinusoidal electric current, with the same frequency but a different amplitude ( $I_0$ ) and phase ( $\phi$ ):

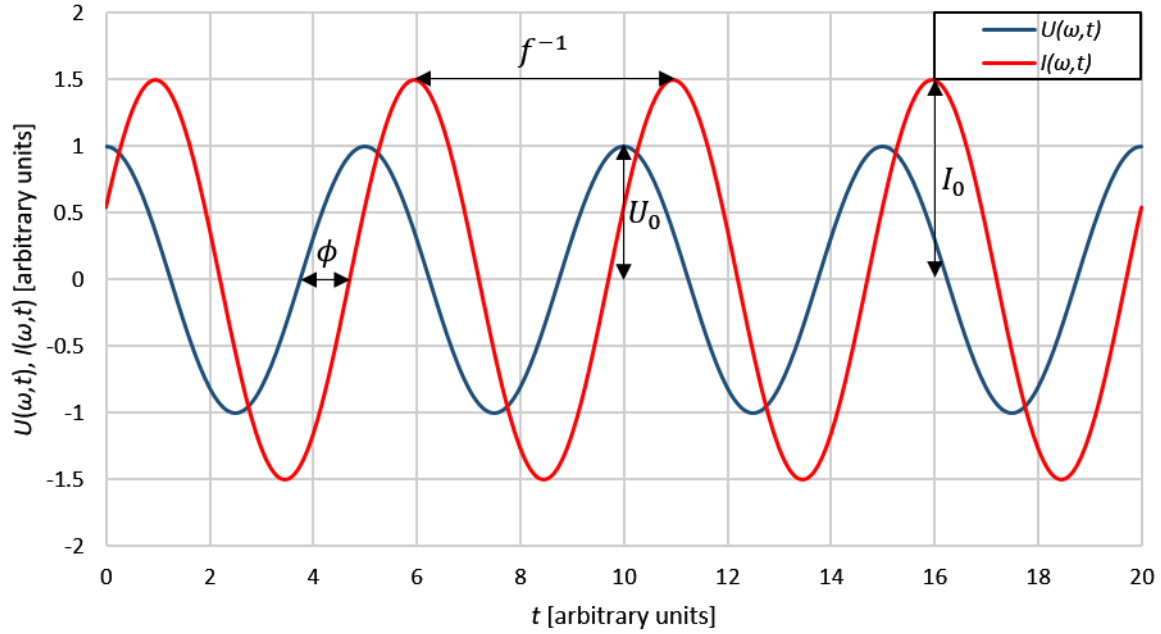
$$I(\omega, t) = I_0 \cos(\omega t - \phi) \quad 2-7$$

Most materials behave linearly, or can at least be treated as linear, when applying small excitation signals (lower than the thermal voltage,  $\sim 25$  mV at  $25$  °C [21]).

In Figure 2, sinusoidal input and output signals (voltage and current, respectively) are shown versus time. The phase difference,  $\phi$ , the period or inverse of frequency,  $f^{-1}$ , as well as the wave amplitudes,  $I_0$  and  $U_0$ , are indicated.

---

<sup>1</sup> From now on, we will consider an applied voltage in a single direction. Therefore, the electric field, permittivity and other tensors will be simplified to scalars.



**Figure 2.** Sinusoidal input and output signals (voltage and current, respectively) versus time. The amplitudes ( $U_0$ ,  $I_0$ ), phase difference ( $\phi$ ) and period or inverse of frequency ( $f^{-1}$ ) are indicated.

It must be noted how the mathematical treatment of dielectric (or impedance) spectroscopy is analogous to those of other properties, as shown in Table 1.

**Table 1.** Comparison of different experimental methods in the frame of the linear response theory [22].

Type of experiment	Disturbance $x(t)$	Response $y(t)$	Compliance $\tilde{J}(\tau)$ or $J^*(\omega)$	Modulus $\tilde{G}(\tau)$ or $G^*(\omega)$
Dielectric	Electric field $\mathbf{E}$	Polarization $\mathbf{P}$	Dielectric susceptibility $\chi^*(\omega) = (\varepsilon^*(\omega) - 1)$	Electric modulus $M^*(\omega)$
Mechanical shear	Shear tension $\sigma$	Shear angle	Shear compliance $J(t)$	Shear modulus $G(t)$
Isotropic compression	Pressure $p$	Volume $V$	Volume compliance $B(t) V$	Compression modulus $K(t)$
Magnetic	Magnetic field $\mathbf{H}$	Magnetization $\mathbf{M}$	Magnetic susceptibility $\mu^*(\omega) - 1$	-
Temperature change	Temperature $T$	Entropy $S$	Entropy compliance $J_s(t)$	Temperature modulus $G_T(t)$

### 2.1.4 Complex Notation and Immitances

For linear, causal, time-invariant systems, the response to a sinusoidal input can be characterized by two magnitudes: the change in amplitude and the change in phase of the response with respect to the input. Therefore, it is mathematically convenient to express voltage and electric current as complex numbers:

$$U^*(\omega) = U_0 e^{i\omega t} \quad 2-8$$

$$I^*(\omega) = I_0 e^{i\omega t} \quad 2-9$$

Impedance is defined as a complex number, similar to the resistance in the Ohm's law:

$$Z^*(\omega) = \frac{U^*(\omega)}{I^*(\omega)} = Z'(\omega) + iZ''(\omega) \quad 2-10$$

Where  $Z'(\omega)$  is the real part of the impedance or resistance and  $Z''(\omega)$  is the imaginary part of the impedance or reactance<sup>2</sup>.

Admittance is defined as:

$$Y^*(\omega) = \frac{1}{Z^*(\omega)} = Y'(\omega) + iY''(\omega) \quad 2-11$$

Where  $Y'(\omega)$  is the real part of the admittance or conductance and  $Y''(\omega)$  is the imaginary part of the admittance or susceptance. The complex conductivity  $\sigma^*(\omega)$  is connected with the admittance by the sample geometry (for a parallel plate capacitor with distance between electrodes ( $d_e$ ) and area ( $A$ )):

$$\sigma^*(\omega) = Y^*(\omega) \frac{d_e}{A} \quad 2-12$$

The complex dielectric function or relative permittivity, defined in section 2.1.2, is related to impedance through the expression:

---

<sup>2</sup> Reactance is sometimes defined as  $-Z''$ , so that it is positive for capacitive systems.

$$\varepsilon^*(\omega) = \frac{1}{\mu Z^*(\omega)} = \varepsilon' - j\omega\varepsilon'' \quad 2-13$$

Where  $\mu = j\omega C_0$ , with  $C_0$  the capacity of empty space ( $C_0 = \varepsilon_0 \frac{A}{d_e}$  for a parallel plate capacitor, with  $\varepsilon_0$  the permittivity of empty space). The complex capacitance  $C^*(\omega)$  is connected to the permittivity through the geometry of the sample:  $\frac{d_e}{A}$ .

While the real part of the complex dielectric function ( $\varepsilon'$ ) is a measure of how much energy a material stores in form of dielectric displacement, the imaginary part ( $\varepsilon''$ , dielectric loss) is a measure of how much energy is dissipated through electric currents.

The electric modulus function ( $M^*(\omega)$ ) is defined as the inverse of the complex permittivity.

The complex functions previously defined are generically called immittances. In Table 2, the relationship among the four basic immittance functions is shown.

**Table 2. Relationship among the four basic immittance functions.  $\mu = j\omega C_0$  with  $C_0$  (empty dielectric cell's capacitance) =  $\varepsilon_0 A/d_e$  for a parallel plate capacitor with distance between electrodes  $d_e$  and area  $A$ .**

Function	$Z^*$	$Y^*$	$\varepsilon^*$	$M^*$
$Z^*$	$Z^*$	$Y^{*-1}$	$\mu^{-1}\varepsilon^{*-1}$	$\mu^{-1}M^*$
$Y^*$	$Z^{*-1}$	$Y^*$	$\mu\varepsilon^*$	$\mu M^{*-1}$
$\varepsilon^*$	$\mu^{-1}Z^{*-1}$	$\mu^{-1}Y^*$	$\varepsilon^*$	$M^{*-1}$
$M^*$	$\mu Z^*$	$\mu Y^{*-1}$	$\varepsilon^{*-1}$	$M^*$

### 2.1.5 Polarization processes

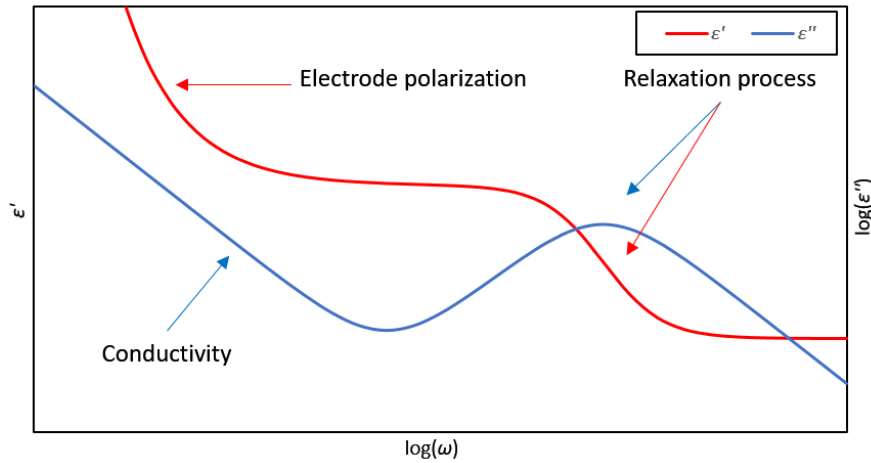
Different processes contribute to the complex permittivity of a material [23]:

- **Molecular dipolar fluctuations**, known as relaxation processes. They take place, for example, in polymers (the effect is measurable when dipolar functional groups are present), at temperatures close to the glass transition temperature, when the polymer chains have enough mobility to move in response to the electric field.
- **Migration of mobile charges**, such as electrons, holes or ions.
- **Separation of charges in an interphase**, giving rise to additional polarization. It may happen at internal interphases (known as mesoscopic polarization or Maxwell/Wagner polarization) or at the surface where the material contacts the electrodes (known as macroscopic polarization). Separation of charges are especially important in



inhomogeneous materials, like composites, phase separated polymers or crystalline polymers [24].

Each process has different characteristic effects on the complex permittivity, which are shown in Figure 3 and will be briefly discussed in the next sections.



**Figure 3. Real (blue) and imaginary (red) part of permittivity as a function of angular frequency for a material featuring electrode polarization, conductivity and a relaxation process.**

### 2.1.5.1 Dipolar Fluctuations

Relaxation processes produce a step-like function in the real part ( $\epsilon'$ ) and a peak in the imaginary part ( $\epsilon''$ ) of the complex dielectric function.

Relaxation processes can be mathematically described by the Debye model, that assumes that rigid dipoles, which do not interact with each other, are located in a viscous media, subjected to random forces [25]–[27]:

$$\epsilon^*(\omega) = \epsilon_\infty + \frac{\Delta\epsilon}{1 + i\omega\tau_D} \quad 2-14$$

With  $\tau_D$  the Debye relaxation time. The dielectric strength ( $\Delta\epsilon$ ) is defined in terms of the static permittivity ( $\epsilon_s$ ) and the permittivity at the high frequency limit ( $\epsilon_\infty$ ):

$$\Delta\epsilon = \epsilon_s - \epsilon_\infty \quad 2-15$$

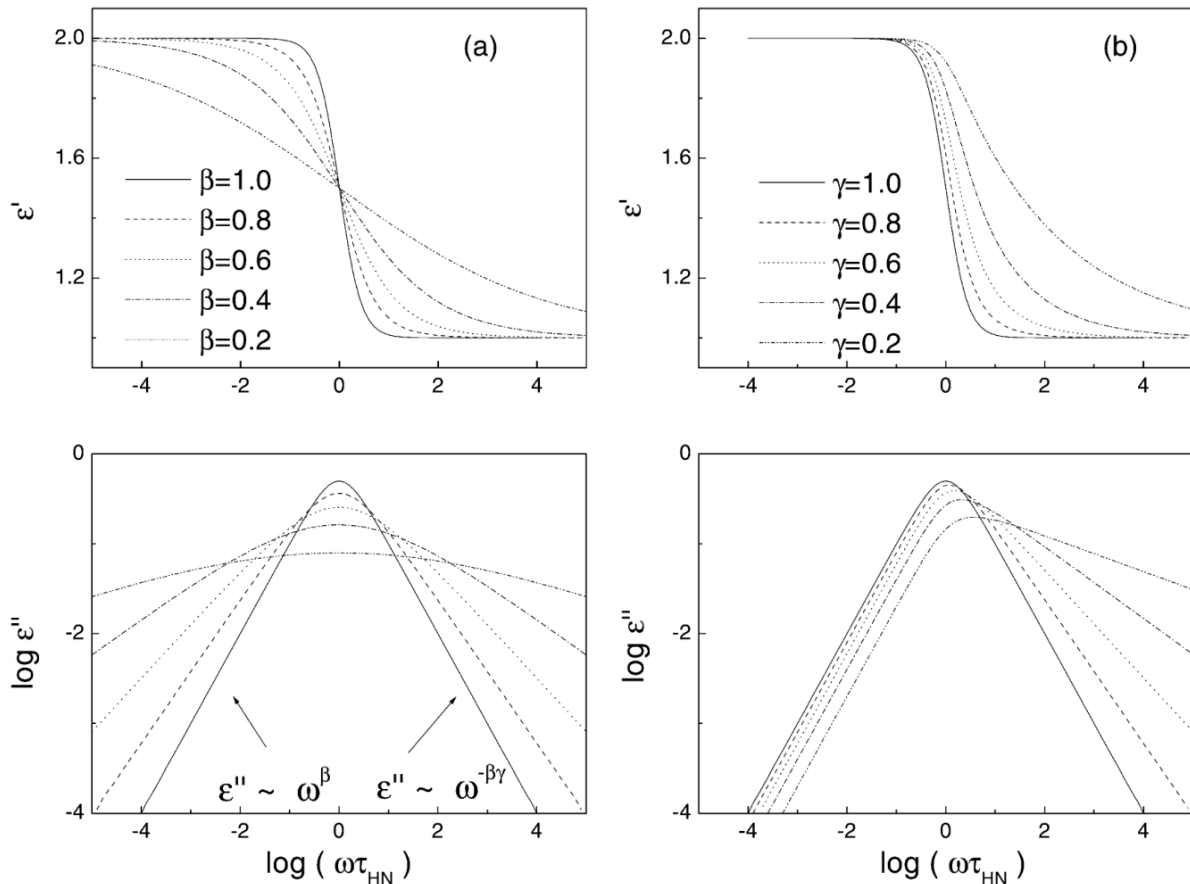
$$\epsilon_s = \lim_{\omega\tau_D \ll 1} \epsilon'(\omega)$$

$$\varepsilon_{\infty} = \lim_{\omega\tau_D \gg 1} \varepsilon'(\omega)$$

Most materials do not follow a perfect Debye behaviour, in which  $\log(\varepsilon'')$  features a symmetrical peak versus  $\log(\omega)$  as shown in Figure 4. Empirical functions have been proposed to account for the discrepancies with experimental data (Cole/Cole function [28], the Cole/Davison [29], [30] or the Fuoss/Kirkwood [31] function). The Havriliak-Negami function [32], [33] is one of the most broadly used and is a combination of the Cole/Cole and Cole/Davidson functions:

$$\varepsilon_{HN}^*(\omega) = \varepsilon_{\infty} + \frac{\Delta\varepsilon}{(1 + (i\omega\tau_{HN})^{\beta})^{\gamma}} \quad 2-16$$

Where  $\beta$  and  $\gamma$  are empirical parameters that account for the symmetrical and non-symmetrical broadening of the complex dielectric functions, respectively, and are bounded by  $\beta > 0$  and  $\beta\gamma \leq 1$ .



**Figure 4. Complex dielectric permittivity for the Havriliak-Negami function with: (a)  $\gamma = 1$ ; (b)  $\beta = 1$  ( $\tau_{HN} = 1$  [s],  $\Delta\varepsilon = 1$ ,  $\varepsilon_{\infty} = 1$ ). Reproduced from [23].**

It has been reported that dielectric relaxation can be used to study the interphase filler/matrix in polymer nanocomposites [34]–[37]. The amorphous phase of polymers with polar functional groups presents a relaxation process close to its glass transition temperature [38]–[44], when the polymer chains have enough mobility to move in response to the electric field. Some fillers may restrict the mobility of those chains and thus suppress the relaxation process in the regions of the amorphous phase around the filler. This would allow the quantification of the amount of interphase between the amorphous phase and the filler through the dielectric strength ( $\Delta\varepsilon$ ) of the relaxation process. It was a goal of this thesis to reproduce these results to develop a technique to quantify the degree of dispersion of nanofillers in a polymer matrix. Experiments were made with polylactide and carbon nanotubes, but the results disagreed with the abovementioned theory, making it unhelpful for the quantification of dispersion. This approach was therefore abandoned in favour of the effective medium approach, that allows a quantitative description of the dielectric properties of a composite (in any matrix, not only amorphous polymers with polar functional groups) based on its morphological characteristics (see section 2.2).

### 2.1.5.2 Fluctuations of Mobile Charges

The complex conductivity and the complex dielectric function are related through:

$$\sigma^*(\omega) = \sigma'(\omega) + i\sigma''(\omega) = i\omega\varepsilon_0\varepsilon^*(\omega) \quad 2-17$$

And therefore:

$$\sigma'(\omega) = \omega\varepsilon_0\varepsilon''(\omega) \quad 2-18$$

$$\sigma''(\omega) = \omega\varepsilon_0\varepsilon'(\omega) \quad 2-19$$

For a pure ohmic conductor ( $\sigma^* = \sigma_0$ ), only the imaginary part is non-zero:

$$\varepsilon''(\omega) = \frac{\sigma_{DC}}{\varepsilon_0\omega} \quad 2-20$$

Therefore, the imaginary part of permittivity of a pure ohmic conductor features a straight line (with slope -1) in the plot of  $\log(\varepsilon'')$  versus  $\log(\omega)$ , as represented in Figure 5.

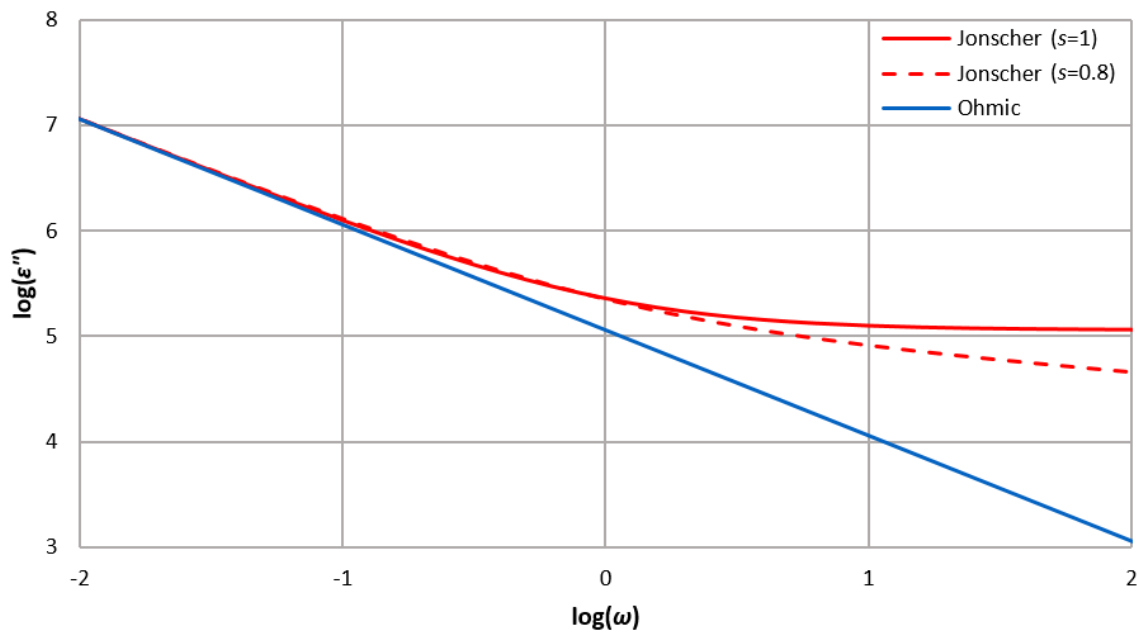
Real conductors feature a different behaviour, which is often described using the empirical Jonscher function [45], [46]:

$$\sigma'(\omega) = \sigma_{DC} + A_J \omega^s = \sigma_{DC} [1 + (\omega\tau)^s] \quad 2-21$$

Where  $\tau$  is a time constant, while  $A_J$  and  $s$  are empirical parameters. For  $\omega \gg 1/\tau$ , a power law is obtained, with  $(0 < s \leq 1)$ . For  $\omega \ll 1/\tau$ , the DC conductivity,  $\sigma_{DC}$ , remains. Jonscher law fits relatively well experimental data [47]–[49], is not based on any physical interpretation.

It features a constant DC conductivity at low frequencies, and a frequency-increasing conductivity at high frequencies, or alternatively, a high frequency plateau and a low frequency constant slope for  $\epsilon''$ , as shown in Figure 5. The critical frequency ( $\omega_c$ ), which separates both regimes, is known to be proportional to the DC conductivity of the material through the Barton/Nakajima/Namikawa relationship [50]–[52]:

$$\omega_c \sim \sigma_{DC} \quad 2-22$$

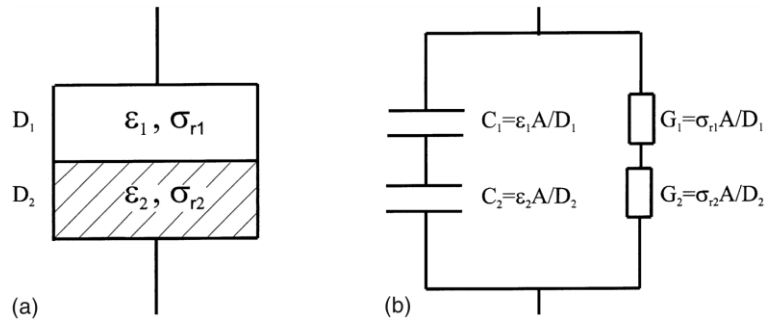


**Figure 5. Imaginary part of permittivity ( $\epsilon''$ ) for Jonscher processes with  $s = 1$  and  $s = 0.8$  and an ohmic process (equivalent to a Jonscher process with  $s = 0$ ).**

### 2.1.5.3 Separation of Charges: Maxwell/Wagner Polarization

When mobile charges get blocked at the internal phase boundaries within a material, a polarization (known as Maxwell/Wagner polarization or mesoscopic polarization) takes place. This polarization produces a strong increase in permittivity at low frequencies.

The simplest case of Maxwell/Wagner polarization is one in which two layers of different materials are in contact (see Figure 6(a)). Both materials are assumed to have frequency-independent conductivity and permittivity. This case will provide insight into other more complex cases and prove that the combination of two materials with frequency-independent properties can produce a composite with frequency-dependent properties.



**Figure 6. (a) Two layers of different materials in series, with  $\epsilon_i$  and  $\sigma_{ri}$  their permittivity and conductivity, respectively. (b) Equivalent circuit, with:  $C_i$ , capacity;  $G_i$ , conductance;  $A$ , area of the electrodes;  $D_i$ , depth of the layer  $i$ . Reproduced from [23].**

The effective properties of the composite can be determined by considering the series connection of both materials, as depicted in the circuit in Figure 6(b). The effective permittivity of the composite ( $\bar{\epsilon}(\omega)$ ) can be proved to be:

$$\bar{\epsilon}(\omega) = \bar{\epsilon}_\infty + \frac{\Delta\bar{\epsilon}}{1 + i\omega\tau_{MW}} \quad 2-23$$

For  $D_1 = D_2$  it holds:

$$\bar{\epsilon}_\infty = \frac{\epsilon_1 \epsilon_2}{\epsilon_1 + \epsilon_2} \quad 2-24$$

$$\Delta\bar{\epsilon} = \frac{\epsilon_2 \sigma_{r1} + \epsilon_1 \sigma_{r2}}{(\sigma_{r1} + \sigma_{r2})^2 (\epsilon_1 + \epsilon_2)}. \quad 2-25$$

The relaxation time  $\tau_{MW}$  of the interfacial polarization is:

$$\tau_{MW} = \varepsilon_0 \frac{\varepsilon_1 + \varepsilon_2}{\sigma_{r1} + \sigma_{r2}}. \quad 2-26$$

It must be noted how equation 2-23 has identical shape to equation 2-14 from the Debye model, describing a relaxation process. However, the nature of the process and the physical meaning of the terms in the equation are completely different.

According to equation 2-26, the critical frequency ( $1/\tau_{MW}$ ) will increase with the conductivity of the materials. Or, in other words, the higher the conductivity, the higher the characteristic frequency of the polarization process.

A more complex model of the Maxwell/Wagner polarization is the Maxwell/Wagner/Sillars (MWS) model [53]–[55]. This model assumes spherical particles of a material embedded in a matrix of a second material (see Figure 7).

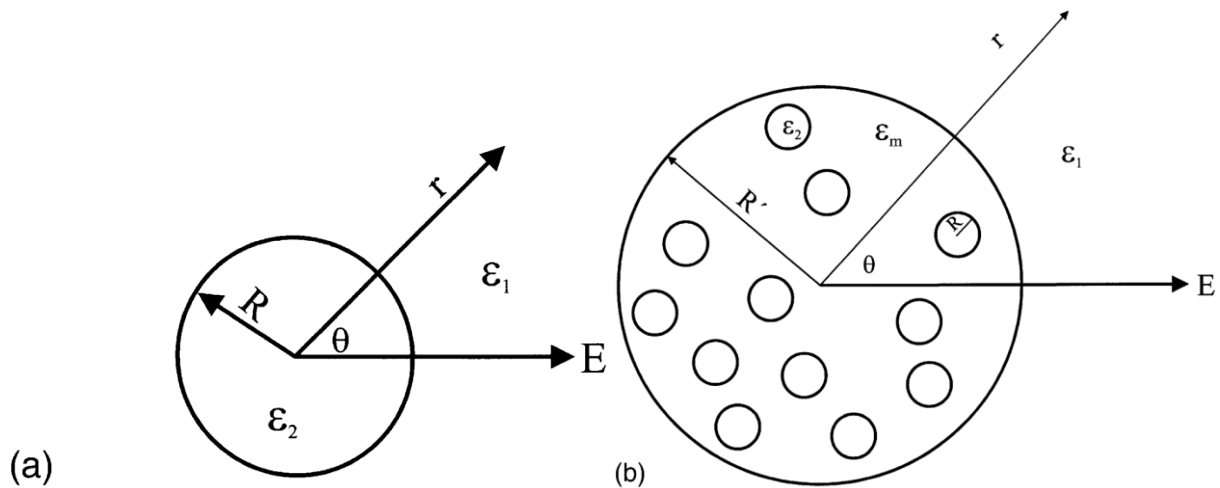


Figure 7. (a) Spherical particle to derive Maxwell's equations for a suspension. (b) Model to derive the mixture equations. The small particles are the same as sketched in (a). Reproduced from [23].

The effective permittivity of the composite according to the MWS model is:

$$\varepsilon_{WMS} = \varepsilon_1 \frac{(2\varepsilon_1 + \varepsilon_2) - 2\nu(\varepsilon_1 - \varepsilon_2)}{(2\varepsilon_1 + \varepsilon_2) + 2\nu(\varepsilon_1 - \varepsilon_2)} \quad 2-27$$

Where  $\nu$  is the volume fraction of the particles.

Equation 2-27 holds only for low concentrations. Moreover, it only considers the real part of permittivity and cannot describe shapes different than perfect spheres. To overcome these

limitations, different modifications of these models have been proposed [24], [56]–[61]. In section 2.2.3.1, a model that is especially useful to describe the composites considered in this thesis is presented.

#### 2.1.5.4 Separation of Charges: Electrode Polarization

Electrode polarization is an undesired process that can hide the real properties of a material. It may happen with moderately or highly conductive samples. A good electrode/sample contact is critical to avoid these effects, as mentioned in section 3.3.1.1.

Electrode polarization affects the low-frequency region of the spectra. Its magnitude and frequency dependency of this polarization depends on the conductivity of the sample. This polarization can produce huge values of  $\varepsilon'$  and  $\varepsilon''$ . The effect of the polarization is often several orders of magnitude higher than the real permittivity of the material, making it rarely possible to correct the measurements with any mathematical procedure, such as the model described hereunder.

Electrode surfaces have a fractal nature [62]. The following fractal power law has been found to describe the electrode polarization:

$$\varepsilon'_{EP}(\omega) - \varepsilon_s = A\omega^{-\lambda} \quad 2-28$$

$$\varepsilon''_{EP}(\omega) \sim \omega^{-\lambda} \quad 2-29$$

$$\omega > \frac{1}{\tau_{EP}}, 0 < \lambda \leq 1 \quad 2-30$$

Where  $\lambda$  ( $0 < \lambda \leq 1$ ) is a parameter describing the fractal nature of the process and  $\varepsilon_s$  is the static permittivity, due to the orientational polarization [23].

#### 2.1.6 Reorientation of CNTs in an Electric Field

It has been reported [63]–[72] that applying an AC electric field to CNTs in a fluid with a relatively low viscosity leads to a reorientation of the CNTs, as well as to the formation of new contacts among CNTs due to electrophoretic effects. Based on this, an aligning network-forming process (described in section 3.2.4) was applied to produce epoxy/CNT composites with a certain degree of alignment (see chapter 6).

## 2.2 Fundamentals of Effective Medium Models

Effective medium models are a type of extended mixture rule for composite materials. In the following sections, the fundamentals of effective medium models will be presented. An effective medium model will be proposed to predict the permittivity of composites with conductive fillers in a non-conductive matrix.

### 2.2.1 Mixture Rules for Composites

Mixture rules describe the macroscopic or effective properties of a composite material as a function of:

- The properties of each component
- The volume fraction of each component
- The geometric configuration of the composite

Theoretical and empirical mixture rules have been proposed for different properties, like permittivity, electrical conductivity [73]–[78], thermal conductivity [79]–[82], or elastic modulus [83]–[86]. Some of these models are specific for a property, while others are generic and can be used for several properties, due to the analogous mathematical treatment of different systems (see Table 1 in section 2.1.4).

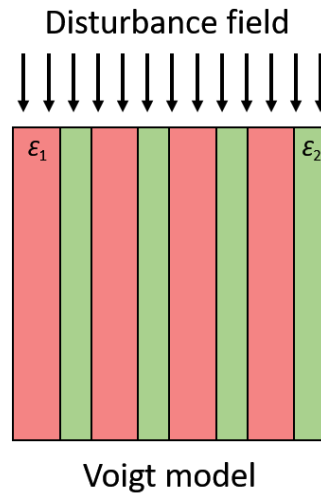
### 2.2.2 Theoretical Bounds: Voigt and Reuss Models

Every mixture rule must predict properties between two theoretical bounds: the Voigt [87] model and the Reuss [88] model, are upper and lower bounds, respectively.

The Voigt model or upper bound, assumes a parallel distribution of the components with respect to the direction of the disturbance (see Figure 8). The effective property (in this case the effective permittivity,  $\bar{\epsilon}$ ) is calculated as the average of the property of each component ( $\epsilon_i$ ), weighted with respect to their volume fraction ( $v_i$ ):

$$\bar{\epsilon} = \sum v_i \epsilon_i \quad 2-31$$

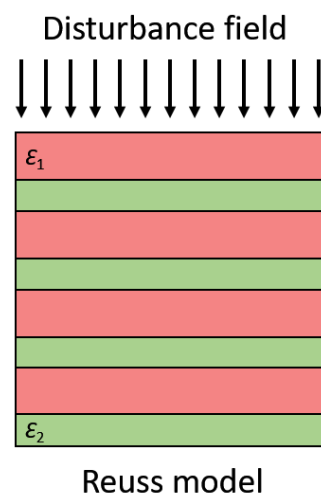




**Figure 8. Schematic representation of a two-component composite, layered parallel to the disturbance field, as established in the Voigt model.**

The Reuss model or lower bound, assumes a perpendicular distribution of the components with respect to the direction of the disturbance (see Figure 9). The inversed effective property is calculated as the average of the inversed property of each component, weighted with respect to their volume fraction:

$$\frac{1}{\bar{\varepsilon}} = \sum \frac{v_i}{\varepsilon_i} \quad 2-32$$



**Figure 9. Schematic representation of a two-component composite, layered perpendicular to the disturbance field, as established in the Reuss model.**

### 2.2.3 Effective Medium Models

Effective medium models are a type of mixture rule in which a filler is considered to be embedded in an effective medium, i.e., in a phase whose properties are equal to the effective property of the composite. Embedding the filler in an effective medium allows more exact solutions to be derived when the filler concentration is high, in comparison to other models [57].

An exact solution for the effective permittivity of a heterogeneous material is impossible to achieve (see more details in section 2.2.4). Effective medium models and other mixture rules are therefore approximations.

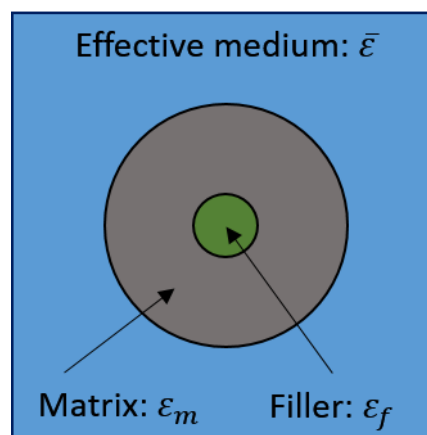


Figure 10. Schematic representation of the effective medium approach.

#### 2.2.3.1 Polder/van Santen/Böttcher (PvSB) model

An effective medium model for dielectric properties of a composite with ellipsoidal inclusions will be considered in this thesis. The equations were first derived by Böttcher [59] (based on the Bruggeman approximation [58]) for spherical fillers, then by Polder and van Santen for randomly oriented ellipsoids [60] and alternatively by Hsu [61] for the complex susceptibility. From this point, we will refer to this model as the Polder/van Santen/Böttcher model or PvSB model. Equations 2-33 and 2-34 represent the PvSB model for oriented and randomly oriented ellipsoids, respectively:

$$\bar{\epsilon} = \epsilon_m + (\epsilon_f - \epsilon_m)v \frac{\bar{\epsilon}}{\bar{\epsilon} + (\epsilon_f - \bar{\epsilon})A_k} \quad 2-33$$

$$\bar{\varepsilon} = \varepsilon_m + (\varepsilon_f - \varepsilon_m) \frac{\nu}{3} \sum_{k=1}^3 \frac{\bar{\varepsilon}}{\bar{\varepsilon} + (\varepsilon_f - \bar{\varepsilon})A_k} \quad 2-34$$

Where  $\bar{\varepsilon}$ ,  $\varepsilon_m$  and  $\varepsilon_f$  are the permittivities of the composite, matrix and filler, respectively;  $\nu$  is the volume concentration of the filler; and  $A_k$  is the depolarization factor of the filler in the  $k$  direction, which is a function of the aspect ratio of the filler. The case of randomly oriented fillers assumes that the fillers are equally aligned with respect to each of the three main directions.

A derivation of these equations is presented in section 2.2.4.

In equations 2-33 and 2-34,  $\varepsilon$  can be substituted by the complex susceptibility,  $\chi^*$  [61]:

$$\bar{\chi}^* = \chi_m^* + (\chi_f^* - \chi_m^*) \nu \frac{\bar{\chi}^*}{\bar{\chi}^* + (\chi_f^* - \bar{\chi}^*)A_k} \quad 2-35$$

$$\bar{\chi}^* = \chi_m^* + (\chi_f^* - \chi_m^*) \frac{\nu}{3} \sum_{k=1}^3 \frac{\bar{\chi}^*}{\bar{\chi}^* + (\chi_f^* - \bar{\chi}^*)A_k} \quad 2-36$$

This formulation is especially convenient when considering conductive fillers in a non-conductive matrix. In that case, matrix and filler can be entirely described by permittivity ( $\chi_m^* = i\omega\varepsilon_m'$ ) and DC conductivity ( $\chi_f^* = \sigma_{DC,f}$ ), respectively [61].

The PvSB model was chosen as the most suitable to describe the composite materials considered in this thesis for several reasons:

- It can model the geometry of typical conductive nanofillers like carbon nanotubes, graphene or carbon black, as explained in section 2.2.4.
- It can predict the dielectric properties of composites with higher concentrations better than other kind of models, like mean field models (Wagner/Sillars model [54], [55], explained in section 2.1.5.3; Fricke model [62], [89], for conductive fillers covered by a non-conductive surface membrane), based on the Maxwell/Garnett approximation [90], which is only applicable for dilute composites.
- It fits well to experimental data: In [57], different methods for calculating the dielectric properties of heterogeneous mixtures (including mean field, effective medium and

integral methods) are discussed and compared to experimental results. The PvSB model fits to experimental data from composites with non-spherical fillers with an error lower than 1 % for volume concentrations below 20 %.

However, there are some known limitations to the applicability of this model. The equations of the PvSB are only exact for composites in which the properties of the components are similar within two orders of magnitudes and when contact resistance and electron tunnelling are negligible [61]. In other words, for composites with conductive fillers in a non-conductive matrix, the PvSB model may deviate from an exact solution (deviations in the prediction of the percolation threshold are known [61], [91]) due to the lack of consideration of the network formation of conductive fillers). Therefore, a modification of the PvSB model is proposed in this thesis to account for the neglected effects of filler networks (see section 4.4).

#### 2.2.4 Derivation of the PvSB Model

The equations of the PvSB model are derived in this section, as reported by Polder and van Santen [60].

We assume that a composite material, with one or more fillers, is placed between a parallel infinite plate capacitor. The components of the composites will be assumed to be isotropic for simplicity. The permittivity of the composite relates the electric field and the electric displacement (see section 2.1.2) as follow:

$$\bar{\mathbf{D}} = \varepsilon \bar{\mathbf{E}} \quad 2-37$$

Where  $\bar{\mathbf{E}}$  and  $\bar{\mathbf{D}}$  are the effective electric field and electric displacement, which are the average electric field and electric displacement for an arbitrary volume in the middle of the capacitor, whose size is much larger than an individual particle of filler, but much smaller than the distance between the plates of the capacitor.

By multiplying equation 2-37 by the volume ( $V$ ) of the material and decomposing to into filler ( $f$ ) and matrix ( $m$ ) we obtain:

$$V\bar{\mathbf{D}} = \int_{V_m} \varepsilon_m \mathbf{E} dv + \sum_f \int_{V_f} \varepsilon_f \mathbf{E} dv = V\varepsilon_m \bar{\mathbf{E}} + \sum_f \int_{V_f} (\varepsilon_f - \varepsilon_m) \mathbf{E} dv \quad 2-38$$

Equation 2-38 can be rewritten as:

$$\bar{\mathbf{D}} = \varepsilon_m \bar{\mathbf{E}} + \sum_f v_f (\varepsilon_f - \varepsilon_m) \frac{1}{V_f} \int_{V_f} \mathbf{E} dv \quad 2-39$$

In which  $v_f$  is the volume concentration of the filler  $f$  with permittivity  $\varepsilon_f$ . It can be seen in equation 2-39 that a mean value of the electric field in the interior of the fillers must be found.

There is no exact solution for this equation [60]. An assumption will be made to obtain an approximate solution: the particle is surrounded by an effective medium whose permittivity is equal to the effective permittivity of the composite, in which the effective electric field  $\bar{\mathbf{E}}$  is homogenous at large distances from the particle.

The mean field inside the particle  $\bar{\mathbf{E}}_i$  can be now set to be proportional to  $\bar{\mathbf{E}}$ :

$$\mathbf{E}_i^{(k)} = \sum_l \alpha_{kq}^{(f)}(\bar{\varepsilon}) \bar{\mathbf{E}}^{(l)}, \quad (k, l = 1, 2, 3) \quad 2-40$$

Where  $\alpha$  is a tensor depending on the effective permittivity ( $\bar{\varepsilon}$ ), the permittivity of the fillers, the geometry of the fillers and the orientation of the fillers.

Assuming that all fillers have the same shape and are randomly oriented, the mean field inside the particle can be approximated by:

$$\frac{1}{V_f} \int_{V_f} \mathbf{E} dv = \frac{1}{3} (\alpha_{11}^{(f)} + \alpha_{22}^{(f)} + \alpha_{33}^{(f)}) \bar{\mathbf{E}} = \alpha^{(f)}(\bar{\varepsilon}) \bar{\mathbf{E}} \quad 2-41$$

Due to the random orientation, only the diagonal components of  $\alpha$  are non-zero. Introducing 2-41 into 2-39 and making use of 2-37, we obtain:

$$\varepsilon' = \varepsilon_f + \sum v_f (\varepsilon_f - \varepsilon_m) \alpha^{(f)}(\bar{\varepsilon}) \quad 2-42$$

It must be noted that 2-42 cannot be, in general, algebraically solved for  $\bar{\varepsilon}$  (although in some cases it reduces to a second or third order polynomial).

An expression for  $\alpha^{(f)}$  can be derived for ellipsoidal<sup>3</sup> particles. For an electric field in the direction  $k$  the ellipsoid will be polarized homogenously and 2-40 will give:

$$E_q^{(k)} = \frac{\bar{E}^{(k)}}{1 + \left(\frac{\epsilon_f}{\epsilon'} - 1\right) A_k} \quad 2-43$$

Where  $A_k$  is the depolarization factor in the direction  $k$ .

Using 2-43, equation 2-42 leads to an expression for the effective permittivity of the composite:

$$\bar{\epsilon} = \epsilon_m + (\epsilon_f - \epsilon_m) \frac{v}{3} \sum_{k=1}^3 \frac{\bar{\epsilon}}{\bar{\epsilon} + (\epsilon_f - \bar{\epsilon}) A_k} \quad 2-44$$

$A_k$  can be calculated by the elliptical integral for an ellipsoid with semi-axis  $a$ ,  $b$  and  $c$ , in the directions  $k = 1, k = 2, k = 3$ , respectively [60]. For  $k = 1$ :

$$A_1 = \frac{abc}{2} \int_0^\infty \frac{du}{(a^2 + u)\sqrt{(a^2 + u)(b^2 + u)(c^2 + u)}} \quad 2-45$$

For a prolate ellipsoid ( $a > b = c$ ), the depolarization factor is:

$$A_1 = [-AR/(AR^2 - 1)^{3/2}][e_p - \tanh^{-1}(e_p)] \quad 2-46$$

Where  $\tanh^{-1}$  is the inverse hyperbolic tangent and  $e_p$  is the eccentricity of a prolate ellipsoid:

$$e_p = [1 - (1/AR)^2]^{1/2} \quad 2-47$$

Being  $AR = a/b$  the aspect ratio of the ellipsoid, here defined as greater than one for prolate and lower than one for oblate ellipsoids.

---

<sup>3</sup> An ellipsoid can be seen as a deformed sphere with three different axes ( $a, b, c$ ) in three orthogonal directions  $(x, y, z)$ :  $\frac{x^2}{a^2} + \frac{y^2}{b^2} + \frac{z^2}{c^2} = 1$ . When two of those axes are equal, the ellipsoid is called ellipsoid of revolution or spheroid. The unequal axis can be longer ( $a > b = c$ ) or shorter ( $a < b = c$ ) than the others, in which case we get prolate and oblate ellipsoids, respectively (see Table 4 in page 25).

For an oblate ellipsoid ( $a < b = c$ ), the depolarization factor is:

$$A_1 = [AR/(1 - AR^2)^{3/2}][e_o - \tan^{-1}(e_o)] \quad 2-48$$

Where  $e_o$  is the eccentricity of an oblate ellipsoid:

$$e_o = [(1/AR)^2 - 1]^{1/2} \quad 2-49$$

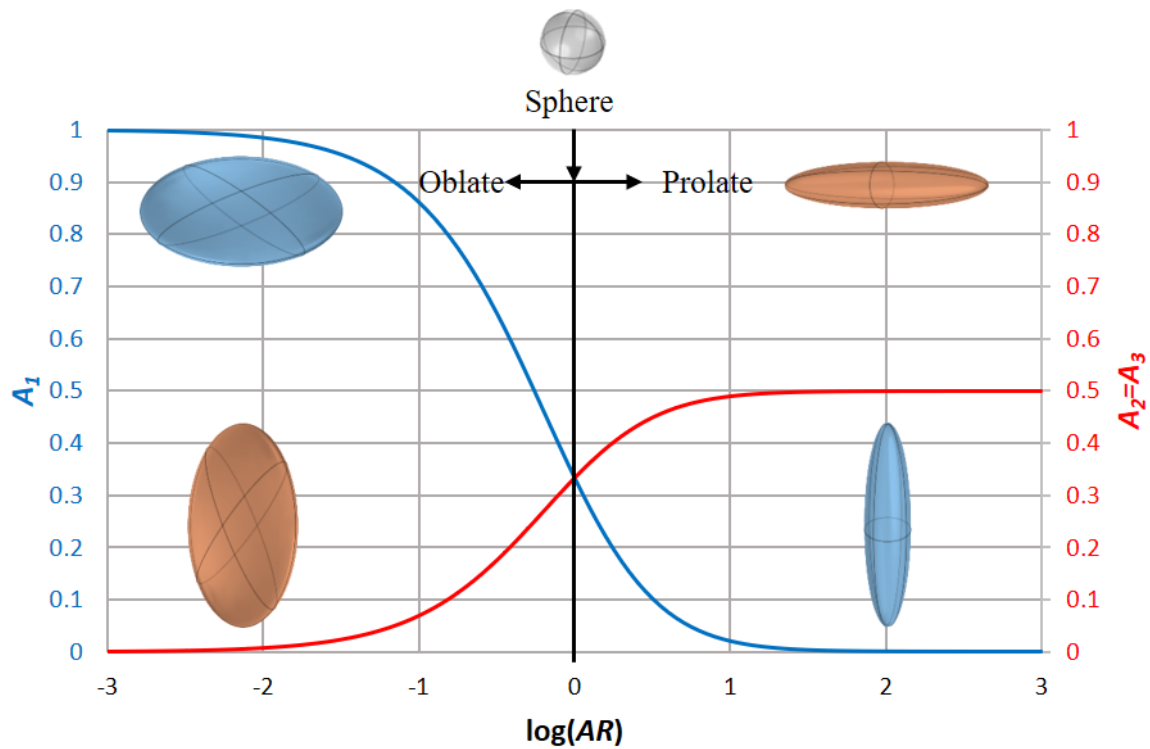
For any ellipsoid, it applies:

$$A_1 + A_2 + A_3 = 1 \quad 2-50$$

The depolarization factors of some special geometries are listed in Table 3, while their dependence on the aspect ratio of the particle is shown in Figure 11.

**Table 3. Depolarization factors for specific geometries.**

<b>Shape</b>	<b>Similar filler</b>	<b>Aspect ratio</b>	<b>Depolarization factors (<math>A_1, A_2, A_3</math>)</b>
<b>Needle-like</b>	Carbon nanotube	$\gg 1$	$(0, \frac{1}{2}, \frac{1}{2})$
<b>Sphere</b>	Carbon black	1	$(\frac{1}{3}, \frac{1}{3}, \frac{1}{3})$
<b>Disc-shaped</b>	Graphene	$\ll 1$	(1,0,0)





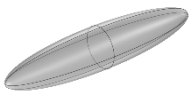

**Figure 11. Parallel ( $A_1$ ) and perpendicular ( $A_2 = A_3$ ) depolarization factors of spheroids as a function of the aspect ratio ( $AR$ ). The convention for orientation described in section 2.2.5 is applied.**

### 2.2.5 Convention for Orientation

The alignment of an ellipsoid of revolution or spheroid with respect to the electric field is referred to its unequal axis. Following this convention, spheroids will be said to be aligned parallel or perpendicular to the electric field as described in Table 4. The convention, which is appropriate for the consistency of the equations, might be counterintuitive for the case of oblate fillers.



**Table 4. Convention for parallel and perpendicular orientation for ellipsoids of revolution, with respect to an electric field in the vertical direction.**

	Prolate	Oblate
Parallel		
Perpendicular		



## 3. Experimental

### 3.1 Materials

The materials used in this thesis are described hereunder. The mentioned property values were provided by the fabricants.

#### 3.1.1 Multi-Walled Carbon Nanotubes

Multi-walled carbon nanotubes (MWNT) were provided by Nanocyl: NC7000™. They are produced by catalytic chemical vapour deposition. According to the technical specifications of Nanocyl [92], NC7000™ have an average diameter of 9.5 nm and an average length of 1.5 μm, as measured through transmission electron microscopy (TEM). The carbon purity is 90 % as measured through thermogravimetric analysis (TGA). The powder volume resistivity of NC7000™ is 1 mΩ·m.

#### 3.1.2 Single-Walled Carbon Nanotubes

Single-walled carbon nanotubes (SWNT) were provided by OCSiAl: Tuball™. According to the technical specifications [93] of OCSiAl, Tuball™ have an outer diameter of 1.6±0.4 nm and an average length of 5 μm as measured through TEM and atomic force microscopy (AFM), respectively. They consist of a mixture of metallic and semiconductive SWNT, whose proportions are not specified. The carbon purity as measured through TGA is 85 %.

#### 3.1.3 Carbon Black

Carbon black (CB) was provided by Unipetrol: Chezacarb AC60. According to the technical specifications of Unipetrol [94], Chezacarb AC60 have an powder electrical resistivity equal or lower than 0.8 Ω·m. Their carbon purity is around 97 %.

#### 3.1.4 Polylactide

Polylactide, also known as polylactic acid (PLA), was provided by Corbion (Total): Luminy 130 (L130). With respect to chirality, L130 is a poly-L-lactide (PLLA). According to the technical specifications [95], the glass transition and melting temperatures of L130 are 57 °C and 175 °C, respectively. Its melting flow index (MFI) is 25 (flow, 210 °C/2.16 kg).

### 3.1.5 Epoxy

The epoxy was provided by Hexion: EPIKOTE RIMR426 (resin) and RIMH433 (curing agent) [96]. The resin/curing agent mixture has low viscosity values, 100-900 mPa·s between 15 °C and 50 °C. The low viscosity facilitates the reorientation of fillers in it, as described in section 3.2.4.

### 3.1.6 Wax

The wax used was Rubitherm's RT42 [97]. Due to its low melting point, 42 °C, it was convenient to fabricate the reference samples of section 4.2. After partial melting and solidification, a good contact with electrodes can be achieved, which is crucial for the reproducibility of dielectric measurements.

## 3.2 Production

### 3.2.1 Compounding of Composites from PLA with MWNT or CB

Composites of MWNT or CB in PLA were compounded in a Leistritz Micro 27 mm 40 L/D twin-screw extruder by Kevin Moser at Fraunhofer ICT within the Bio4Self project. A masterbatch of PLA + 1 wt% MWNT and PLA + 1 wt% composites were kindly provided to be used in this thesis.



Figure 12. Leistritz Micro 27 mm 40 L/D Extruder.

Alternatively, composites with same materials and concentrations were compounded using a Thermo Haake™ MiniLab with conical counter-rotating screws. The compounding took place in a continuous mode at 190 °C with a screw speed of 50 rpm.



**Figure 13. Thermo Haake™ MiniLab with conical counter-rotating screws.**

The compounding with the Haake™ extruder was intentionally performed with a screw configuration that provide a suboptimal mixing of matrix and filler. The composites produced in this way were labelled as “bad dispersion” composites, in contrast to the ones produced with the Leistritz extruder, which operated with optimal processing parameters to produce composites with “good dispersion”.

Masterbatches with both good and bad dispersions were diluted in the Haake™ extruder to produce PLA/CB composites with filler concentrations between 0.05 wt% and 0.5 wt% and PLA/CNT composites with filler concentrations between 0.01 wt% and 0.5 wt%. Because PLA/CNT composites have a lower percolation threshold, they were diluted to lower concentrations so that more low-conductive samples were available for the dielectric measurements.

The dilution with the Haake™ extruder did not alter the difference in dispersion between the good and bad dispersion composites (see micrographs in section 5.2).

### **3.2.2 Sample Preparation of PLA Composites**

Round disk-shaped samples with 40 mm in diameter and 0.5 mm thick were fabricated by compression moulding in order to perform the dielectric characterization. A Collin P 200 P/M press was used. Pellets of the composites were placed in metallic moulds between plates and covered by Kapton® films to avoid adherence to the plates. The compression took place at

190 °C under 2 bar for 3 minutes, followed by 10 bar for 2 minutes and 80 bar for 3 minutes. The samples were then removed from the press and rapidly cooled down in water at room temperature to produce amorphous phase in the polymer.

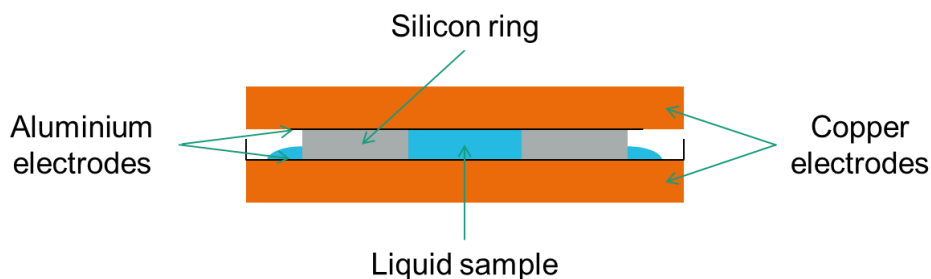
Films with a thickness of 90  $\mu\text{m}$  were produced in a similar way (substituting the metallic moulds with Kapton<sup>®</sup> moulds) to characterize them with transmission optical microscopy.

### 3.2.3 Three-Roll Milling of Epoxy/SWNT Suspensions

Epoxy/SWNT suspensions were obtained by three-roll milling by Marco Marcellan at Fraunhofer ICT and were kindly provided by Manuel Morais (Fraunhofer ICT). The suspensions were made in a regressive program at a fixed roll speed of 180 rpm. A total of 8 passes were performed with decreasing roll gaps: 2 passes with gaps of 60  $\mu\text{m}$  and 20  $\mu\text{m}$ , 2 passes with gaps of 30  $\mu\text{m}$  and 10  $\mu\text{m}$  and finally 4 passes with gaps of 15  $\mu\text{m}$  and 5  $\mu\text{m}$ . Resins were produced at different SWNT concentrations: 0.0005 wt%, 0.001 wt%, 0.005 wt% and 0.01 wt%.

### 3.2.4 Sample Preparation of Epoxy Composites

The epoxy/SWNT suspensions were cured for 50 minutes at 100 °C in the cell shown in Figure 14. This cell was designed to allow dielectric measurement during the curing process of the epoxy. The suspension was poured into silicon ring mould with an internal diameter of 20 mm and a thickness of 2 mm, within an aluminium recipient. An aluminium cover enclosed the suspension in the ring, so that electrical contact is made at the top and bottom surfaces. Excess suspension can flow out and can be later removed.



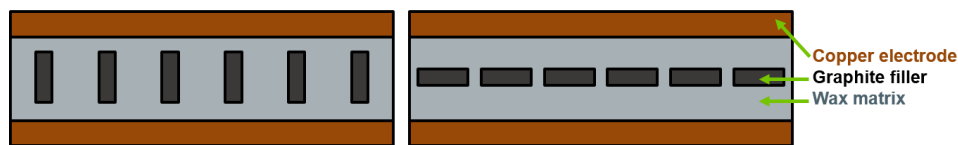
**Figure 14. Profile view of the cell where the epoxy/SWNT suspensions were simultaneously cured and characterized.**

The cell was installed in a sample holder for dielectric measurements (see section 3.3.1.1) and placed in an oven with a controlled temperature of 100 °C.

This setup allows the monitorization of the dielectric properties of the sample during the curing process. Moreover, some samples were subjected to a relatively strong AC electric field ( $100 V_{\text{rms}}$ , for a thickness of 2 mm) at a frequency of 1 MHz to influence the position of the SWNT in the resin (as explained in section 2.1.6).

### 3.2.5 Reference Samples with Controlled Morphology

Reference samples were fabricated with controlled shape and orientation of fillers (see Figure 15). Wax (Rubitherm RT42) was chosen as matrix due to its mouldability. After partial melting and solidification, a good contact with the electrodes was achieved, which is crucial for the reproducibility of the dielectric measurements. Silver and graphite filaments were chosen as conductive fillers. Graphite was chosen as a macroscopic “equivalent” of CNTs. Silver was easier to handle during the fabrication process and served to test the effect of different conductive materials.



**Figure 15.** Schematic representation of the reference samples for the cases of parallel (left) and perpendicular (right) alignment with respect to the electric field.

The dielectric properties of the samples were measured in a parallel-plate capacitor configuration. The samples were disk-shaped with 20 mm diameter and 2 mm thickness. Due to fabrication limitations, the thickness could not be lower. Although these dimensions are not optimal for the determination of the dielectric constant (border effects are high, as explained in section 3.3.1.2.1), the apparent dielectric constant can be used to compare the samples with the model.

Graphite and silver fillers in form of short fibres (1.7 mm length, 0.6 mm diameter) were manually included in the matrix vertically and horizontally, with nominal volume concentrations of 2 % and 4 %. They were placed in the middle of the samples to avoid direct contact with the electrodes.

### 3.3 Characterization

#### 3.3.1 Volume versus Mass Concentrations

Mass concentrations are typically more convenient than volume concentrations for composites, as the mass of matrix and fillers can be easily measured and do not change after the compounding. However, volume concentrations are more relevant when considering effective medium models. Therefore, the volume concentration was calculated for all the composites considered in this thesis.

The density of the filler must be obtained for this purpose. The density of CNTs was calculated as follow [98], [99]:

The average volume of CNTs ( $V_{CNT}$ ), considering them as cylinders with hemispheres at both bases [100], [101], is:

$$V_{CNT} = \frac{\pi}{6} D_{CNT}^3 + D_{CNT}^2 L_{CNT} \quad 3-1$$

With  $D_{CNT}$  and  $L_{CNT}$  the average diameter and length of CNTs.

The average mass of CNTs  $m_{CNT}$ :

$$m_{CNT} = S_{tot} \sigma_C \quad 3-2$$

Where  $S_{tot}$  is the total surface of layers and  $\sigma_C$  the surface density of carbon:

$$S_{tot} = \pi L_{CNT} N (D_{CNT} - N\delta) \quad 3-3$$

$$\sigma_C = \frac{4m_a}{3\sqrt{3}a_{C-C}^2} \quad 3-4$$

Where  $N$  is number of layers in CNTs,  $\delta=0.335$  nm is the distance between layers,  $m_a$  is the atomic mass of carbon and  $a_{C-C} = 0.142$  nm is the distance between carbon atoms.

Finally, the average density of CNTs is:



$$\rho_{CNT} = \frac{m_{CNT}}{V_{CNT}} \quad 3-5$$

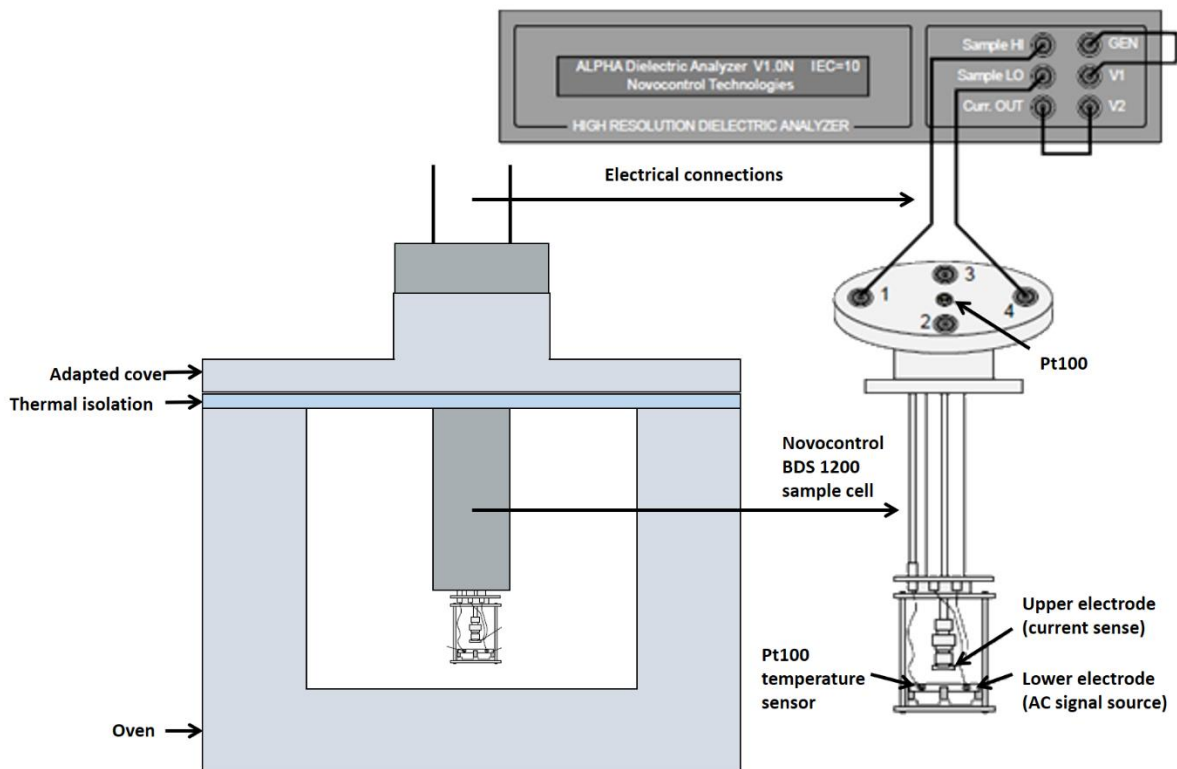
The volume concentration ( $v$ ) can be obtained as a function of the mass concentration ( $w$ ):

$$v = \frac{1}{1 + \frac{1-w}{w} \frac{\rho_{filler}}{\rho_{polymer}}} \quad 3-6$$

Where  $\rho_{filler}$  and  $\rho_{polymer}$  are the densities of the filler and the polymer, respectively.

### 3.3.1.1 Dielectric Measurements

A setup was developed to measure dielectric properties at controlled temperatures from -100 °C to 400 °C. The components of the setup are depicted in Figure 16.



**Figure 16.** Experimental setup for the measurement of dielectric properties at controlled temperatures.

The sample holder is a Novocontrol BDS1200. The sample cell has a parallel-plate capacitor configuration. A metallic shielding covering the sample cell avoids electrical noise. The sample cell is designed for temperatures between -200 °C and 400 °C and includes a Pt100 element, to measure the temperature below the lower electrode.

The impedance analyser is a Novocontrol Alpha Analyser (kindly provided by Dr.-Ing. Wolfgang Menesklou, Institut für Angewandte Materialien - Werkstoffe der Elektrotechnik (IAM-WET), Karlsruhe Institut für Technologie (KIT)), providing high precision measurements of high resistive sample ( $|Z| \pm 0.01 \%$ , phase angle  $\pm 0.002^\circ$ ).

An oven was adapted to fit the BDS1200 sample holder, where temperatures up to 400 °C can be reached.

Disk-shaped samples were measured in a parallel-plate configuration. Samples were sputtered with gold on opposite surfaces to improve the contact with the electrodes of the sample holder. In this way, electrode polarization (described in section 2.1.5.4) is avoided and measurements are reproducible.

### 3.3.1.2 Optimal Sample Dimensions for Dielectric Measurements

Choosing the appropriate sample dimensions is critical for the determination of permittivity. Two opposing effects are playing a role:

- Border effects are only negligible for thin samples.
- Too high conductivities, outside of the instrumental range for permittivity determination, are obtained for thin samples.

#### 3.3.1.2.1 Border Effects on Dielectric Measurements

The determination of the permittivity of a material in a parallel-plate capacitor configuration is provided by:

$$C = \varepsilon \varepsilon_0 \frac{A}{d} \quad 3-7$$

However, equation 3-7 assumes that the material is placed between infinite parallel electrodes. In practice, the finite area of the electrode give rise to border effects (Figure 17). The electric field is therefore non-uniform close to the borders, affecting the observed permittivity calculated with the previous equation.

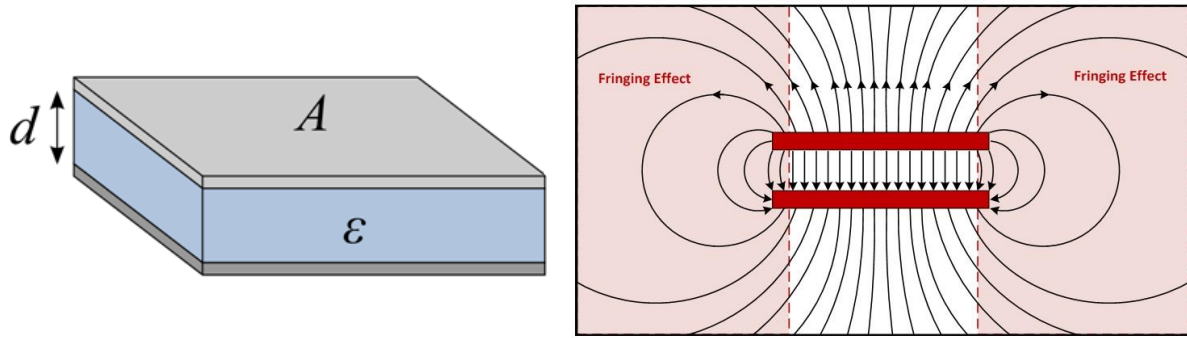


Figure 17. Representation of an infinite parallel-plate capacitor (left) and border or fringing effects on a real finite capacitor (right).

The border effects were theoretically analysed by Kirchhoff [102] for parallel cylindrical electrodes:

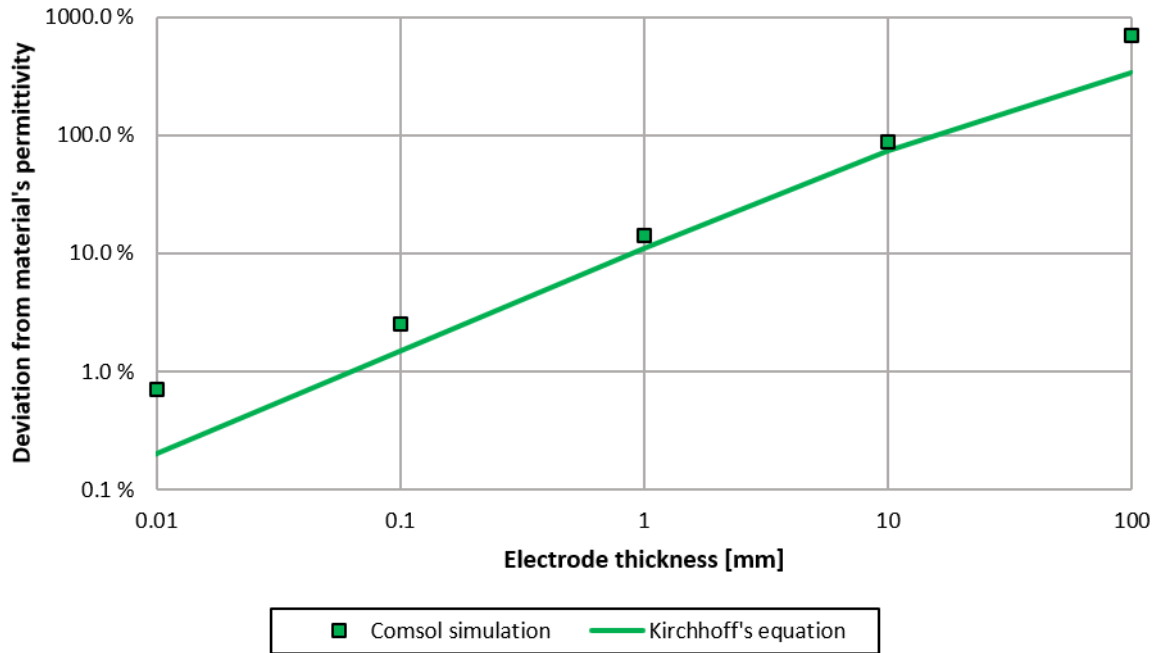
$$\frac{C_{edge}}{C_0} = \frac{2d_e}{\pi D_e} \left[ \ln \left( \frac{8\pi D_e}{d_e} \right) - 3 + z(x) \right] \quad 3-8$$

$$z(x) = (1 + x) \ln(1 + x) - x \ln(x), x = \frac{t_e}{d_e} \quad 3-9$$

$$C_0 = \varepsilon_0 \frac{\pi}{4} \frac{D_e^2}{d_e} \quad 3-10$$

Where  $D_e$  is the electrode diameter;  $d_e$  is the distance between the electrodes;  $t_e$  is the thickness of the electrodes; and  $\varepsilon_0$  is the permittivity of empty space.

The influence of the border effects was simulated in Comsol Multiphysics® (more details on simulations in section 4.3) for a 40 mm diameter electrode (dimensions of the electrodes used for the samples in chapter 5) with different thickness. The results of the simulations, as well as the predictions of Kirchhoff's equation, are shown in Figure 18 in terms of the deviation of the apparent permittivity with respect to the real permittivity of the material, i.e., the ratio of the observed permittivity to the actual material's permittivity.



**Figure 18. Relative influence of the border effects for a 40 mm diameter electrode for different thicknesses. Comparison of theoretical values with FEM (finite element method) simulations in Comsol Multiphysics®.**

It can be observed that, for samples with thickness over 1mm, the deviation of the apparent permittivity with respect to the real permittivity of the material is over 10 %. Therefore, thicknesses lower than 1 mm are advisable. These border effects can be quantified and used to correct the measurement results. However, if the border effects are in the same order of magnitude or higher than the material's permittivity (deviation in Figure 18 equal or greater than 100 %), the precision of the measurement will be considerable reduced.

### 3.3.1.2.2 Instrumental Accuracy for Conductive Samples

In the case of conductive samples, the instrumental accuracy of the impedance analyser might be considerable reduced. In Figure 19, the accuracy specification of Novocontrol's Alpha impedance analyser is shown.

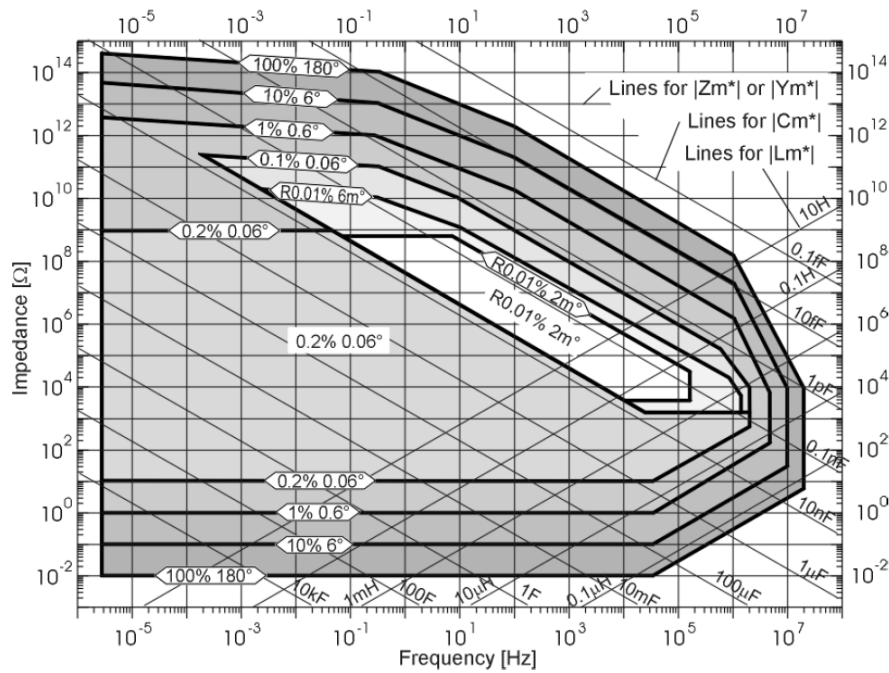


Figure 19. Novocontrol's Alpha impedance analyzer accuracy specification [103].

Samples with impedances lower than  $10 \Omega$  at 1 kHz provide phase errors higher than  $0.6^\circ$ , which provides unacceptable values of capacitance.

For the PLA composites of chapter 5, the optimal thickness was found to be 0.5 mm. The thickness of the epoxy composites of chapter 6 is 2 mm, implying relatively high errors in the determination of the absolute value of permittivity.

### 3.3.2 Scanning Electron Microscopy (SEM)

The PLA composites of chapter 5 were characterised using SEM. Pellets of different composites were fractured at cryogenic conditions, in order to expose internal sections of the composites without incurring in plastic deformation of the sample, which might alter the position of the fillers.

Secondary electrons were collected with the in-lense detector, using an EHT (extra high tension or accelerating tension) of 3 kV. With this configuration, electrons do not penetrate deep into the material, i.e., SEM images show features on the surface or very close to it.

### 3.3.3 Transmission Optical Microscopy (TOM)

TOM images were taken of composite films of  $90 \mu\text{m}$  thickness using a Leica DFC295. All images were taken with the same conditions of illumination, augmentation and exposure time.

The TOM images were analysed using the software ImageJ, in order to quantify the area of observable agglomerates in the composite. Pictures were converted to 8-bit images. The area of agglomerates was discriminated using the so-called Minimum Method [104].

A total of 10 images were taken per material and the average fraction area of agglomerate was calculated.

## 4. Modelling and Simulation of Dielectric Properties

The PvSB model can only be applied to ideal composites, as described in section 2.2.3.1. The PvSB model was experimentally validated using composites fabricated with controlled morphologies (section 4.2). Additionally, the PvSB model was compared with simulations of ideal composites (section 4.3.2).

In section 4.3.3, simulations of composites with different non-ideal features, typical in real composite, are presented. An extended PvSB model is derived from the results of these simulations (section 4.4). However, the extended PvSB model could not be experimentally validated, due to the complexity of producing real composites with controlled morphologies.

A methodology is proposed in section 4.5 to obtain morphological information from experimental data using the extended PvSB model.

### 4.1 PvSB Model for Composites with Conductive Fillers

#### 4.1.1 Reformulation of the PvSB Model

The PvSB model (equations 2-33 and 2-34) can be reformulated into a more convenient form for the purpose of this thesis:

$$\bar{\epsilon} = \epsilon_m + (\epsilon_f - \epsilon_m) \left[ v_{f\parallel} \frac{\bar{\epsilon}}{\bar{\epsilon} + (\epsilon_f - \bar{\epsilon})A_{f\parallel}} + v_{f\perp} \frac{\bar{\epsilon}}{\bar{\epsilon} + (\epsilon_f - \bar{\epsilon})A_{f\perp}} \right] \quad 4-1$$

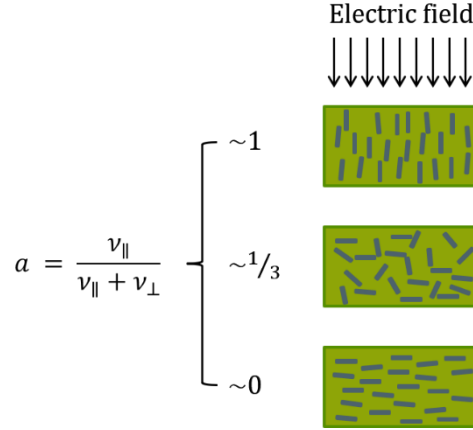
Where the fillers have been divided into parallel ( $\parallel$ ) and perpendicular ( $\perp$ ) to the electric field. It must be noted that every filler whose main axis is within a plane perpendicular to the electric field, has the same depolarization factor, whatever its orientation within that plane.

It is therefore possible to define an alignment parameter ( $a$ ) as follows:

$$a = \frac{v_{\parallel}}{v_{\parallel} + v_{\perp}} = \frac{v_{\parallel}}{v_f} \quad 4-2$$

Which represents the volume fraction of the fillers that are parallel to the electric field. When all the fillers are aligned parallel to the electric field,  $a = 1$ ; when all fillers are perpendicular

to the electric field,  $a = 0$ ; when the fillers are randomly oriented,  $a = 1/3$  (in a random configuration, the average orientation of the fillers contribute to the three orthogonal directions in the same amount).



**Figure 20.** Definition of the alignment parameter,  $a$ , and schematic representation of composites for different values of  $a$ : 1, 1/3 and 0.

Introducing the alignment parameter from 4-2 into 4-1, it remains:

$$\bar{\varepsilon} = \varepsilon_m + (\varepsilon_f - \varepsilon_m)v_f \left[ a \frac{\bar{\varepsilon}}{\bar{\varepsilon} + (\varepsilon_f - \bar{\varepsilon})A_{f\parallel}} + (1 - a) \frac{\bar{\varepsilon}}{\bar{\varepsilon} + (\varepsilon_f - \bar{\varepsilon})A_{f\perp}} \right] \quad 4-3$$

Equation 4-3 can be further extended to include the dispersion of the filler in the composite. Fillers may form agglomerates with a different shape (aspect ratio) and in general different dielectric properties. Agglomerates will be considered as a second kind of filler:

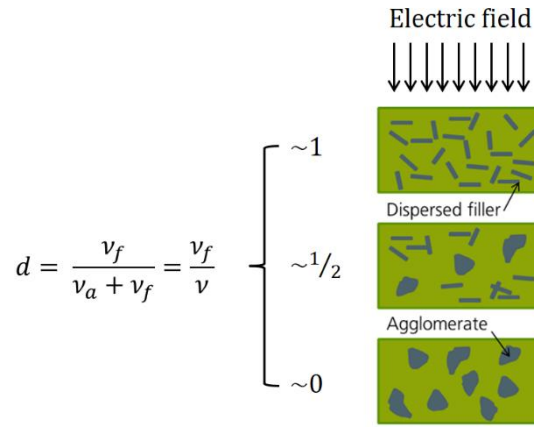
$$\begin{aligned} \bar{\varepsilon} = \varepsilon_m + (\varepsilon_f - \varepsilon_m)v_f \left[ a_f \frac{\bar{\varepsilon}}{\bar{\varepsilon} + (\varepsilon_f - \bar{\varepsilon})A_{f\parallel}} + (1 - a_f) \frac{\bar{\varepsilon}}{\bar{\varepsilon} + (\varepsilon_f - \bar{\varepsilon})A_{f\perp}} \right] \\ + (\varepsilon_a - \varepsilon_m)v_a \left[ a_a \frac{\bar{\varepsilon}}{\bar{\varepsilon} + (\varepsilon_a - \bar{\varepsilon})A_{a\parallel}} + (1 - a_a) \frac{\bar{\varepsilon}}{\bar{\varepsilon} + (\varepsilon_a - \bar{\varepsilon})A_{a\perp}} \right] \end{aligned} \quad 4-4$$

Where  $v_a$ ,  $\varepsilon_a$ ,  $A_{a\parallel}$  and  $A_{a\perp}$  are the volume concentration, the permittivity and the depolarization factors of the agglomerates parallel and perpendicular to the electric field.  $a_f$  and  $a_a$  are the alignment parameters for fillers and agglomerates, respectively.

Dispersion ( $d$ ) is defined as the volume fraction of fillers that are isolated in the matrix:



$$d = \frac{v_f}{v_a + v_f} = \frac{v_f}{v} \quad 4-5$$



**Figure 21.** Definition of the dispersion parameter,  $d$ , and schematic representation of composites for different values of  $d$ : 1, 1/2 and 0.

Introducing the dispersion parameter from 4-5 into 4-4, it remains:

$$\bar{\varepsilon} = \varepsilon_m + (\varepsilon_f - \varepsilon_m)vd \left[ a_f \frac{\bar{\varepsilon}}{\bar{\varepsilon} + (\varepsilon_f - \bar{\varepsilon})A_{f\parallel}} + (1 - a_f) \frac{\bar{\varepsilon}}{\bar{\varepsilon} + (\varepsilon_f - \bar{\varepsilon})A_{f\perp}} \right] \quad 4-6$$

$$+ v(1 - d) \left[ a_a \frac{\bar{\varepsilon}}{\bar{\varepsilon} + (\varepsilon_a - \bar{\varepsilon})A_{a\parallel}} + (1 - a_a) \frac{\bar{\varepsilon}}{\bar{\varepsilon} + (\varepsilon_a - \bar{\varepsilon})A_{a\perp}} \right]$$

The permittivity of the composite ( $\bar{\varepsilon}$ ) cannot be solved algebraically, as a fourth order polynomial is obtained. Numerical methods must therefore be used to solve it.

Equation 4-6 assumes that an agglomerate is a solid mass, with equal dielectric properties to individual fillers but a different aspect ratio. As it will be shown in section 4.4, this assumption does not predict correctly the permittivity of composites with agglomerates and a reformulation of the PvSB model will be provided to account for it.

#### 4.1.2 PvSB Model Simplification

In the special case of conductive fillers in non-conductive matrices at concentrations below the percolation threshold, the PvSB can be simplified, so that the permittivity of the composite can be solved algebraically.

At concentrations below the percolation threshold, we can assume the permittivity of the matrix and the composites to be much smaller than the permittivity of the filler:

$$\varepsilon_f \gg \varepsilon_m, \varepsilon_f \gg \bar{\varepsilon} \quad 4-7$$

Equation 4-3 simplifies thus into:

$$\bar{\varepsilon} = \varepsilon_m + \varepsilon_f v_f \left[ a \frac{\bar{\varepsilon}}{\bar{\varepsilon} + \varepsilon_f A_{f\parallel}} + (1 - a) \frac{\bar{\varepsilon}}{\bar{\varepsilon} + \varepsilon_f A_{f\perp}} \right] \quad 4-8$$

Assuming  $\varepsilon_f A_{fi} \gg \bar{\varepsilon}$ , (which is true unless  $A_{fi}$  gets close to 0, or AR close to infinity)  $\varepsilon_f$  is cancelled out of the equation and the permittivity of the composite can be solved algebraically:

$$\bar{\varepsilon} = \frac{\varepsilon_m}{1 - v_f \left[ \frac{a}{A_{f\parallel}} + \frac{(1 - a)}{A_{f\perp}} \right]} \quad 4-9$$

Analogously, equation 4-6 leads to:

$$\bar{\varepsilon} = \frac{\varepsilon_m}{1 - vd \left[ \frac{a_f}{A_{f\parallel}} + \frac{(1 - a_f)}{A_{f\perp}} \right] + v(1 - d) \left[ \frac{a_a}{A_{a\parallel}} + \frac{(1 - a_a)}{A_{a\perp}} \right]} \quad 4-10$$

## 4.2 Experimental Validation of the PvSB Model

In order to validate the PvSB model, different reference samples were fabricated with controlled shape and orientation of fillers (see Figure 22).

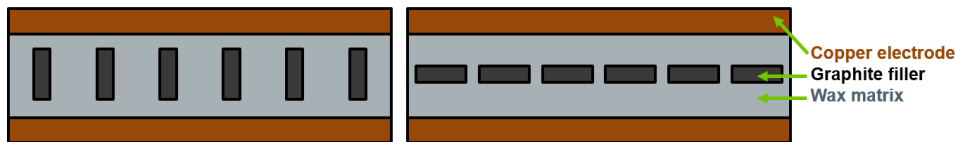
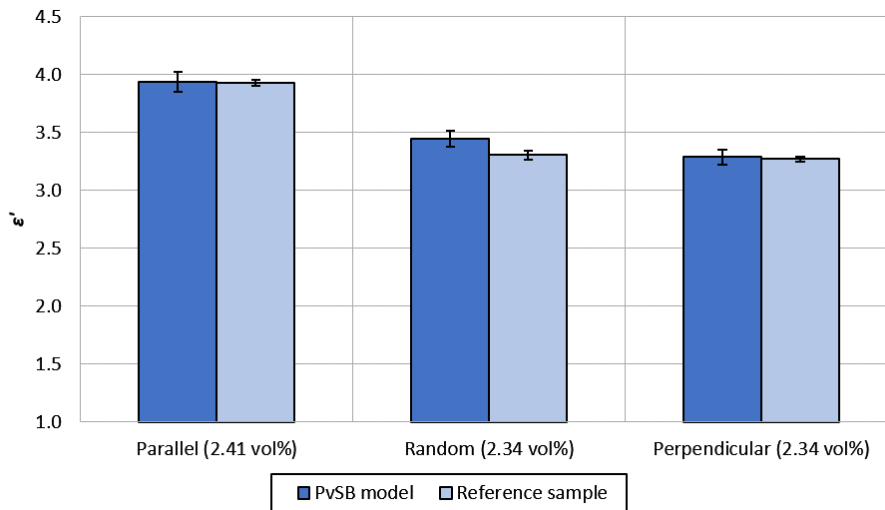


Figure 22. Schematic representation of the reference samples for the cases of: parallel (left) and perpendicular (right) alignment with respect to the electric field.

Details about the fabrication of the reference samples are presented in section 3.2.5.

### 4.2.1 Effect of Orientation

In Figure 23, the calculated and measured real permittivity of wax/silver reference samples is shown. The fillers were aligned vertically (electric field parallel to the fillers' longest axis) and horizontally (electric field perpendicular to the fillers' longest axis) to check the effect of the alignment. As the dielectric spectra of the samples were frequency-independent, the average real part of permittivity between 10 Hz and 1 MHz was considered.



**Figure 23. Modelled and measured permittivity for wax/silver reference samples with different orientations.**

The measurements agree both quantitatively and qualitatively with the PvSB model. It is therefore confirmed the effect of increasing permittivity of needle-like conductive fillers when they are parallel to the electric field.

According to the PvSB model, the random orientation is equivalent to the case in which one third of the fillers are placed vertically, while two thirds are placed horizontally. The reference sample with random orientation was fabricated following this pattern.

The error bars are calculated from the instrumental error of each variable according to a first order propagation of errors. In the case of the simplified PvSB model (equation 4-9), it holds:

$$\Delta\bar{\epsilon} = \frac{\partial\bar{\epsilon}}{\partial\epsilon_m}\Delta\epsilon_m + \frac{\partial\bar{\epsilon}}{\partial v_f}\Delta v_f + \frac{\partial\bar{\epsilon}}{\partial a}\Delta a + \frac{\partial\bar{\epsilon}}{\partial A_{f\parallel}}\Delta A_{f\parallel} + \frac{\partial\bar{\epsilon}}{\partial A_{f\perp}}\Delta A_{f\perp} \quad 4-11$$

Analogously, the error of the measured permittivity is:

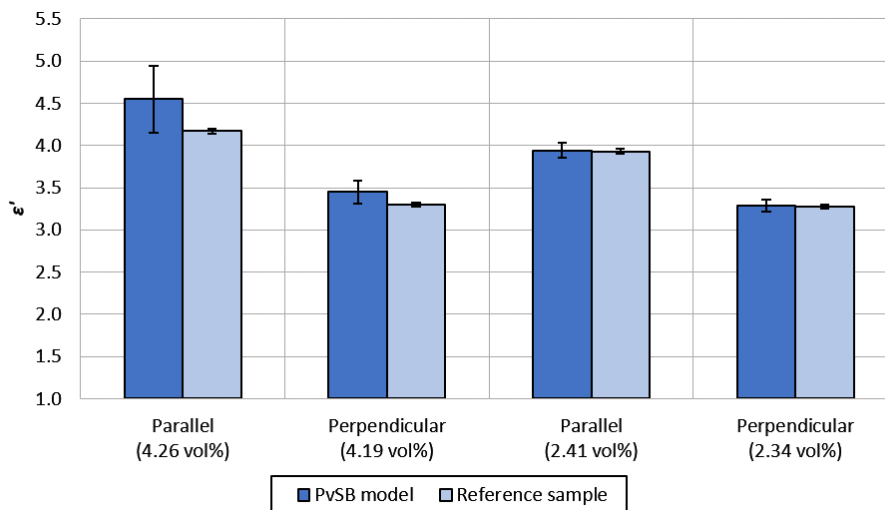
$$\Delta\varepsilon = \frac{\partial\varepsilon}{\partial C}\Delta C + \frac{\partial\varepsilon}{\partial A}\Delta A + \frac{\partial\varepsilon}{\partial d}\Delta d \quad 4-12$$

Given the relation  $C = \varepsilon\varepsilon_0 \frac{A}{d}$ , where  $C$  is the measured capacitance;  $\varepsilon$  and  $\varepsilon_0$  are the relative permittivity of the sample and the permittivity of the empty space, respectively;  $A$  is the area of the electrodes; and  $d$  is the separation between the electrodes.

#### 4.2.2 Effect of Concentration

In Figure 24, the calculated and measured real permittivity of wax/silver reference samples with different filler concentration is shown.

The agreement between model and measurements is again within the limits of the experimental errors. The fabrication process was considerably improved (lower variability of fillers' length) after the samples with 4 % concentration were fabricated. This explains the larger error bars for these samples, especially for the one with vertically aligned fillers, for which the permittivity is more sensible to variations in the aspect ratio of the filler.



**Figure 24. Modelled and measured permittivity for wax/silver reference samples with different filler concentrations.**

#### 4.2.3 Effect of Material

In Figure 25, the calculated and measured real permittivity of wax/silver and wax/graphite reference samples is shown.

No differences are observed between the silver and the graphite fillers. This supports the idea of the effect of the filler being equal for any conductive filler.

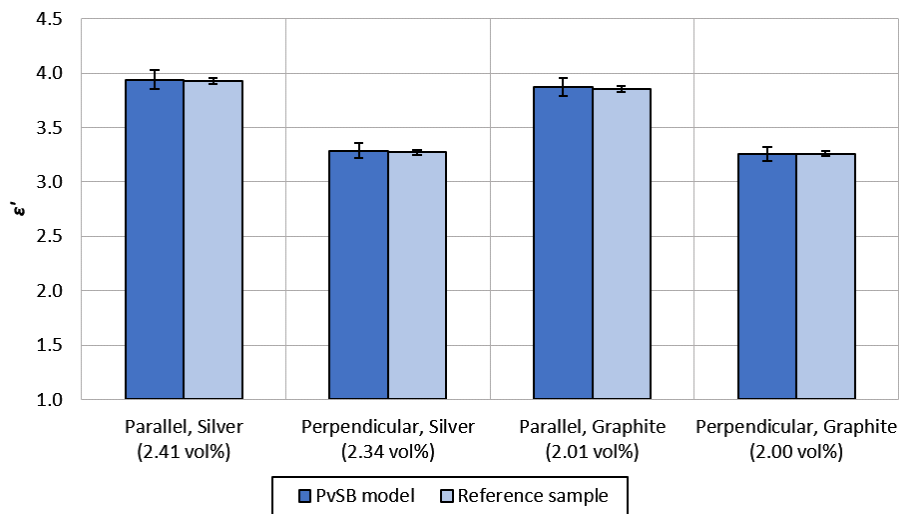


Figure 25. Modelled and measured permittivity for wax/silver and wax/graphite reference samples.

### 4.3 Simulations

The model proposed in this thesis for the dielectric properties of composites was derived following certain assumptions (see section 2.2.4). Some features of real composites (like the inhomogeneous distribution of fillers or the contact between fillers) are not taken into account in the model, giving rise to errors in the predicted permittivity. The permittivity of composites with different configurations was simulated using Comsol Multiphysics<sup>®</sup>, in order to quantify the relative error due to such features.

#### 4.3.1 The Finite Element Method

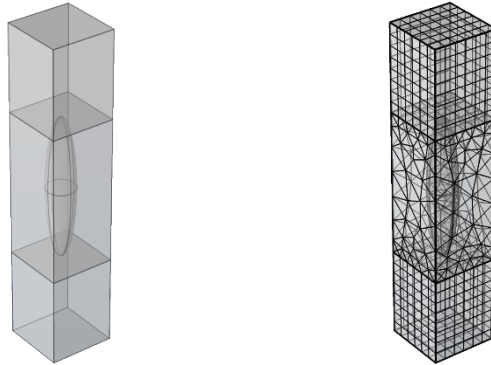
The finite element method was used to perform the simulations. The Maxwell equations were numerically solved for a three-dimensional representation of the composites.

The composite was represented as a right rectangular prism, setting the matrix as a non-conductive polymeric material ( $\epsilon' = 4$ , similar to the epoxy analysed in chapter 6) and a conductive material ( $\sigma = 10^7$  S/m) as ellipsoidal fillers.

A frequency-dependent electric potential difference was set between parallel faces of the prismatic structure. The frequency was set to 1 kHz, well below the characteristic frequency of

the polarization process (see section 2.1.5.3), which was found (through simulations) to be above 10 GHz for all the systems simulated here.

A tetrahedral mesh was set in and around the fillers, in order to better account for the curved geometry of the ellipsoids. Smaller tetrahedra were set in the proximity of edges, so that sharper changes in the electric field could be simulated with more accuracy. A cubic mesh was set away from the filler, where the electric field is mainly homogeneous.



**Figure 26. Simulated geometry: Prismatic composite with an ellipsoidal filler (left) and its corresponding mesh (right).**

Periodical boundary conditions were set at the faces of the prismatic structure, perpendicular to the applied electric field. In this way, the structure was treated as unit cell that repeats itself infinitely in the two directions perpendicular to the applied electric field, so that the ideal case of an infinite parallel plate capacitor can be considered to calculate the permittivity of the system.

### **4.3.2 Simulating Ideal Conditions**

In this section, composite with the ideal configuration assumed by the model are simulated. The case of ellipsoidal fillers with aspect ratios 1 (sphere) and 5 (prolate ellipsoid) are considered. Higher aspect ratios (CNTs can reach aspect ratios greater than 100) are computationally too expensive to simulate. However, an aspect ratio of 5 is enough to reach conclusions on the effect of filler alignment and the congruence of the model with the simulations.

#### **4.3.2.1 Spherical fillers**

The relative permittivity of a composite with spherical fillers was simulated and compared with the prediction of the model (see Figure 27). The different volume concentrations were set by

changing the relative size of the filler with respect to the size of the unit cell. The filler was always centred in the rectangular prism.

At volume concentrations below 7 %, model and simulation agree. At higher concentrations, where the composite approaches percolation and the value of permittivity increases, model and simulation start to disagree.

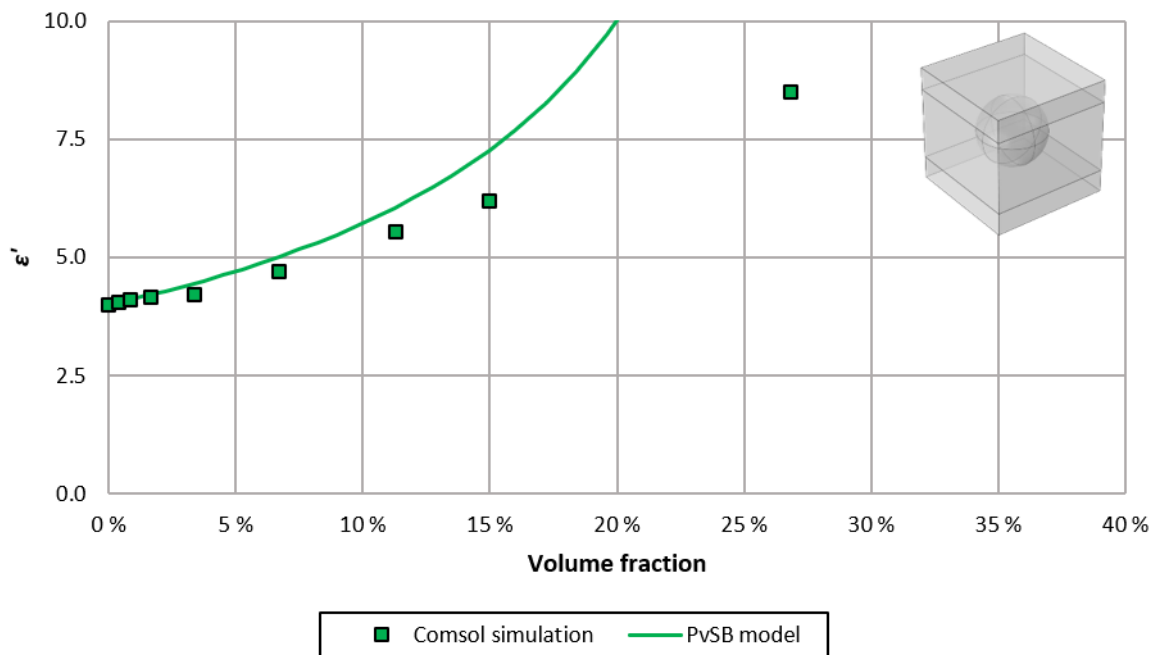


Figure 27. Relative permittivity of composites with different volume concentrations of conductive spherical fillers.

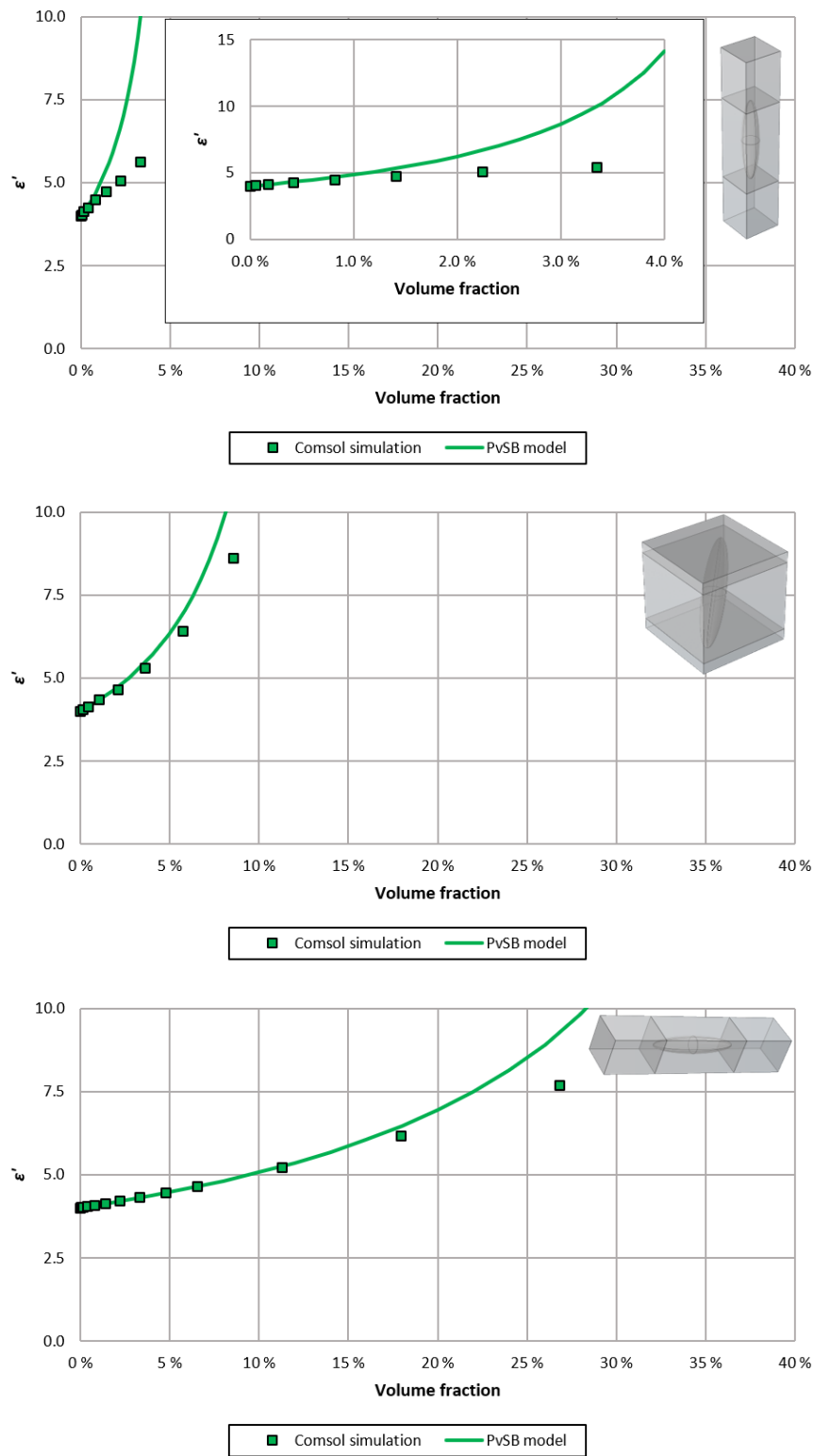
#### 4.3.2.2 Ellipsoidal fillers

To test the effect of filler alignment on the permittivity of the composite, ellipsoidal fillers with an aspect ratio of 5 were simulated. Three different alignments of the fillers were simulated: parallel, perpendicular and at an angle  $\alpha = 63.43^\circ$  with respect to the electric field<sup>4</sup>.

In Figure 28, the simulated permittivity is compared to the one predicted by the model at different concentrations. At low concentrations, model and simulation agree. At concentrations close to the percolation threshold, model and simulation start to disagree. It must be noted that

<sup>4</sup>For a composite with randomly oriented fillers, the fillers have the same probability to be oriented in each of the three orthogonal directions. The alignment parameter is  $a = \frac{1}{3} = \frac{\cos \alpha}{\cos \alpha + \sin \alpha}$ . The angle is therefore  $\alpha = \tan^{-1}(2) \cong 63.43^\circ$ .

the percolation threshold with ellipsoids of aspect ratio 5 happens at lower concentrations than with spheres, as expected.



**Figure 28. Relative permittivity of composites with different volume concentrations of conductive prolate ellipsoidal fillers oriented: parallel (top), randomly (middle) and perpendicular (bottom) with respect to the electric field.**



### 4.3.3 Simulating Non-Ideal Features

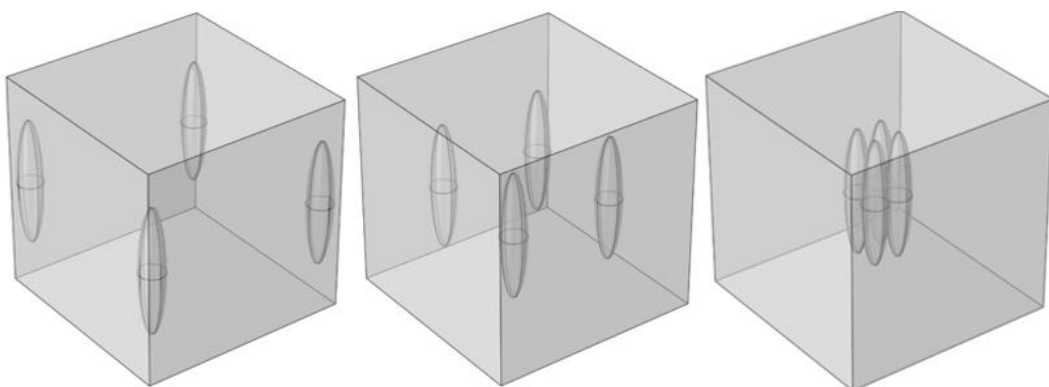
The following features, that might be present in real composites but are not considered in the model, were simulated:

- Gap between fillers
- Distance to electrodes
- Number of layers
- Curvature
- Network of fillers

When appropriate, the features were simulated in composites with equal concentration (1 %), filler aspect ratio (5) and filler alignment (parallel to electric field). The formation of networks, which happens to be the feature with the highest influence, was studied both for ellipsoidal and spherical fillers.

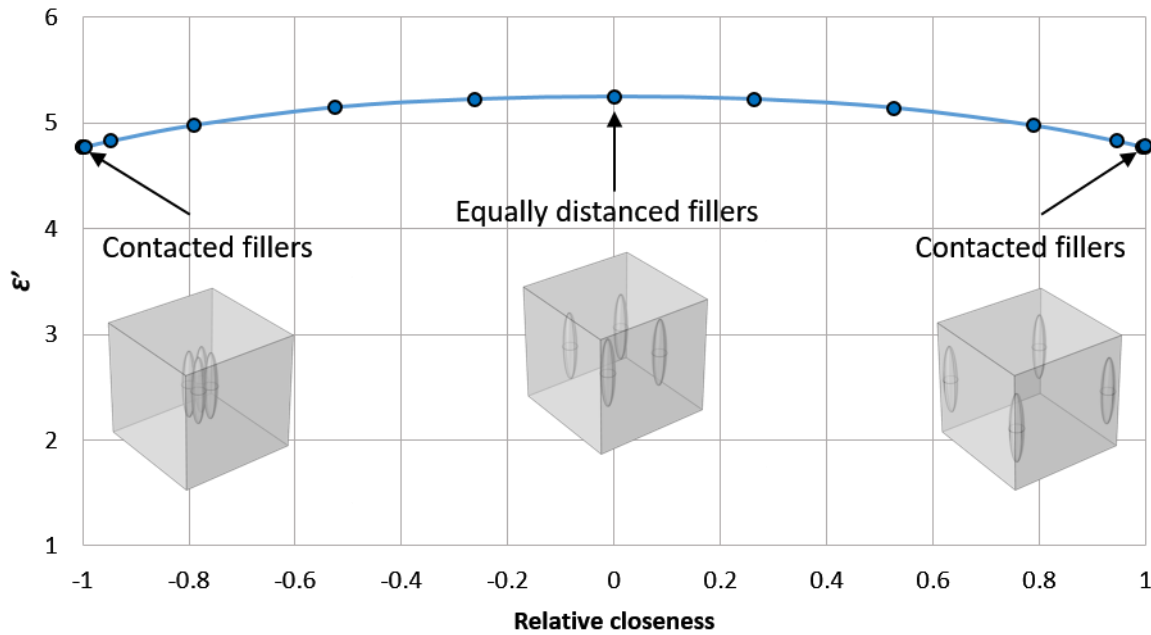
#### 4.3.3.1 Gap between Fillers

An inhomogeneous distribution of particles is not considered in the PvSB model. In this section, the permittivity of composites with different relative distances between fillers is simulated. Four fillers particles are distributed in a unit cell. Two limiting cases, which are equivalent due to the periodical boundary conditions, are considered: all particles are evenly distributed; particles are united in bundles of four units (Figure 29).



**Figure 29. Simulated composites with different filler distances. Cases in left and right are equivalent.**

In Figure 30, the simulated permittivity of the composite is plotted versus the relative closeness among fillers. The relative closeness is defined to be 0 when the fillers are evenly distributed, and  $\pm 1$  when the fillers make contact, varying linearly between both limits.



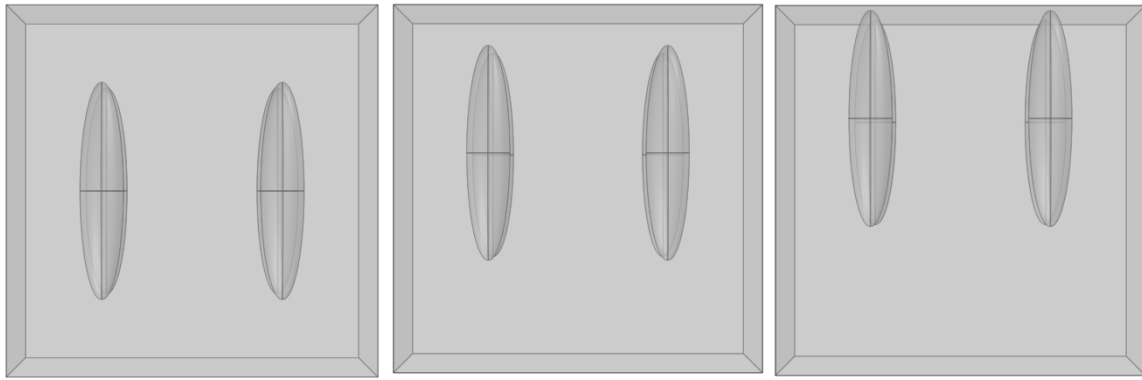
**Figure 30.** Permittivity of the composites described in Figure 29. The fillers are evenly distributed when the relative closeness is 0, and make contact when its value is  $\pm 1$ . The line is a visual guidance.

It is to be noted that, due to the periodic conditions of the simulations, the case in which the particles are united at the centre of the unit cell (relative closeness = -1) is equivalent to the case in which the particles are placed at the edges of the unit cell (relative closeness = +1). The deviation of permittivity with respect to the ideal case (fillers uniformly distributed, considered by the PvSB model and represented by the configuration in the middle in Figure 29, relative closeness = 0) due to the relative distance between fillers is, at most, 9 % for the simulated conditions.

The effect of network formation is analysed in section 4.3.3.5.

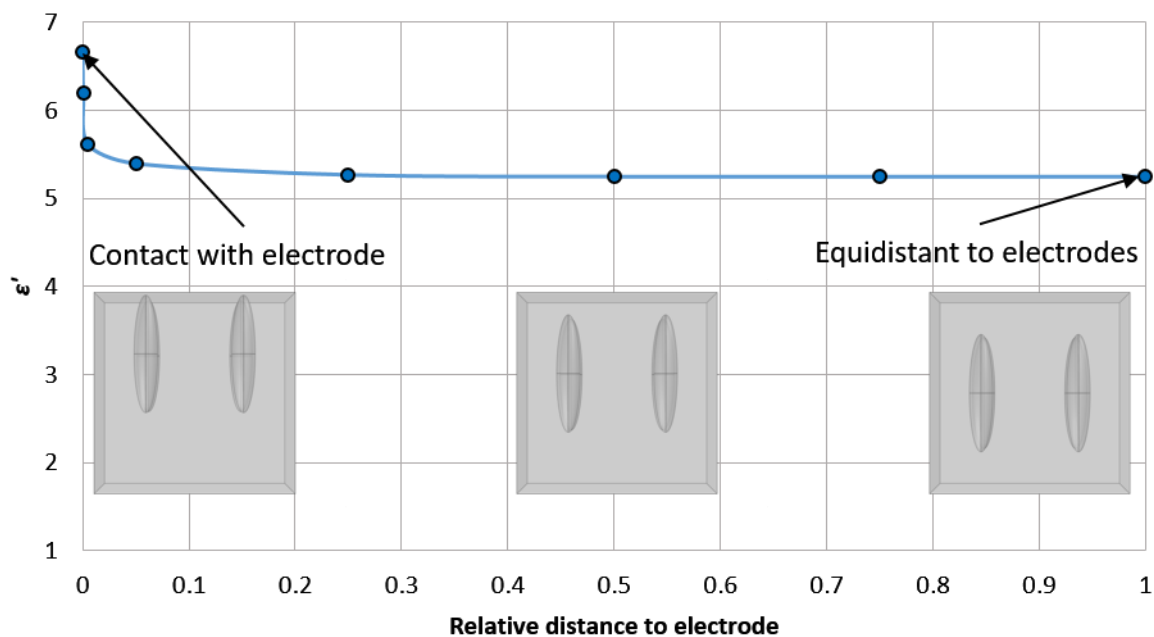
#### 4.3.3.2 Distance to Electrodes

In previous simulations, the fillers were placed in a parallel layer evenly placed between the two electrodes. In this section, the permittivity of the composite is simulated for different distances between four equally distributed filler particles and the electrodes. Two limiting cases are considered: the fillers are placed equidistant to both electrodes; the fillers make contact with one electrode. (Figure 31).



**Figure 31. Simulated composites with different distances between fillers and electrodes.**

In Figure 32, the simulated permittivity of the composite is plotted versus the relative distance to the electrodes. The relative distance is defined to be 0 when the fillers make contact with an electrode and 1 when the fillers are equidistant to both electrodes, varying linearly between both limits.



**Figure 32. Permittivity of the composites showed in Figure 31. The line is a visual guidance.**

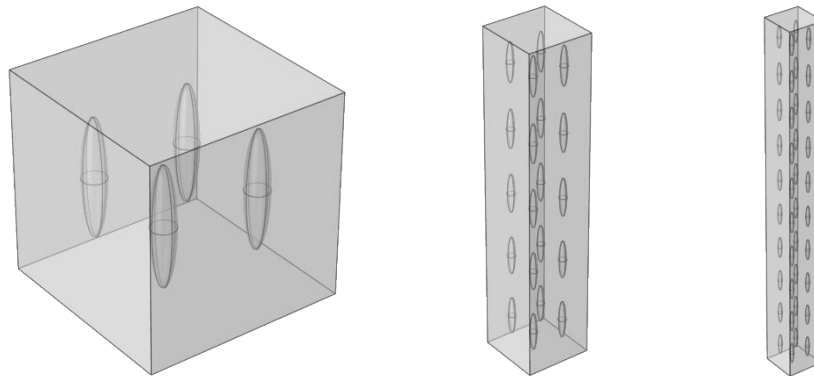
For the simulated conditions, the deviation of permittivity due to the distance to the electrode is negligible when the fillers are away from the electrodes. When the relative distance to the electrodes is 0.5 %, the deviation with respect to the ideal case (fillers equidistant to both electrodes, considered by the PvSB model and represented by the configuration in the left in Figure 31, relative distance to electrode = 1) is 7 %. When the fillers make contact with the

electrode, the deviation is 27 %. That means that this feature is only significant when the filler is very close to the electrode. Moreover, in a macroscopic nanocomposite (in which the thickness of the sample is much larger than the size of the fillers) the number of fillers in contact – or close to contact – with the electrodes is small with respect to the number of fillers in the bulk, thus reducing the overall effect of this feature in a composite.

The conductive fillers behave as internal electrodes. Fillers and electrode behave as a capacitor whose dielectric is the polymer. Only when the distance filler/electrode is small, the capacitance is high enough to be significant. When the conductive filler makes contact with the electrode, both stay at the same voltage, making the filler a prolongation of the original electrode into the composite.

#### 4.3.3.3 Number of Layers

So far, all the fillers were placed in a single layer between the electrodes. In this section, the fillers are located in a varying number of layers. The number of layers is changed from 1, as in previous sections, to 15. (Figure 33). The concentration is the same for every number of layers. Simulating additional layers is computationally more and more expensive and would have a lower and lower effect on the permittivity of the composite.



**Figure 33. Simulated composites with different number of layers of fillers. The filler concentration remains constant.**

In Figure 34, the simulated permittivity of the composite is plotted versus the number of layers. The permittivity increases asymptotically with the number of layers, reaching a maximum value which represent an increase of 8 % with respect to the one-layer composite.

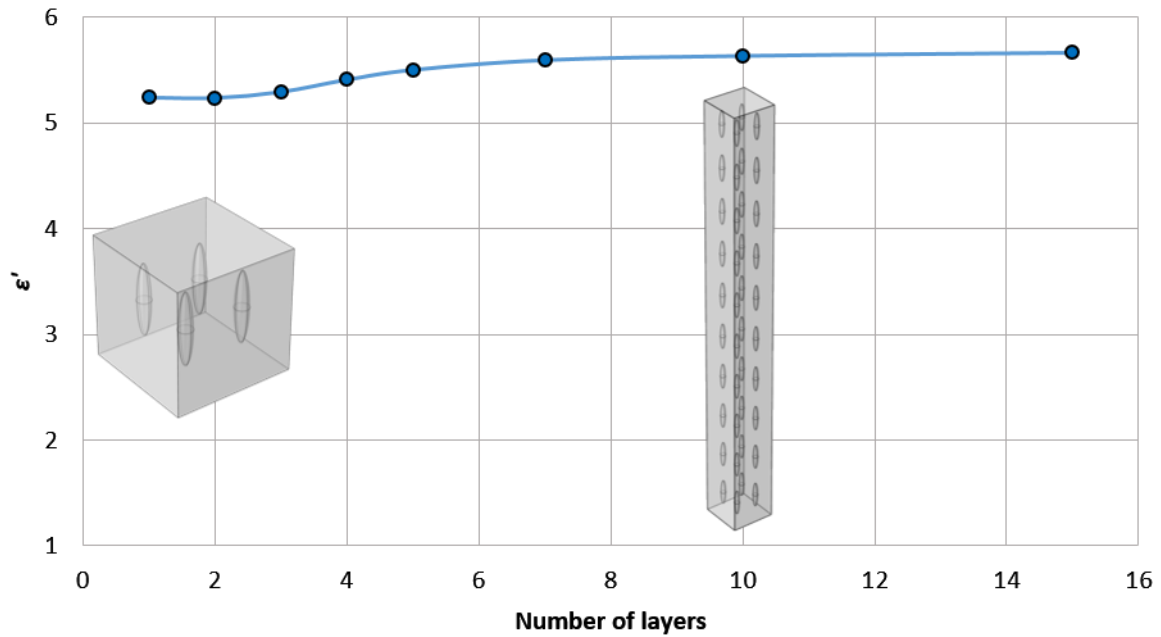


Figure 34. Permittivity of the composites described in Figure 33. The line is a visual guidance.

#### 4.3.3.4 Curvature

Carbon nanotubes are ideally assumed to be straight tubes. However, CNTs do bend in nanocomposites (see the SEM images in section 5.2.1). To account for the effect of CNT curvature, composites with curved tubes (portions of a torus) with different curvature angles ( $\alpha_{max}$ ) were simulated (see Figure 35). The angle of curvature is defined as the ratio of the tube's length to its radius of curvature, in radians. All fillers have the same length and diameter (and hence the same volume). The angle of curvature was set to values between  $0^\circ$  and  $90^\circ$ , being the filler with  $0^\circ$  straight and parallel to the electric field, with an aspect ratio of 5.

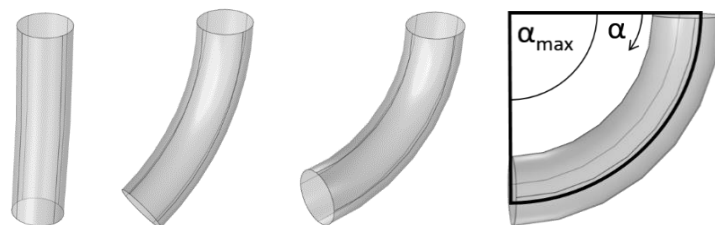


Figure 35. Simulated fillers with different curvature angles ( $\alpha_{max}$ ), for an electric field in the vertical direction.

The curved tubes can be considered in the PvSB model as a linear combination of ellipsoids (with equal aspect ratio and volume as the straight tubes) parallel and perpendicular to the electric field.

In order to calculate the  $v_{\parallel}$  and  $v_{\perp}$  parameters of the PvSB model (see definition in section 4.1.1), the curved filler was decomposed (as done with straight fillers) in two components: parallel and perpendicular to the electric field. as follows.

Given the geometry described in Figure 35, the vertical component of the tangent of an arbitrary point along the tube axis, is:

$$v_{\parallel} = \cos(\alpha) \quad 4-13$$

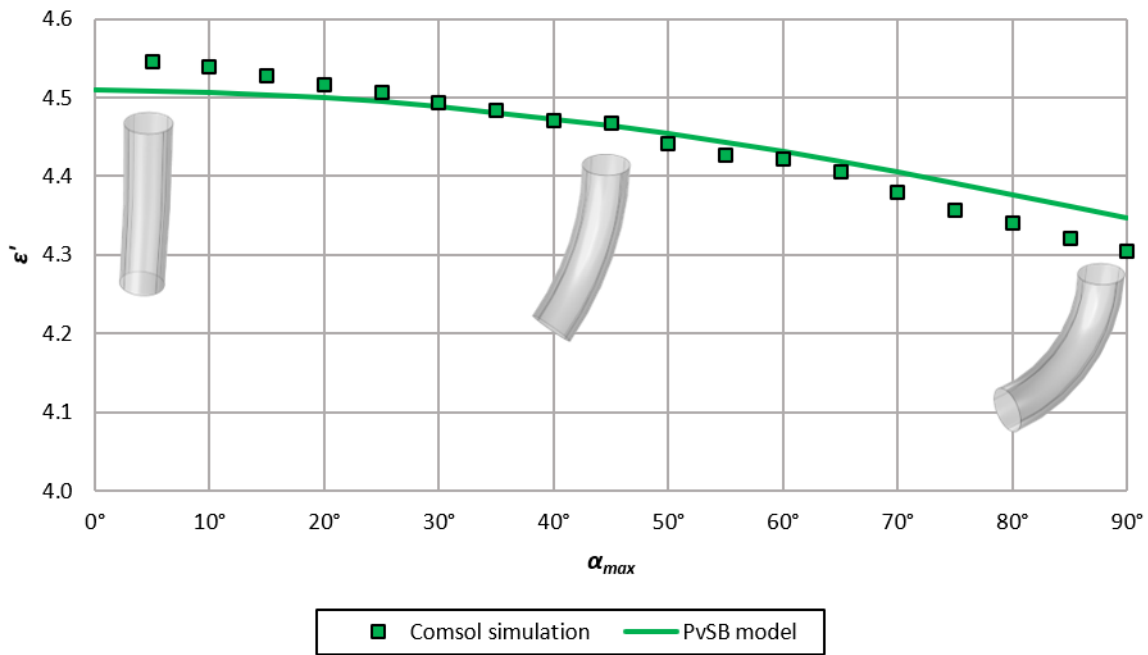
The differential form of equation 4-16 is:

$$dv_{\parallel} = d(\cos(\alpha)) = -\sin(\alpha)d\alpha \quad 4-14$$

And therefore, the average vertical component of the tube ( $\bar{v}_{\parallel}$ ) is:

$$\bar{v}_{\parallel} = \frac{1}{\alpha_{max}} \int_0^{\alpha_{max}} -\sin(\alpha)d\alpha = \frac{1}{\alpha_{max}} [\cos(\alpha_{max}) - 1] \quad 4-15$$

In Figure 36, the permittivity of the composites with curved fillers as obtained from simulations and the PvSB model are shown. Both values agree within a 1 % error. The discrepancies, especially for the straight filler ( $\alpha_{max} = 0$ ) can be explained in terms of the different geometries assumed for the fillers by simulation (cylinder) and model (ellipsoid).



**Figure 36. Simulated and modelled permittivity of the composites with curved fillers described in Figure 35 for different values of the curve angle ( $\alpha_{max}$ ).**

Therefore, we can conclude that the curvature of CNTs is already accounted for in the PvSB model through the  $\nu_{\parallel}$  and  $\nu_{\perp}$  parameters.

#### 4.3.3.5 Network of Fillers

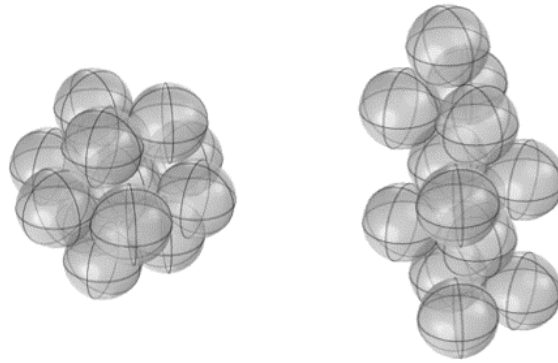
In this section, the effect of the formation of networks of fillers on the effective permittivity of the composite is simulated.

The connection of spherical or ellipsoidal fillers was considered for different kinds of networks:

- Spherical fillers are aggregated in spheroidal or elongated agglomerates.
- Ellipsoidal fillers are connected forming unidirectional chains parallel or perpendicular to the electric field.

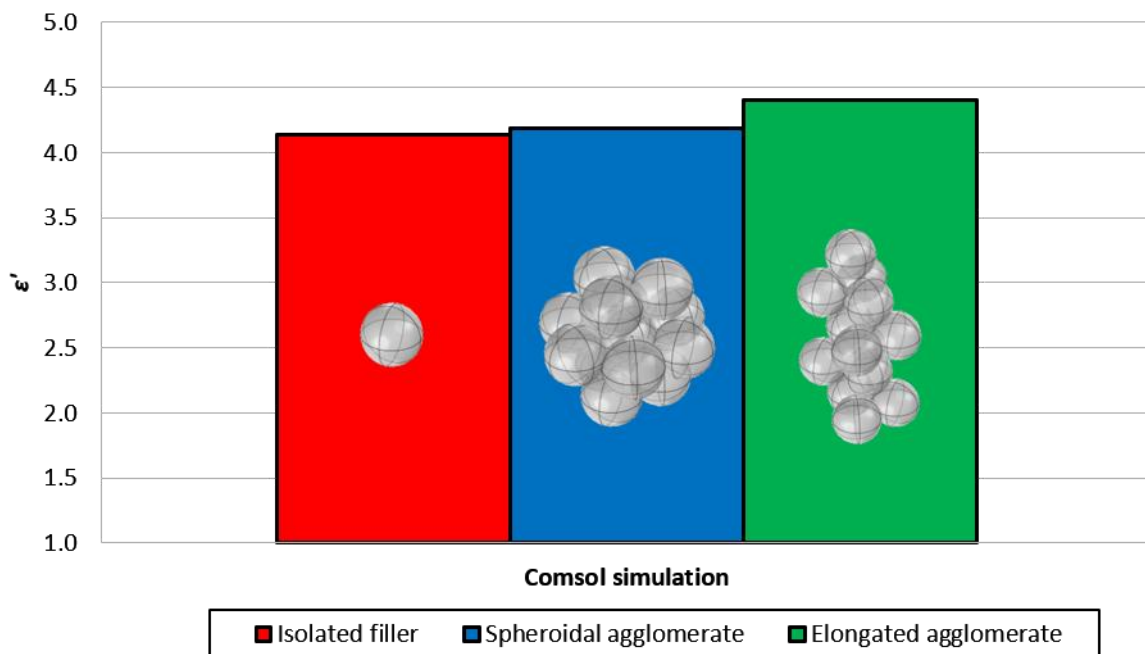
##### 4.3.3.5.1 Agglomerates of Spherical Particles

Spherical fillers were simulated to be aggregated into spheroidal agglomerates (see Figure 37 (left)) and elongated agglomerates (see Figure 37 (right)). Both agglomerates have the same number of equally sized spheres.



**Figure 37. Simulated composites with spherical fillers forming spheroidal (left) and elongated (right) agglomerates. Both agglomerates have the same number of equally sized spheres.**

In Figure 38, the permittivity of composites with volume concentration of 1 % of spherical filler in different configurations (isolated fillers, spheroidal agglomerates and elongated agglomerates) is shown. It can be observed how the permittivity of the composites with agglomerates is higher than the one with the isolated filler.



**Figure 38. Permittivity of composites with volume concentration of 1 % of spherical filler in different configurations: isolated fillers, spheroidal agglomerates and elongated agglomerates.**

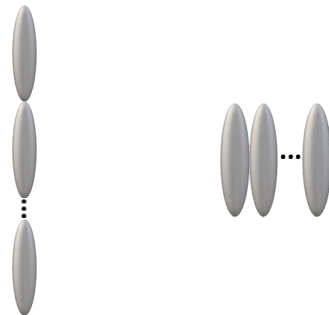


The spheroidal agglomerate, with an aspect ratio close to one, produces a smaller increase in permittivity with respect to the isolated filler than the elongated agglomerate, whose aspect ratio is much higher.

The permittivity of the composites with spheroidal and elongated agglomerates were equivalent to the permittivity predicted by the PvSB model for ellipsoidal fillers, parallel to the electric field, with aspect ratios 1.55 and 3.00, respectively. This result suggests that the increase of permittivity due to agglomeration (also observed in section 4.3.3.1) is influenced by the aspect ratio of the agglomerate. Thus, agglomerates can be considered in the PvSB model as ellipsoids with an apparent aspect ratio, as it will be discussed later in this chapter.

#### 4.3.3.5.2 Chains of Ellipsoidal Fillers

The formation of unidirectional chains of ellipsoidal fillers, parallel or perpendicular to the electric field, was also simulated (see Figure 39). All simulations were performed for a 0.1 % volume concentration of fillers, with chains including between one and twenty fillers.



**Figure 39. Chains of ellipsoidal fillers arranged parallel (left) and perpendicular (right) to the electric field.**

In Figure 40, the permittivity of composites with different unidirectional chains of fillers is shown as a function of the number of fillers per chain. It can be observed how the permittivity of vertical chain increases with the number of fillers in the chain (which increases the aspect ratio of the chain). For the horizontal chain, the value of permittivity remains almost constant. These results agree with the behaviour observed (experimentally (section 4.2.1) and in simulations (section 4.3.2.2) for isolated ellipsoids, suggesting that agglomerates follow a similar pattern: elongated shapes give rise to a major increase in permittivity when parallel to the electric field, and a lower increases in permittivity when perpendicular to it.

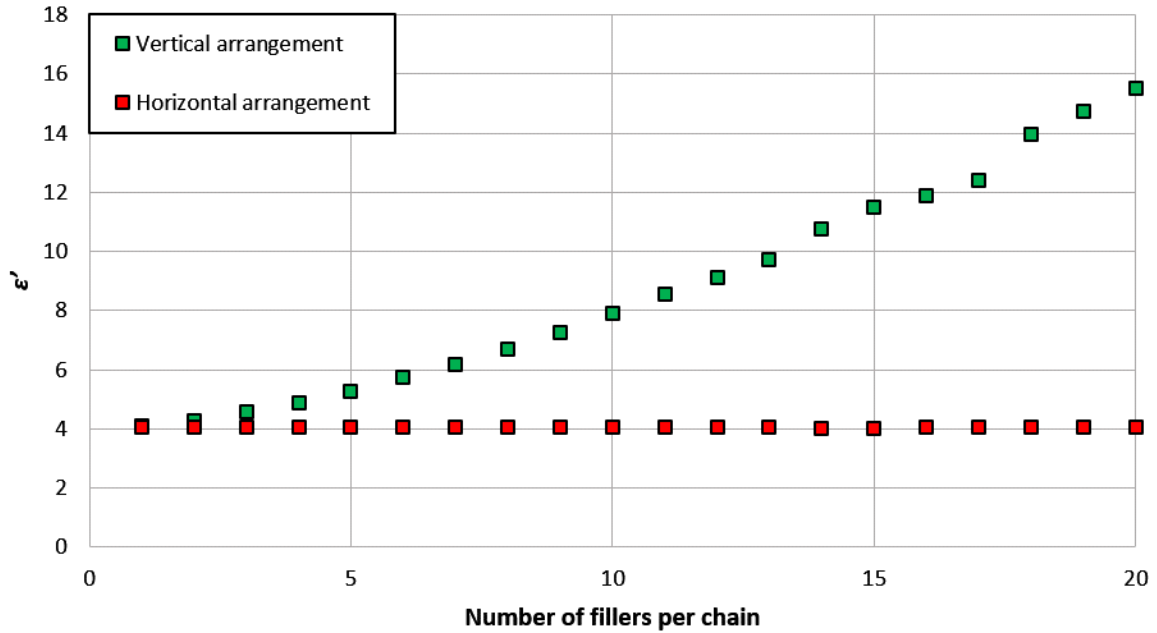


Figure 40. Permittivity of composites with different unidirectional chains of fillers as a function of the number of fillers per chain for a given volumetric concentration of 0.1 %.

#### 4.4 Extended PvSB Model (e-PvSB)

Attending to the results of the simulations in the previous section, most non-ideal features produce negligible effects on the permittivity of composites. Only the formation of conductive networks through contact between fillers give rise to relevant effects that must be incorporated into the model.

To account for the networking features of composites, a modification of the PvSB model is proposed, which will be described in this section.

The following hypothesis will be verified:

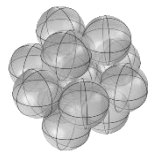
**The contribution of a given network of fillers to the permittivity of a composite equals the contribution of an isolated ellipsoid (with equal volume concentration and aspect ratio), which is a function of the geometry<sup>5</sup> of the network.**

<sup>5</sup> The number of contacts among fillers, the aspect ratio and orientation of individual fillers, as well as the effective aspect ratio and orientation of the network as a whole, are key elements of the geometry of the networks. It is therefore hard to provide a detailed equation to accounts for those elements.

In other words, a network of fillers can be substituted by a so-called equivalent ellipsoid.

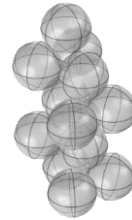
Figure 41 shows two different networks (already simulated in section 4.3.3.5.1) and their equivalent ellipsoids, as calculated from the results of simulations. The equivalent ellipsoid was considered to be parallel to the electric field. The network on the left (with spheroidal shape) is equivalent to an ellipsoid with aspect ratio 1.4, while the network on the right (elongated shape) has a higher aspect ratio, 2.7.

Spheroidal agglomerate



$$AR_{ee\parallel} = 1.4$$

Elongated agglomerate



$$AR_{ee\parallel} = 2.7$$

**Figure 41.** Spheroidal (left) and elongated (right) agglomerates. The aspect ratio of their equivalent ellipsoids parallel to the electric field ( $AR_{ee\parallel}$ ), as calculated with the PvSB model, are indicated.

In order to incorporate this idea into the PvSB model, a new parameter is included, the network factor ( $F_n$ ). It is defined as the ratio between the aspect ratio of the equivalent ellipsoid (parallel to the electric field) and the aspect ratio of the original filler:

$$F_n = \frac{AR_{ee\parallel}}{AR_f} \quad 4-16$$

Where  $AR_{ee\parallel}$  and  $AR_f$  are the aspect ratios of the equivalent ellipsoid and the isolated filler, respectively.

It is important to note that the equivalent ellipsoid has been defined to be parallel to the electric field. Therefore, values of network factor ( $F_n$ ) greater than one represent equivalent prolate ellipsoids parallel to the electric field, while values lower than one represent equivalent oblate ellipsoids parallel to the electric field (an oblate is said to be parallel to the electric field when its shorter axis is parallel to the electric field, i.e., when its plane is perpendicular to the electric field, as established in section 2.2.5).

The extended Polder/van Santen/Böttcher model (it would be referred to as e-PvSB) can be thus expressed as follows:

$$\bar{\varepsilon} = \varepsilon_m + (\varepsilon_f - \varepsilon_m) \nu d \left[ a_f \frac{\bar{\varepsilon}}{\bar{\varepsilon} + (\varepsilon_f - \bar{\varepsilon}) A_{f\parallel}} + (1 - a_f) \frac{\bar{\varepsilon}}{\bar{\varepsilon} + (\varepsilon_f - \bar{\varepsilon}) A_{f\perp}} \right] + (\varepsilon_f - \varepsilon_m) \nu (1 - d) \frac{\bar{\varepsilon}}{\bar{\varepsilon} + (\varepsilon_n - \bar{\varepsilon}) A_n} \quad 4-17$$

$$A_n = f(AR_f F_n) \quad 4-18$$

Where  $A_n$  is introduced as the depolarization factor of the equivalent ellipsoid, parallel to the electric field.




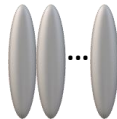





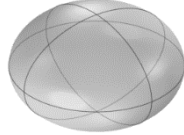
For conductive fillers in a non-conductive matrix below the percolation threshold, the e-PvSB can be simplified (see section 4.1.2) and the permittivity of the composite can be solved:

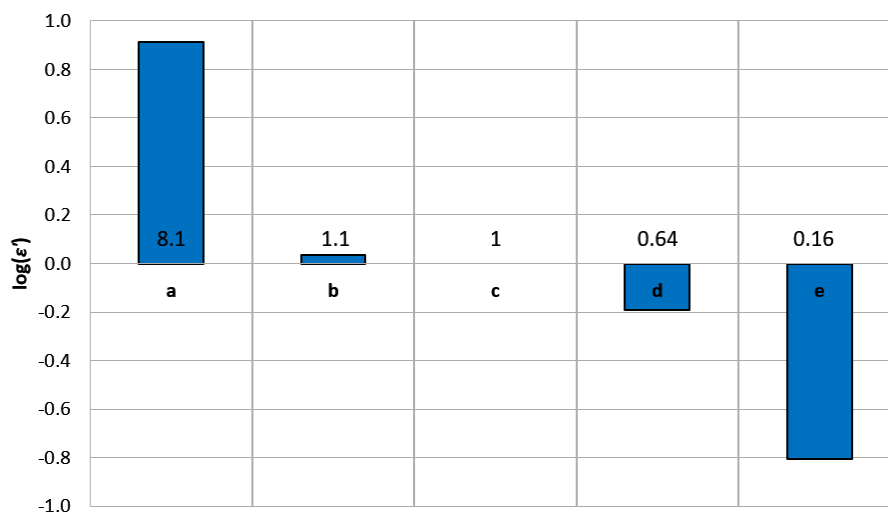
$$\bar{\varepsilon} = \frac{\varepsilon_m}{1 - \nu d \left[ \frac{a_f}{A_{f\parallel}} + \frac{(1 - a_f)}{A_{f\perp}} \right] + \frac{\nu(1 - d)}{A_n}} \quad 4-19$$

The equivalent ellipsoid that represents the network has been defined as parallel to the electric field, in order to minimize the number of parameters of the model. Otherwise, a new parameter must have been included: the alignment of the network. The model would then have been overparameterized.

In Table 5, different networks made of prolate ellipsoids are shown. Their respective equivalent ellipsoids and values of the network factor, as obtained from the results of simulations through the e-PvSB model, are included in Table 5 and plotted in Figure 42.

**Table 5.** Representation of the equivalent ellipsoid and their respective value of the network factor for different networks of prolate ellipsoids ( $AR = 5$ ): (a) 8 vertical fillers in a vertical arrangement (b) 8 horizontal fillers in a vertical arrangement (c) an isolated vertical filler (d) 8 vertical fillers in a horizontal arrangement (e) 8 horizontal fillers in a horizontal arrangement. The equivalent ellipsoid of (a) is not to scale due its large aspect ratio.

	a	b	c	d	e
Network					
Equivalent ellipsoid					
$F_n$	8.1	1.1	1.0	0.64	0.16
$AR_{eell}$	40.5	5.5	5.0	3.2	0.80



**Figure 42.** Network factor, in logarithmic scale, of the networks shown in Table 5.









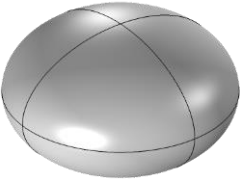
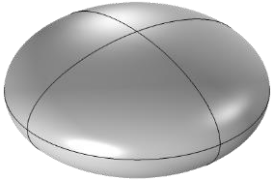
It must be noted that the network factor  $F_n$  does not only include information about the global aspect ratio of the network, but also from its orientation. A same network has different values

of  $F_n$  when rotated, as it is the case of networks (a) and (e), as well as networks (b) and (d), from Table 5.

It is also important to note that, although a given network has only one equivalent ellipsoid, a given equivalent ellipsoid does represent an infinite number of possible networks. A value of  $F_n$  can therefore not be associated to a specific network, but provides insights about its morphology: larger values of  $F_n$  imply networks elongated along the direction of the electric field.

In Table 6 different networks made of spheres are shown. Their respective equivalent ellipsoids and values of the network factor, as obtained from the results of simulations through the e-PvSB model, are included in Table 6 and plotted in Figure 43.

**Table 6. Representation of the equivalent ellipsoid and their respective value of the network factor for different networks of spheres: (a) 9 fillers in a vertical chain (b) 9 fillers in a vertical plane (c) an isolated filler (d) 9 fillers in a horizontal plane (e) 9 fillers in a horizontal chain.**

	a	b	c	d	e
Network					
Equivalent ellipsoid					
$F_n = AR_{eell}$	9.9	2.8	1.0	0.62	0.48

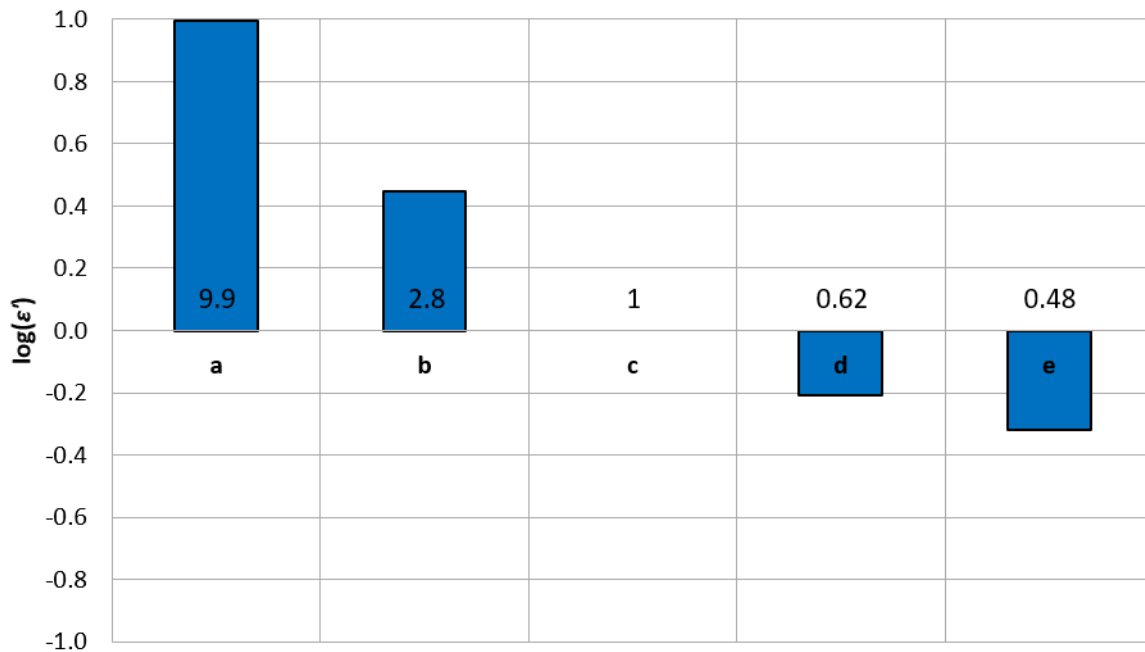


Figure 43. Network factor of the networks represented in Table 6.

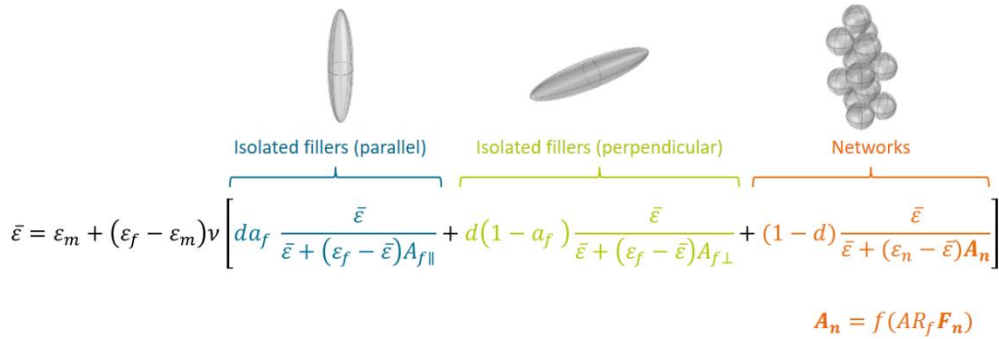
When the spheres associate themselves in structures that grow in the direction of the electric field, a value of the network factor  $F_n$  greater than one is obtained. On the contrary, when the spheres associate themselves in structures that grow in a direction perpendicular to the electric field, a value of  $F_n$  less than one than one is obtained.

Networks with values of  $F_n$  greater than one provide a larger increase of permittivity than networks with values of  $F_n$  less than one, as can be deduced from the depolarization factors of their equivalent ellipsoids.

#### 4.5 Method to Obtain Morphological Information from Experimental Data

The method to obtain morphological information of real composites using the e-PvSB model will be described in this section.

The e-PvSB model computes the dielectric properties of a composite as a function of the dielectric properties of filler and matrix, as well as the concentration, geometry, alignment and dispersion of the filler.



$$\bar{\epsilon} = \epsilon_m + (\epsilon_f - \epsilon_m)v \left[ da_f \frac{\bar{\epsilon}}{\bar{\epsilon} + (\epsilon_f - \bar{\epsilon})A_{f\parallel}} + d(1 - a_f) \frac{\bar{\epsilon}}{\bar{\epsilon} + (\epsilon_f - \bar{\epsilon})A_{f\perp}} + (1 - d) \frac{\bar{\epsilon}}{\bar{\epsilon} + (\epsilon_n - \bar{\epsilon})A_n} \right]$$

$$A_n = f(AR_f F_n)$$

Figure 44. Visual representation of the e-PvSB model (equations 4-17 and 4-18), featuring examples of fillers.

In typical experimental conditions, the dielectric properties of each material, as well as the concentration and geometry of the filler, are known. We will assume that experimental data of the permittivity of the composites at different concentrations of the filler are available. The permittivity of the composite and the filler concentration are therefore variables. Dispersion, alignment and network factor are unknown parameters, while other magnitudes are known constants (see Figure 45).

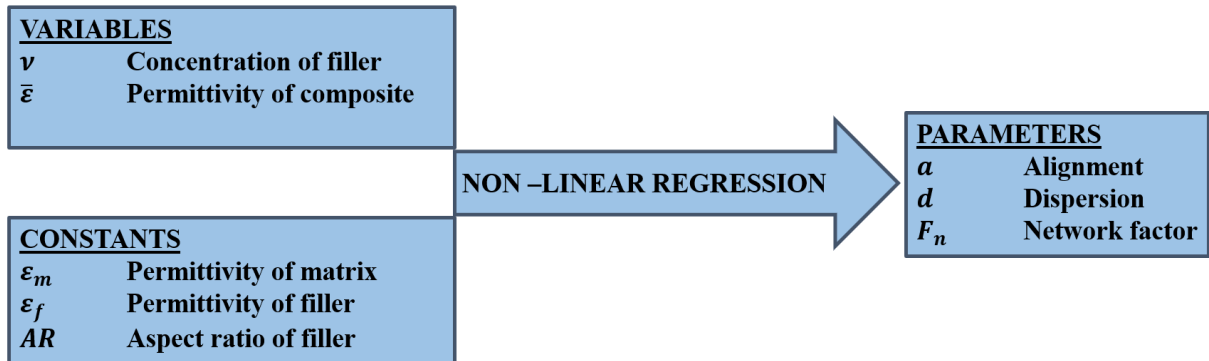


Figure 45. Method to obtain morphological information from experimental data using the e-PvSB model.

Dispersion, alignment and network factor will be determined by fitting the measured data to the model. We are considering a nonlinear regression problem with 2 variables, 3 unknown parameters and 3 constants. The generalized reduced gradient method [105] was used to minimize the coefficient of determination,  $R^2$ :

$$R^2 = 1 - \frac{\sum(y_i - \hat{y}_i)^2}{\sum(y_i - \bar{y})^2} \quad 4-20$$



Where  $y_i$  represents the experimentally observed values (observed permittivity),  $\hat{y}_i$  represents the predictions of the model (permittivity given by the e-PvSB model), and  $\bar{y} = \frac{1}{n} \sum_{i=1}^n y_i$  is the average of the  $n$  observed values. The closer the coefficient of determination is to 1, the better the model reproduces the experimental values.

An assumption must be made in order to do the regression analysis: the values of dispersion, alignment and network factor do not change with concentration. It is assumed that, because all composites are compounded and processed with the same parameters, the obtained alignment and dispersion will be at least similar.

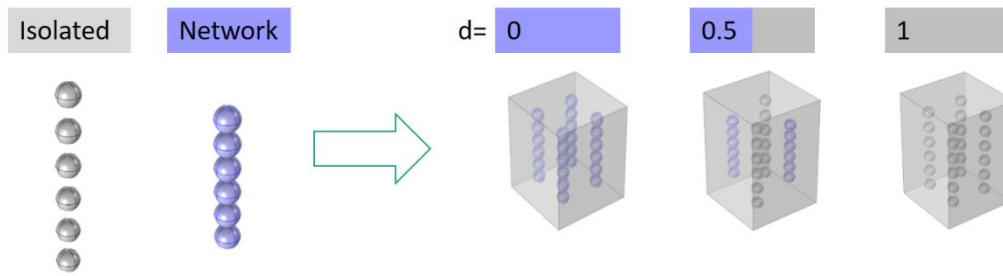
It must also be noted that the values of some magnitudes, like filler aspect ratio, alignment or dispersion, may be different for different regions of the composites or for individual units of filler. We always consider average or effective values of these magnitudes. The lower the standard deviation of these average values, the more exact the predictions of these analysis will be.

#### **4.5.1 Method Applied to Simulated Composites**

The e-PvSB model will be tested with data obtained from simulations. A nonlinear regression analysis will be performed as previously mentioned, using the values typically known from experimental conditions: the permittivity of the composite is measured for different values of filler concentration, while the dielectric properties of the materials and the aspect ratio of the filler are known constants.

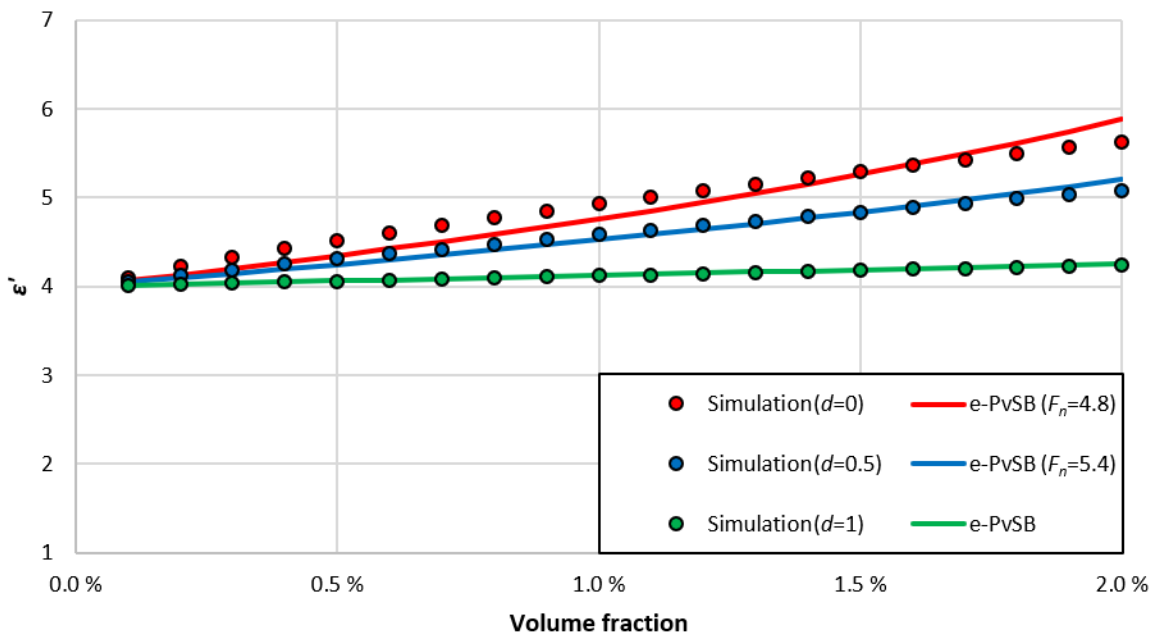
##### **4.5.1.1 Spherical Fillers with Varying Degrees of Dispersion**

In the first example, we will apply the model to spherical fillers (similar to the PLA/CB composites in chapter 4). Due to the meaninglessness of the alignment of spherical fillers, only dispersion and network factor are unknown variables. We will simulate the case in which the spherical fillers aggregate to form chains of six spheres that align parallel to the electric field (see Figure 46). Composites with different degrees of dispersion (0, 0.5, 1) were simulated.



**Figure 46. Spherical fillers: isolated (grey) and forming chains (blue). Simulated composites with different degrees of dispersion: 0, 0.5 and 1.**

In Figure 47, the simulated permittivity for different values of dispersion is plotted versus the filler concentration. The simulated data were fitted to the e-PvSB model by nonlinear regression, considering the dispersion as a known input (which is typically not the case in experimental conditions). In all three cases the model reproduces the simulated data within a 4 % error. A value of the network factor of  $5.1 \pm 0.3$  was found (through non-linear regression) to describe the simulated network.

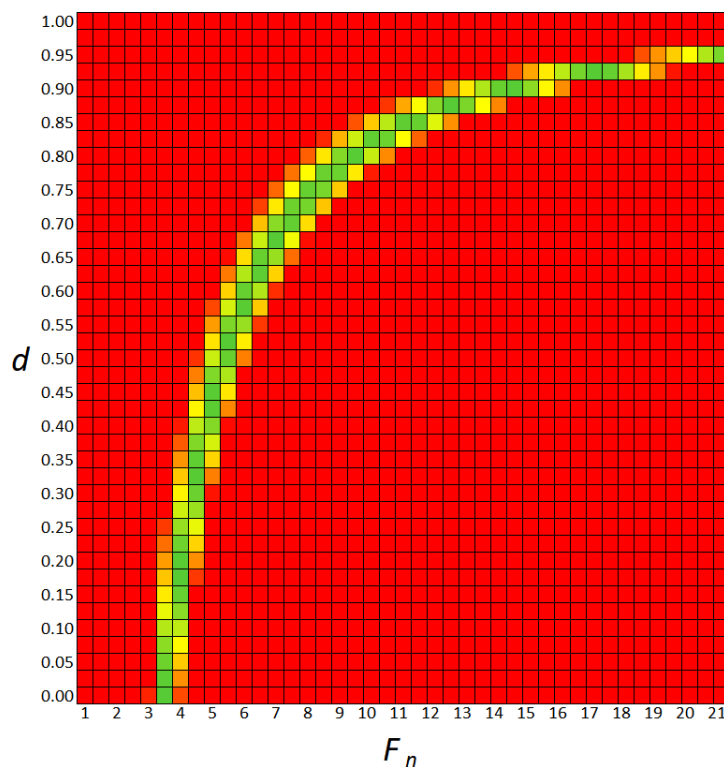


**Figure 47. Simulated and modelled permittivity for the composite represented in Figure 46. The values of dispersion (shown in this figure) were inputs to the e-PvSB model. A value of  $F_n = 5.1 \pm 0.3$  was found for the network (for  $d = 1$  there is no network and  $F_n$  is therefore not defined).**

However, the value of dispersion is typically unknown in experimental conditions, so that two parameters, dispersion and network factor, are to be found through the nonlinear regression. Unfortunately, different combinations of the values of dispersion and network factor can

provide the same permittivity versus concentration curve (as proved in Appendix A). This means that it is impossible to determine the real values of dispersion and network factor from experimental data. Instead, only the set of all the possible solutions can be found.

In order to find the different solutions to the fitting problem, the coefficient of determination ( $R^2$ ) of the e-PvSB model with respect to the simulated data was calculated for different combinations of dispersion and network factor (see Figure 48), for composite simulated with a degree of dispersion of 0.5). Each square represents a combination of values for dispersion (vertical axis) and network factor (horizontal axis), while its colour represents the value of the coefficient of determination, ranging from red ( $R^2 \leq 0.7$ , insufficient fitting) to green ( $R^2 = 1$ , perfect fitting), going through yellow ( $R^2 = 0.9$ , acceptable fitting). Thus, hybrid colours between yellow and green represent values of the coefficient of determination between 0.9 and 1.



**Figure 48.** Matrix of coefficients of determination ( $R^2$ ) of the e-PvSB model with respect to a simulated composite (with  $d = 0.5$ ) for different combinations of dispersion ( $d$ ) and network factor ( $F_n$ ). Colours represent the value of the coefficient of determination, ranging from red ( $R^2 \leq 0.7$ , insufficient fitting) to green ( $R^2 = 1$ , perfect fitting), going through yellow ( $R^2 = 0.9$ , acceptable fitting).

The green line that emerges in Figure 48 represents the combination of possible solutions to the regression problem. In Figure 49, the line of possible solutions of the three simulated

composites of Figure 46 is shown. The line was obtained by selecting the value of dispersion that provides the greatest value of  $R^2$  for each considered value of  $F_n$ . The matrices of coefficients of determination for the composites with dispersion 0 and 1 can be found in Appendix B.

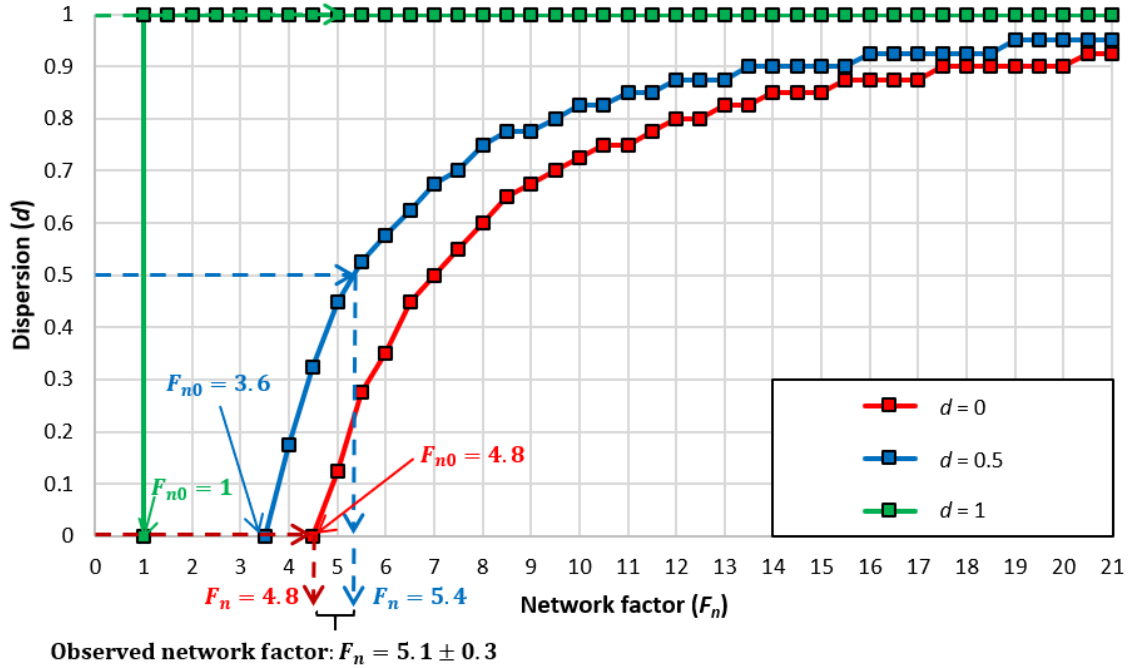


Figure 49. Different possible combinations of dispersion and network factor that fit the simulated composites of Figure 46 (with  $d = 0$ ,  $d = 0.5$  and  $d = 1$ ) according to the e-PvSB model. The real solutions are indicated (dashed lines). The value of  $F_{n0}$  (network factor for  $d = 0$ ) is also indicated.

In the next section, the reference network factor ( $F_{n0}$ ) will be introduced and its potential to provide information from composites with unknown morphology will be discussed.

#### 4.5.1.2 Reference Network Factor

In the previous case (Figure 49), the real values of dispersion cannot be determined, but the locus of solutions are clearly different for the three composites. Each curve can be unequivocally described by the value of the network factor when the dispersion is 0 (proof in Appendix A), i.e., when no isolated fillers are present in the composite:

$$F_{n0} \equiv F_n(d = 0)$$

The reference network factor ( $F_{n0}$ ) of a composite is defined as the network factor of a fictitious composite with null dispersion and identical properties to the original composite. In other words, if the network factor ( $F_n$ ) represents an equivalent ellipsoid that describes the average

effect of all the networks in a composite,  $F_{n0}$  represents an equivalent ellipsoid that describes the average effect of both the networks and the isolated fillers in a composite.

The method previously proposed (Figure 45) to obtain morphological information from experimental data using the e-PvSB model can thus be updated by introducing the reference network factor.

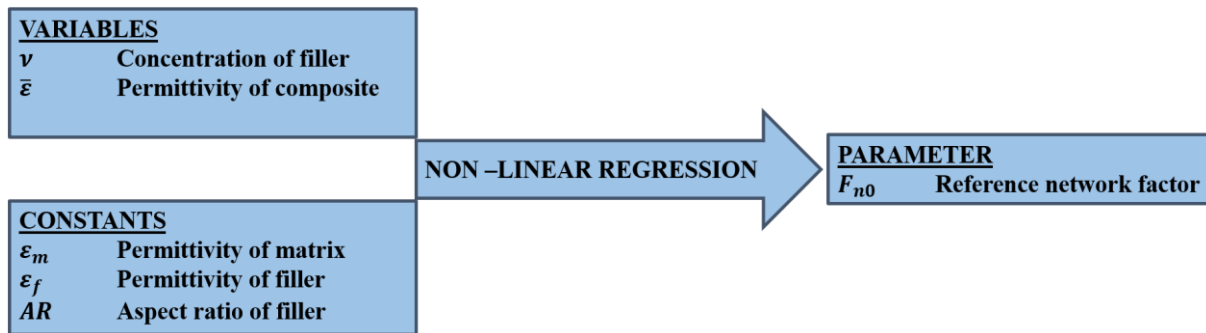


Figure 50. Updated method to obtain morphological information from experimental data using the e-PvSB model. The reference network factor ( $F_{n0}$ ) includes the effects of alignment ( $a$ ), dispersion ( $d$ ) and network factor ( $F_n$ ).

#### 4.5.1.3 Ellipsoidal Fillers with Varying Degrees of Alignment

In this case, we will apply the model to prolate ellipsoidal fillers (similar to the composites with CNTs in chapters 5 and 6). Unlike the case of spherical fillers, the orientation of the fillers is a relevant factor in this case. We will assume that the ellipsoidal fillers do not aggregate ( $d = 1$ ). Different values of the alignment parameter ( $a$ ) will be considered (see Figure 51): 1 (parallel to electric field),  $1/3$  (random orientation) and 0 (perpendicular to electric field). The case of random orientation is equivalent to an angle of  $63.43^\circ$  (as derived in footnote 4 in page 47).

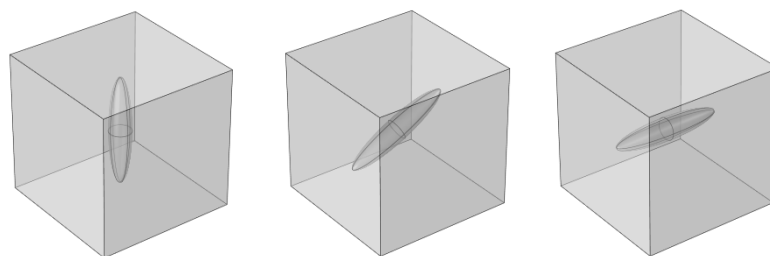
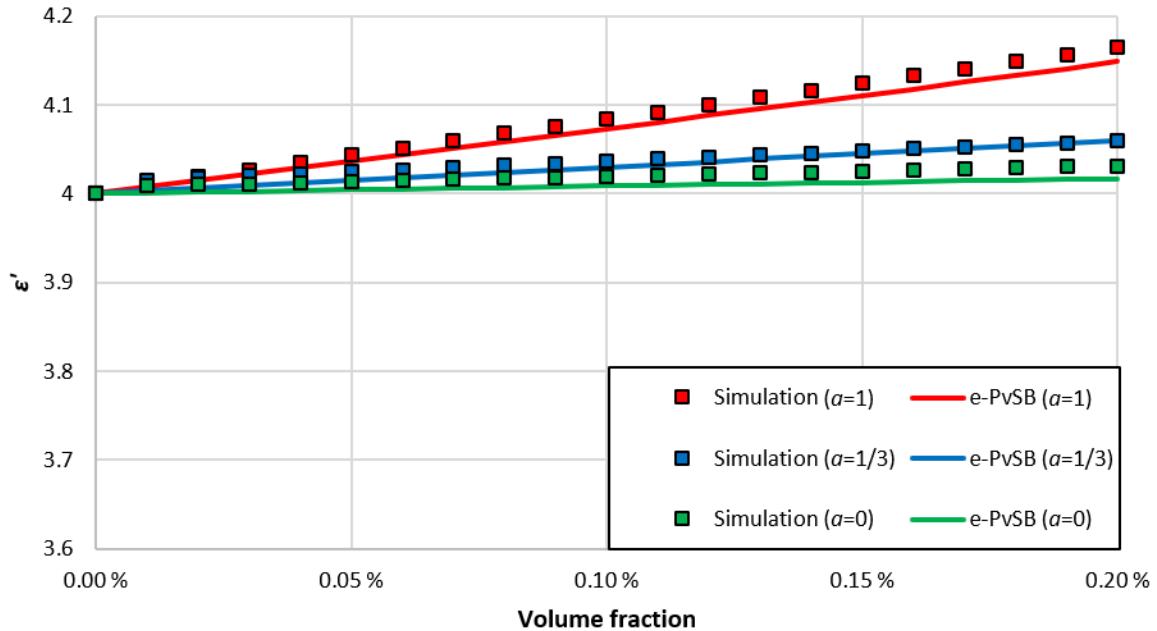


Figure 51. Simulated composites with ellipsoidal fillers with different values of the alignment parameter ( $a$ ): 1, parallel to electric field (left);  $1/3$ , random orientation (middle); and 0, perpendicular to electric field (right).

In Figure 52, the simulated permittivity for different values of alignment is plotted versus the filler concentration. The simulated data were fitted to the e-PvSB model by nonlinear regression, considering the alignment as a known input and assuming a perfect dispersion. In all three cases the model reproduces the simulated data within a 0.4 % error.



**Figure 52.** Simulated and modelled permittivity for the composite represented in Figure 51. The values of alignment (shown in the figure) and dispersion ( $d = 1$ ) were inputs to the e-PvSB model.

However, analogously to the example in the previous section, the values of alignment and dispersion are typically unknown in experimental conditions, so that three parameters (dispersion, alignment and network factor), are to be found through the nonlinear regression. In this case, different triplets of values of (dispersion, alignment, network factor) are solutions to the regression problem, i.e., the real values of these parameters cannot be determined.

In order to obtain useful information from the measured (in this case simulated) data of permittivity, the  $F_{n0}$  will be calculated. Thus, the different degrees of alignment of the simulated composites will be described in terms of equivalent ellipsoids.

In Figure 53, the locus of the possible solutions (with  $a = 1$ ) for the three simulated composites is shown. Using any other value of  $a$  (alignment of the dispersed fillers) would have no effect in the determination of  $F_{n0}$ , as it is defined for a null dispersion, i.e., it is defined for a fictitious composite in which there are no dispersed fillers.

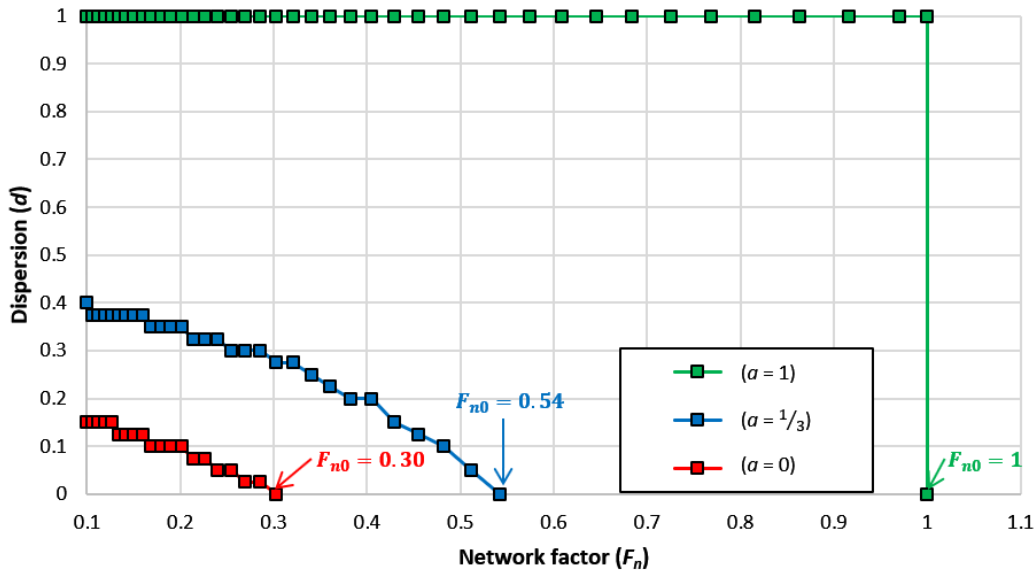


Figure 53. Different possible combinations of dispersion and network factor that fit the simulated composites of Figure 51 (with  $a = 1$ ,  $a = 1/3$  and  $a = 0$ ) according to the e-PvSB model. The value of  $F_{n0}$  (reference network factor) is also indicated.

It must be noted how lower values of  $F_{n0}$  are associated perpendicular alignment, while higher values of  $F_{n0}$  are associated with parallel alignment.

In Table 7, the values of  $F_{n0}$  are related to their corresponding effective ellipsoids.

Table 7. Effective ellipsoids corresponding to each degree of alignment.

Real filler	$a = 0$	$a = 1/3$	$a = 1$
Effective ellipsoid	$F_{n0} = 0.30$ (AR = 1.5) 	$F_{n0} = 0.54$ (AR = 2.7) 	$F_{n0} = 1$ (AR = 5) 

The relation between  $F_{n0}$  and  $a$  observed in Figure 53 is derived in Appendix A (equation A-4).

## 4.6 Discussion

An effective medium model – Polder/van Santen/Böttcher (PvSB) model [59], [60] – has been considered to predict the dielectric properties of composites as a function of filler dispersion and orientation.

The PvSB model can incorporate the geometry of typical conductive nanofillers like carbon nanotubes, graphene or carbon black. It can predict the dielectric properties of composites with higher concentrations better than other kind of models, like mean field models (Wagner/Sillars model [54], [55]; Fricke model [62], [89]), based on the Maxwell/Garnett approximation [90], which is only applicable for dilute composites.

The model was reformulated and two parameters, alignment and dispersion, were defined in terms of the components of the model.

The PvSB model was experimentally validated. Macroscopic composite materials, in which conductive fillers were deliberately placed to obtain controlled values of concentration, orientation and dispersion, were fabricated. Their measured dielectric properties agree accurately with the prediction of the PvSB model. These results complement previous findings [57], where the PvSB model agree with experimental data from composites with non-conductive fillers.

The PvSB model was compared to simulations. Composites with the ideal dispersion characteristics assumed by the PvSB model were simulated using Comsol Multiphysics<sup>®</sup>. The results of simulations with different filler concentrations, shapes and orientations agree accurately with the predictions of the PvSB model, except for high concentrations, where the results of model and simulations start to deviate.

The observed deviations at high concentrations is a known limitation of the PvSB model [106]. The PvSB model only considers the ideal condition in which the fillers are evenly distributed in a matrix, with no contact among them. These contacts become more and more probably as the concentration of fillers rises.

Several non-ideal features (see section 4.3.3), which are ignored in the PvSB model, were simulated. Most of the considered features resulted in negligible effects on the dielectric properties of the composites. Only the connection between conductive fillers to form networks



produced relevant effects that must be incorporated into the model. These conductive networks produce a strong alteration in the electric field inside composites with respect to the electric field considered by the PvSB model.

An extension of the PvSB is proposed in this thesis to include the effect of network formation of fillers. Based on the simulations of non-ideal composites, a mathematical representation of conductive networks is introduced: networks are represented as equivalent ellipsoidal fillers that have the same effect on the permittivity of the composite (see section 4.4). A new parameter is introduced, namely the network factor. The network factor is determined by the geometry of the network and relates it to an equivalent ellipsoidal filler. The so modified PvSB model will be referred to as the extended Polder/van Santen/Böttcher (e-PvSB) model.

Percolation and fractal theories are alternative theories that can accurately describe the properties of composites with conductive fillers. However, their applicability to infer morphological information from experimental data is limited (this is extensively analysed by Nan in [107]). Percolation theories assumes that fillers are randomly distributed, while fractal theories imply that filler form self-similar networks, which is not always the case. McLachlan [76] proposed an empirical equation combining percolation theories with effective medium theories (thus overcoming the random nature of percolation theories). However, this equation applied only to the resistivity of composites.

In this chapter, a methodology is proposed to use the e-PvSB model to obtain morphological information from experimental data. The concept of reference network factor is introduced, in order to synthesize the information of orientation, alignment and network factor in a single parameter. The reference network factor can be obtained by a nonlinear regression analysis of experimental data and can be used to compare the morphology of similar composites.

Different filler morphologies result in the same values of permittivity versus concentration. This implies that the real morphology of a composite cannot be unequivocally deduced from experimental data. However, the method proposed in this chapter has practical applications in analysing composites with conductive fillers, as discussed in section 7.

The method was successfully tested on data obtained from simulations to study composites with different degrees of dispersion and orientation. In the next sections, the method is applied to experimental data of composites with different degrees of dispersion (section 5) and alignment (section 6).



## 5. Analysis of dispersion

In this chapter, the e-PvSB model will be applied to obtain morphological information from composites with different degrees of filler dispersion.

### 5.1 Nanocomposites

PLA/MWNT and PLA/CB composites were produced with good and bad dispersion (see chapter 3) and the e-PvSB model was applied to detect the difference in dispersion. MWNTs and CB, which can be modelled as prolate ellipsoids and spheres, respectively, were chosen in order to study the effect of different aspect ratios on the permittivity of composites.

### 5.2 Microscopy

Scanning electron microscopy (SEM) and transmission optical microscopy (TOM) were used in order to obtain information on the morphology of the fillers in the composites.

#### 5.2.1 Scanning Electron Microscopy

The composites were characterized using SEM. The sample preparation and the microscope settings are specified in section 3.3.

##### 5.2.1.1 PLA/MWNT Composites

In Figure 54 and Figure 55, SEM images of PLA composites with mass concentration of 1 % on MWNTs with good and bad dispersion are shown at different magnifications. Agglomerates with sizes in the order of tens of micrometres can be observed as bright (conductive) regions. Individual bright tubular structures can be observed within and outside agglomerates. The tubular structures feature an apparent diameter that was measured to be in the order of 80 nm. The diameter of MWNT according to the provider lies around 9.5 nm. Hence, the observed structures are arguably bundles of MWNTs, rather than individual MWNTs.

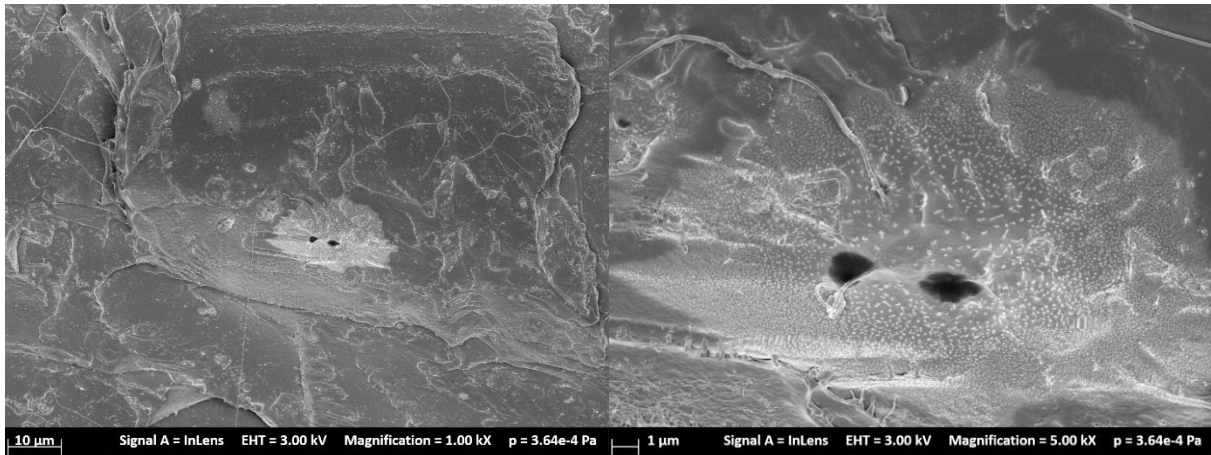


Figure 54. SEM images of PLA composites with a MWNT mass concentration of 1 % and good dispersion.

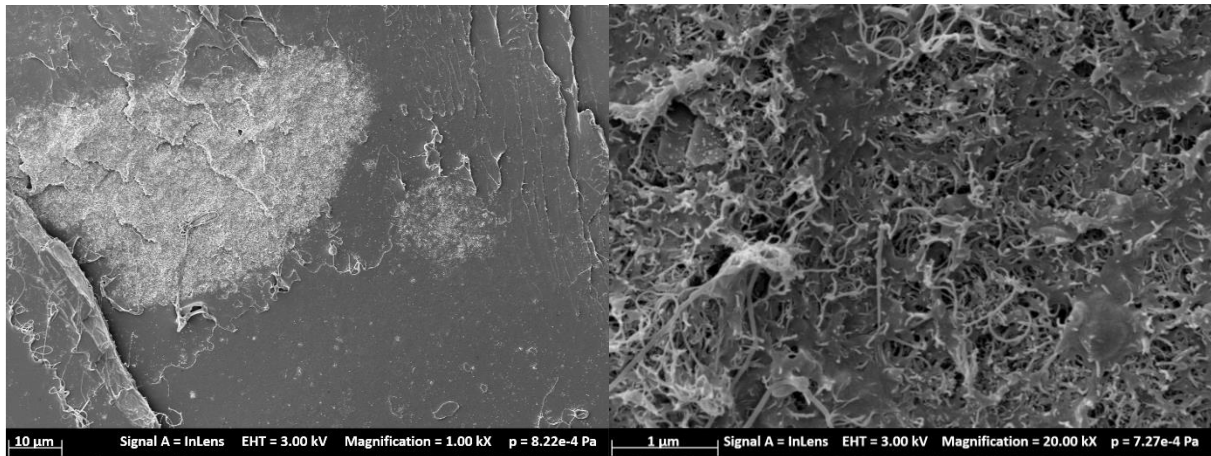


Figure 55. SEM images of PLA composites with a MWNT mass concentration of 1 % and bad dispersion. The long tubular structures observed on the bottom left corner of the image on the left are polymer structures produced during the sample fracturing.

In the composite with bad dispersion, larger agglomerates are observed. A mesh of MWNT bundles are observed within these agglomerates. In comparison, agglomerates in the composite with good dispersion feature better dispersed MWNTs. No alignment of the filler is observed in both composites.

### 5.2.1.2 PLA/CB Composites

In Figure 56 and Figure 57, SEM images of PLA composites with mass concentration of 1 % on CB with good and bad dispersion are shown at different magnifications. Agglomerates with sizes in the order of tens of micrometres can be observed as bright (conductive) regions. Individual bright spherical structures can be observed within and outside agglomerates, corresponding to individual particles of carbon black.

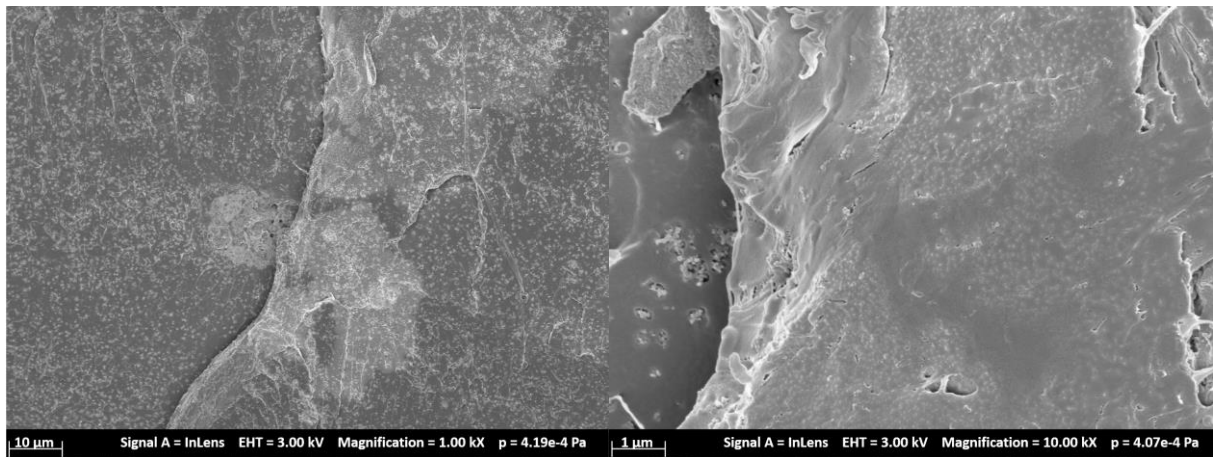


Figure 56. SEM images of PLA composites with a CB mass concentration of 1 % and good dispersion.

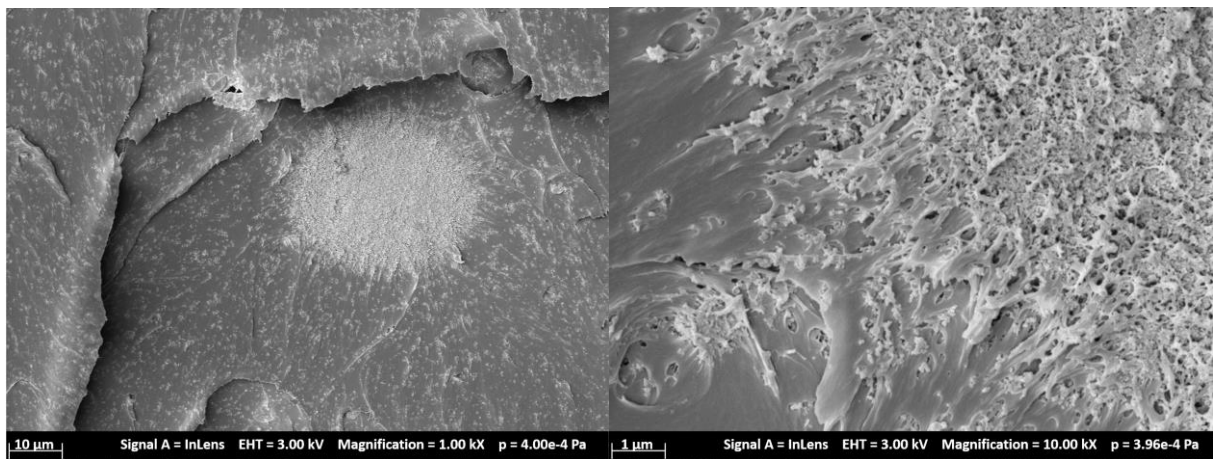


Figure 57. SEM images of PLA composites with a CB mass concentration of 1 % and bad dispersion.

In the composite with bad dispersion, larger agglomerates are observed. A mesh of CB particles is observed within these agglomerates. In comparison, agglomerates in the composite with good dispersion show better dispersed CB particles. In some cases, small networks of tens of CB particles are observed.

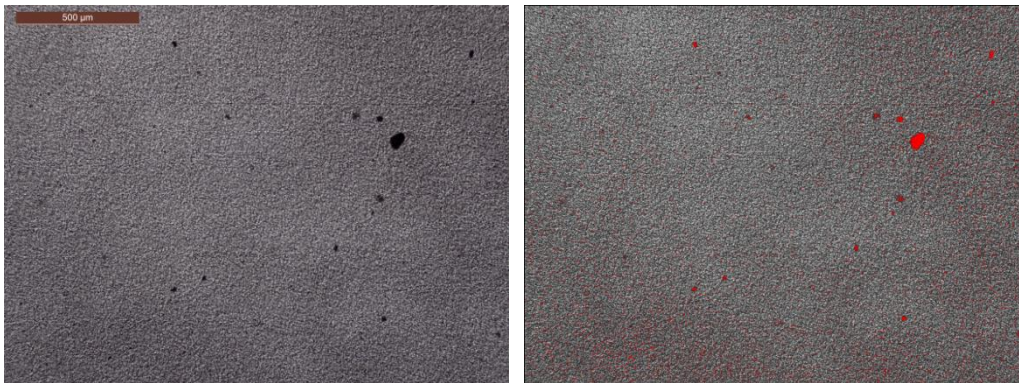
## 5.2.2 Transmission Optical Microscopy

The composites were characterized using TOM. The sample preparation and the microscope settings are specified in section 3.3.

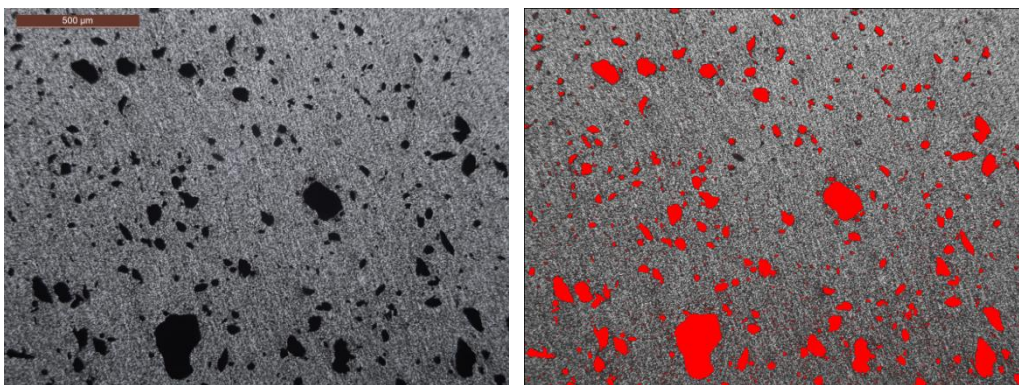
### 5.2.2.1 PLA/MWNT Composites

In Figure 58 and Figure 59, TOM images of PLA composites with mass concentration of 1 % on MWNTs with good and bad dispersion are shown. Black regions represent agglomerates. Individual filler particles are too small to be detected. Light regions represent zones where no

agglomerates of detectable size are present, i.e., they may contain isolated particles or non-observable agglomerates.



**Figure 58. TOM images of PLA composites with a MWNT mass concentration of 1 % and good dispersion: (left) original image and (right) image after computer analysis to detect agglomerates.**



**Figure 59. TOM images of PLA composites with a MWNT mass concentration of 1 % and bad dispersion: (left) original image and (right) image after computer analysis to detect agglomerates.**

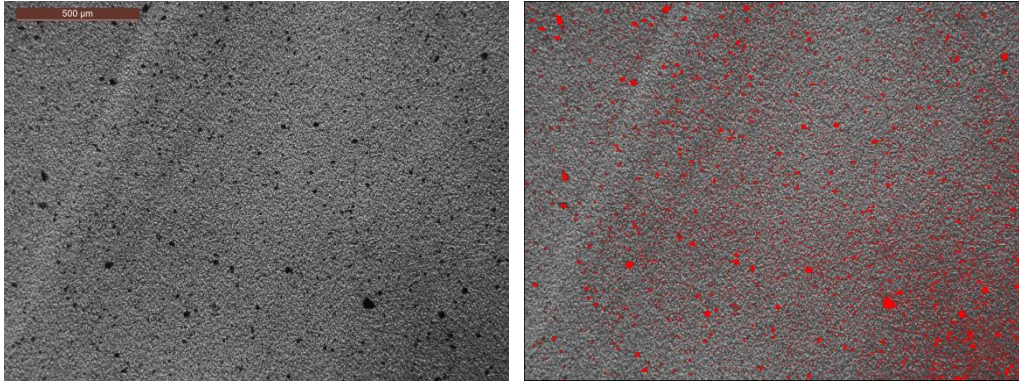
For each composite, ten images were computationally analysed according to the method described in section 3.3.3 to detect agglomerates (see right images of Figure 58 and Figure 59). The fraction of observable agglomerate area was found to be  $0.5 \pm 0.3$  % and  $7 \pm 2$  % for the composites with good and bad dispersion, respectively. Although the fraction of agglomerate area cannot be directly translated into a volume fraction, it is safe to state that the sample with bad dispersion has more agglomerates, or at least larger agglomerates. The results agree with the morphology expected for the fabrication process of each composite.

### 5.2.2.2 PLA/CB Composites

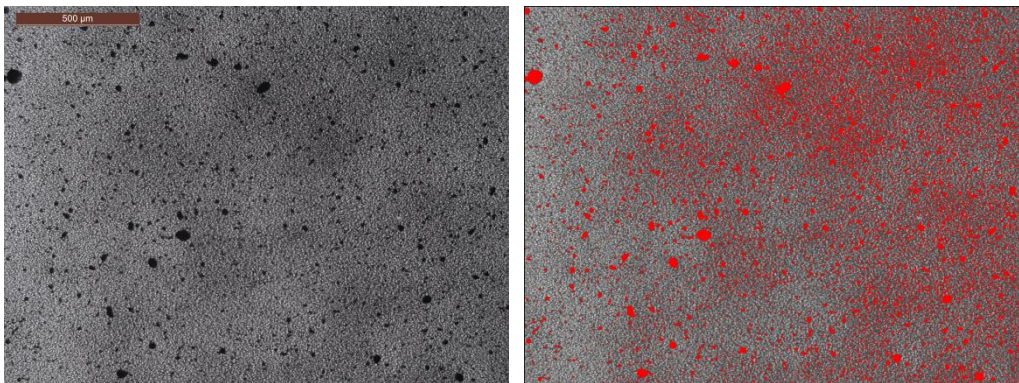
In Figure 60 and Figure 61, TOM images of PLA composites with mass concentration of 1 % on CB with good and bad dispersion are shown. Black regions represent agglomerates.



Individual filler particles are too small to be detected. Light regions represent zones where no agglomerates of detectable size are present, i.e., they may contain isolated particles or non-observable agglomerates.



**Figure 60. TOM images of PLA composites with a CB mass concentration of 1 % and good dispersion: (left) original image and (right) image after computer analysis to detect agglomerates.**



**Figure 61. TOM images of PLA composites with a CB mass concentration of 1 % and bad dispersion: (left) original image and (right) image after computer analysis to detect agglomerates.**

For each composite, ten images were computationally analysed according to the method described in section 3.3.3 to detect agglomerates (see right images of Figure 60 and Figure 61). The fraction of observable agglomerate area was found to be  $3\pm 1\%$  and  $14\pm 1\%$  for the composites with good and bad dispersion, respectively. The results agree with the morphology expected for the fabrication process of each composite.

### 5.3 Dielectric Spectroscopy

In this section, the results of dielectric spectroscopy are presented and discussed. The dielectric spectra were measured as described in section 3.3.1.1, between 1 Hz and 1 MHz.

### 5.3.1 Dielectric Spectra

In Figure 62, the dielectric spectra of PLA and PLA composites with 0.1 % MWNT and 0.1 % CB mass concentrations and good dispersion are plotted versus frequency. It can be observed how the values of relative permittivity are almost flat, with a slightly decreasing slope with respect to frequency and are parallel for the three materials. The composites have a higher value of relative permittivity than the unfilled polymer, which can be explained in terms Maxwell/Wagner polarization processes (see section 2.1.5.3 for more details). The magnitude of the increase in permittivity of the composite with respect to the pure polymer can be accounted for by the e-PvSB model. This increase is a function of the filler's dielectric properties, geometry and concentration, as discussed in chapter 4.

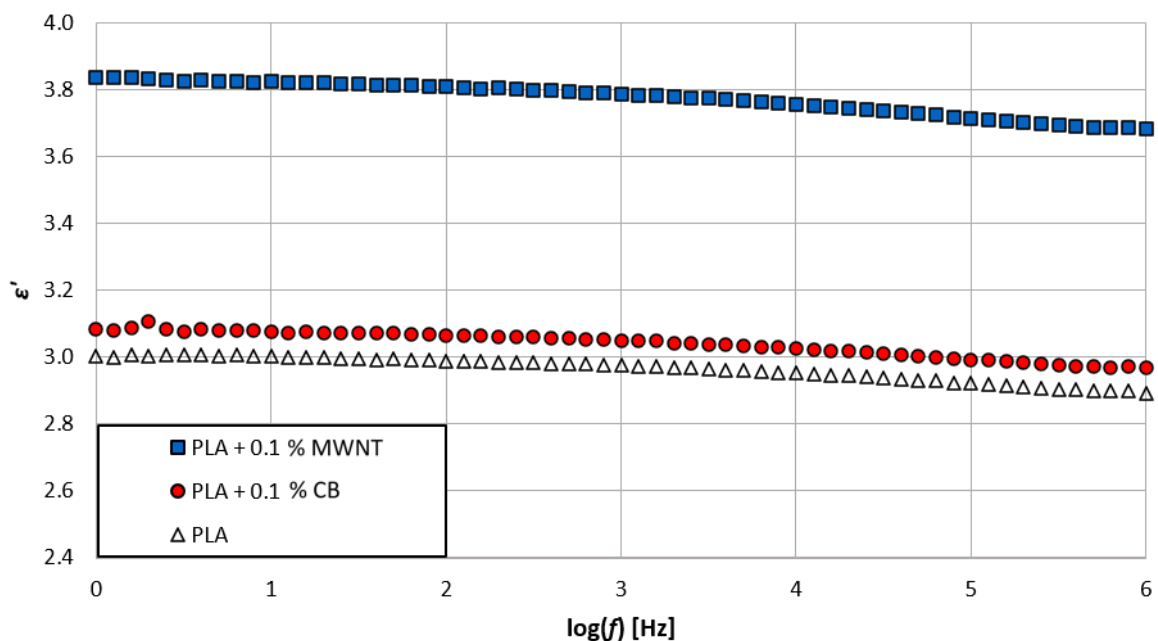


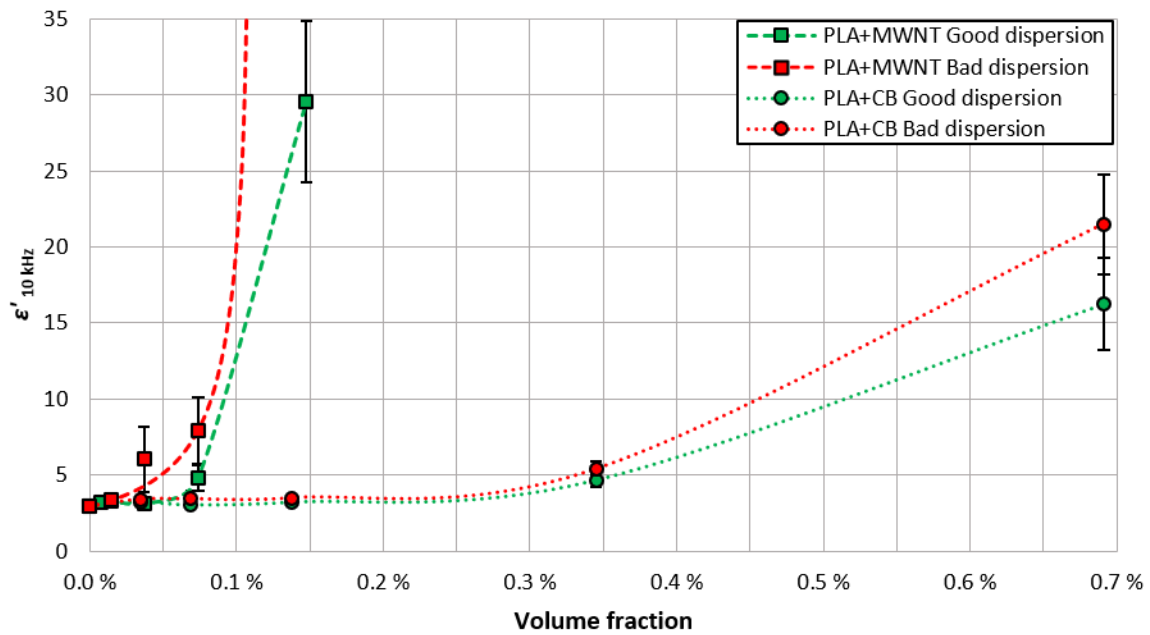
Figure 62. Dielectric spectra of PLA and PLA composites with 0.1 % MWNT and 0.1 % CB mass concentrations and good dispersion.

### 5.3.2 Permittivity versus Concentration

In Figure 63, the permittivity of PLA composites with MWNT and CB is shown as a function of concentration, for good and bad dispersion. The values of permittivity were considered at an arbitrary frequency (10 kHz) for convenience. Due to the parallel and almost flat dielectric spectra shown in Figure 62, choosing other frequencies does not alter the conclusions of this chapter.



PLA/MWNT composites were measured for volume concentrations between 0.01 % and 0.15 %, while PLA/CB composites were measured for volume concentrations between 0.03 % and 0.69 %. The volume concentrations were calculated as described in section 3.3.1. The highest measurable concentration is determined by the percolation threshold of each composite, as discussed in section 3.3.1.1.



**Figure 63. Measured permittivity of PLA composites with MWNT and CB, with good and bad dispersion, for different volume concentrations. Error bars are the standard deviation of 4 samples and are visible when the error is larger than the marker size. Lines are a visual guidance.**

It can be observed how the permittivity increases with concentration, especially when approaching the percolation threshold, where the measuring errors increase until the determination of the permittivity is no longer possible. The shape of the curve is compatible with the e-PvSB model, as shown in the next section.

It must be noted that the percolation threshold is higher for the PLA/CB than for the PLA/CNT, as expected by for CB's lower aspect ratio [12], [108]–[111].

The composites with bad dispersion show higher values of permittivity than the composites with good dispersion. This effect will be explained in the next section by fitting the measured data to the e-PvSB model.

### 5.3.3 Analysis with e-PvSB Model

In this section, the e-PvSB model will be applied to obtain morphological information from the measured dielectric values, using the method described in section 4.5.

#### 5.3.3.1 PLA/MWNT Composites

The reference network factor ( $F_{n0}$ ) for the PLA/MWNT composites was calculated by fitting the experimental data from Figure 63 to the e-PvSB model. In Figure 64, the set of combinations of dispersion and network factor that reproduces the experimental data, for both good and bad dispersion, is represented (the corresponding matrices of coefficients of determination are shown in Appendix B.) As discussed in section 4.5, it is not possible to discern which of all the possible solutions most accurately describe the real morphology of the composites. Instead, the  $F_{n0}$  is calculated. For the elaboration of Figure 64, it was assumed that isolated MWNTs were randomly oriented. However, it has no influence on the value of  $F_{n0}$  (as previously defined,  $F_{n0}$  is the equivalent network factor of a fictitious composite with null dispersion, i.e., when no individual MWNT is isolated in the matrix).

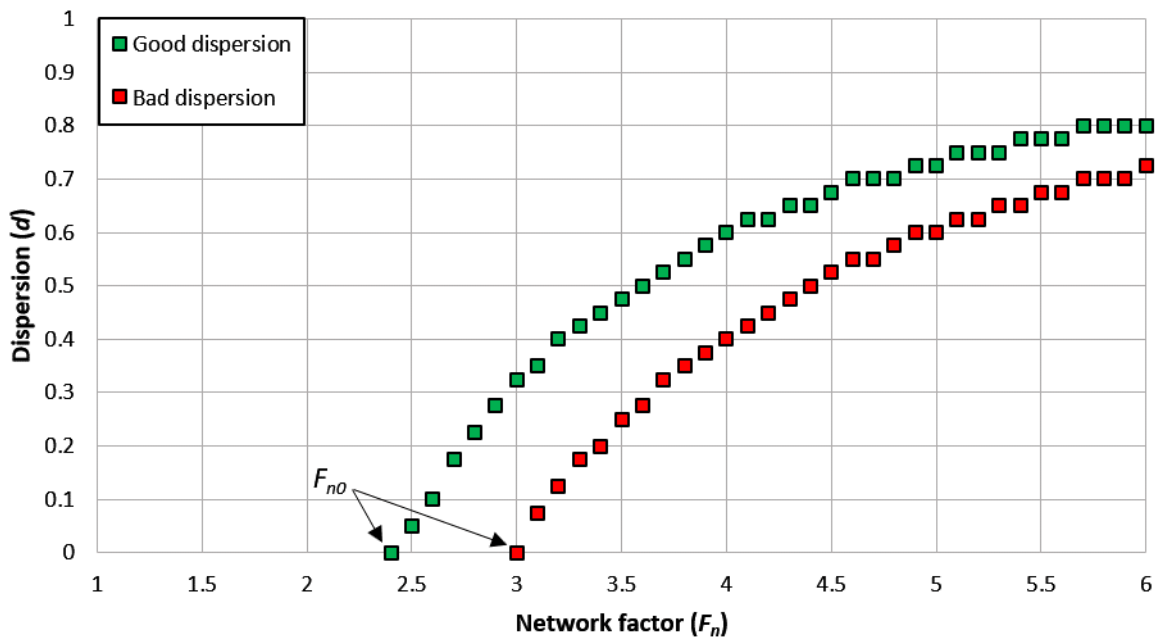


Figure 64. Different possible combinations of dispersion  $d$  (vertical axis) and network factor  $F_n$  (horizontal axis) that describe the measured permittivity of the PLA/MWNT composites of Figure 63.

The observed values of  $F_{n0}$  were  $2.44 \pm 0.01$  and  $2.99 \pm 0.01$ , for the composites with good and bad dispersion, respectively. As expected, the  $F_{n0}$  of the composite with bad dispersion is larger

than the  $F_{n0}$  of the composite good dispersion. It must be remembered that any possible orientation of the fillers or agglomerates is included in the observed value of  $F_{n0}$ . However, due to the fabrication process, the orientation in both composites is expected to be similar and probably close to a random orientation.

In Figure 65, the experimental data and the corresponding values provided by the e-PvSB model are represented. The coefficients of correlation are 0.99 and 0.82 for the composite with good and bad dispersion, respectively.

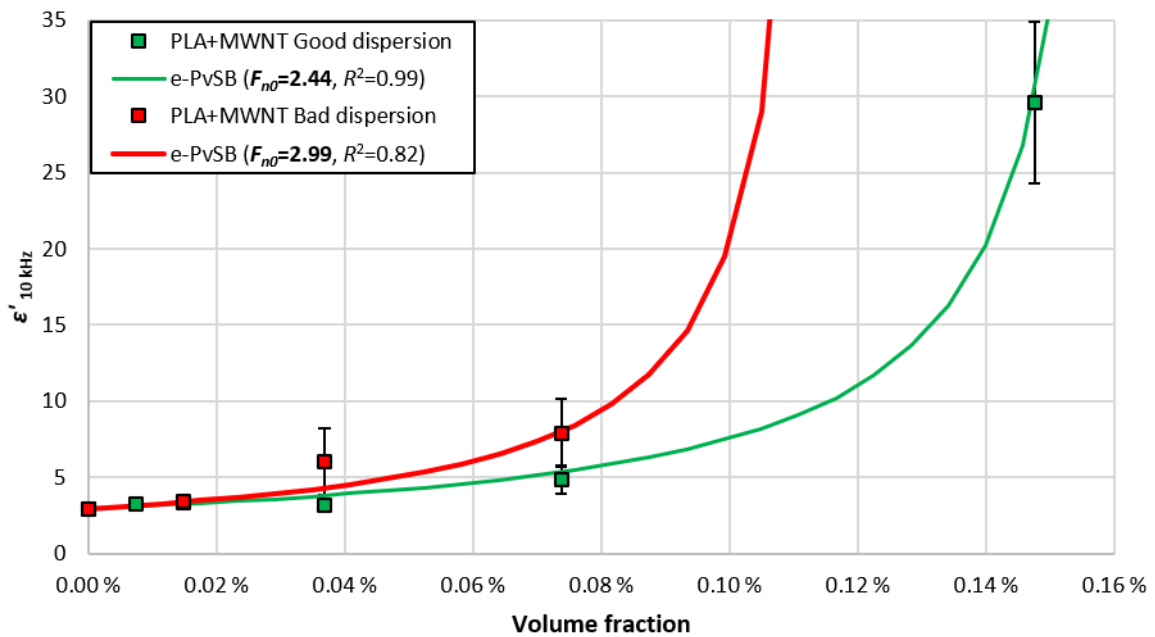
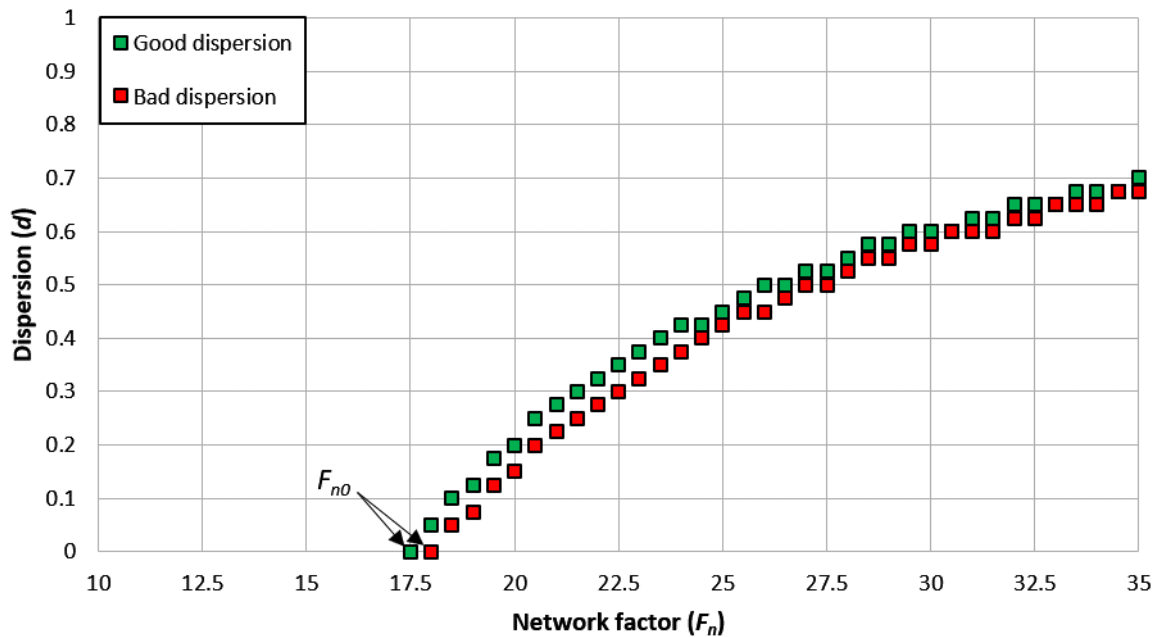


Figure 65. Measured (squares) and modelled (lines) permittivity of PLA/MWNT composites, with good and bad dispersion, for different volume fractions. Error bars are the standard deviation of 4 samples and are visible when the error is larger than the marker size.

### 5.3.3.2 PLA/CB Composites

The reference network factor ( $F_{n0}$ ) for the PLA/CB composites was calculated by fitting the experimental data from Figure 63 to the e-PvSB model. In Figure 66, the set of combinations of dispersion and network factor that reproduces the experimental data, for both good and bad dispersion, is represented (the corresponding matrices of coefficients of determination are shown in Appendix B). As discussed in section 4.5, it is not possible to discern which of all the possible solutions most accurately describe the real morphology of the composites. Instead, the  $F_{n0}$  is calculated. Due to the sphericity of individual CB particles, their orientation is

meaningless, and the alignment parameter has no influence on the permittivity of the composites.



**Figure 66.** Different possible combinations of dispersion (vertical axis) and network factor (horizontal axis) that describe the measured permittivity of the PLA/CB composites of Figure 63.

The observed values of  $F_{n0}$  were  $17.4 \pm 0.1$  and  $18.0 \pm 0.1$ , for the composites with good and bad dispersion, respectively. As expected, the  $F_{n0}$  of the composite with bad dispersion is larger than the  $F_{n0}$  of the composite good dispersion.

In Figure 67, the experimental data and the corresponding values provided by the e-PvSB model are represented. The coefficients of correlation are 0.99 and 1.00 for the composite with good and bad dispersion, respectively.

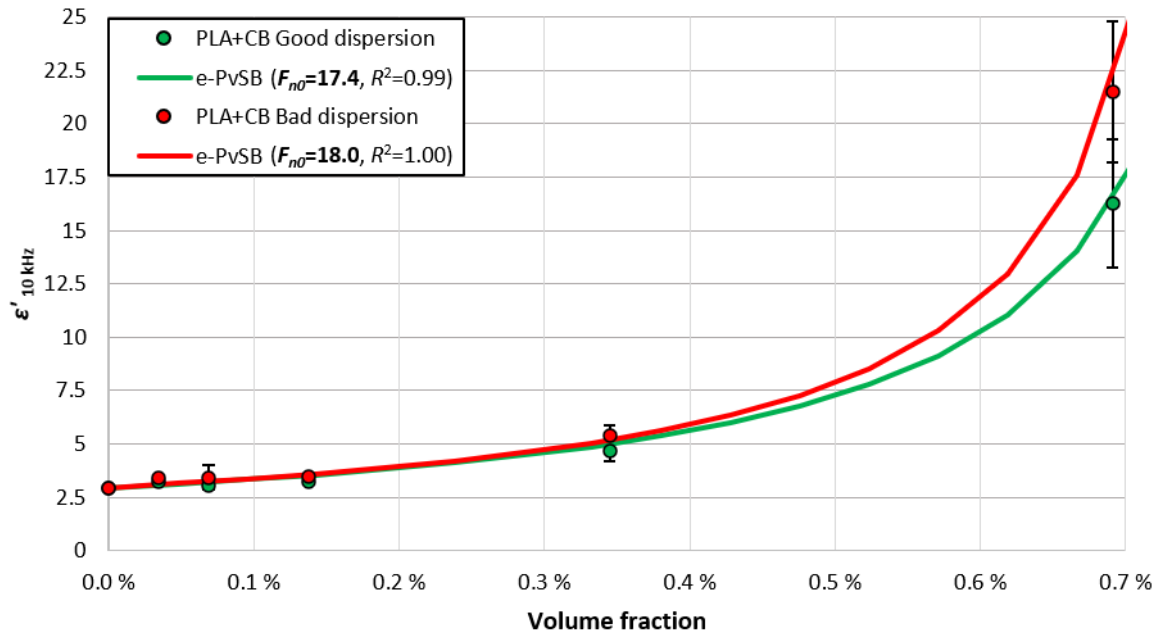


Figure 67. Measured (circles) and modelled (lines) permittivity of PLA/CB composites, with good and bad dispersion, for different volume concentrations. Error bars are the standard deviation of 4 samples and are visible when the error is larger than the marker size.

#### 5.4 Discussion

The dielectric properties of composites of PLA with MWNT or CB with good or bad dispersion at different concentrations were measured. Results agree with previous observations: Pötschke et al. [112] have reported a decrease in electrical conductivity and permittivity of MWNT/polymer composites with increasing dispersion. Alig et al. [113] use percolation theory to quantitatively describe this effect. However, percolation theories lack of any direct relation between dielectric properties and morphological characteristics of the composites like filler aspect ratio, dispersion or alignment. The quantitative description proposed in this thesis takes into account all of these factors.

The method described in section 4.5 to obtain morphological information of a composite using the e-PVSB model was successfully applied to experimental data. The observed values of reference network factor ( $F_{n0}$ ) qualitatively agree with the results of optical transmission microscopy and scanning electron microscopy: composites with bad dispersion show a greater value of  $F_{n0}$  than composites with good dispersion, as expected.

The reference network factor ( $F_{n0}$ ) can therefore be used as a parameter to compare similar composites with different expected degrees of dispersion.

In a fabrication process where no filler alignment is expected or detected by other techniques, the reference network factor can be used as a parameter representing the quality of the filler dispersion in the composite. The reference network factor could be used, e.g., to compare the quality of the dispersion obtained with different combinations of process parameters during extrusion.

## 6. Analysis of Alignment

In this chapter, the e-PvSB model will be applied to obtain morphological information from composites with different degrees of alignment and network factor.

### 6.1 Nanocomposites

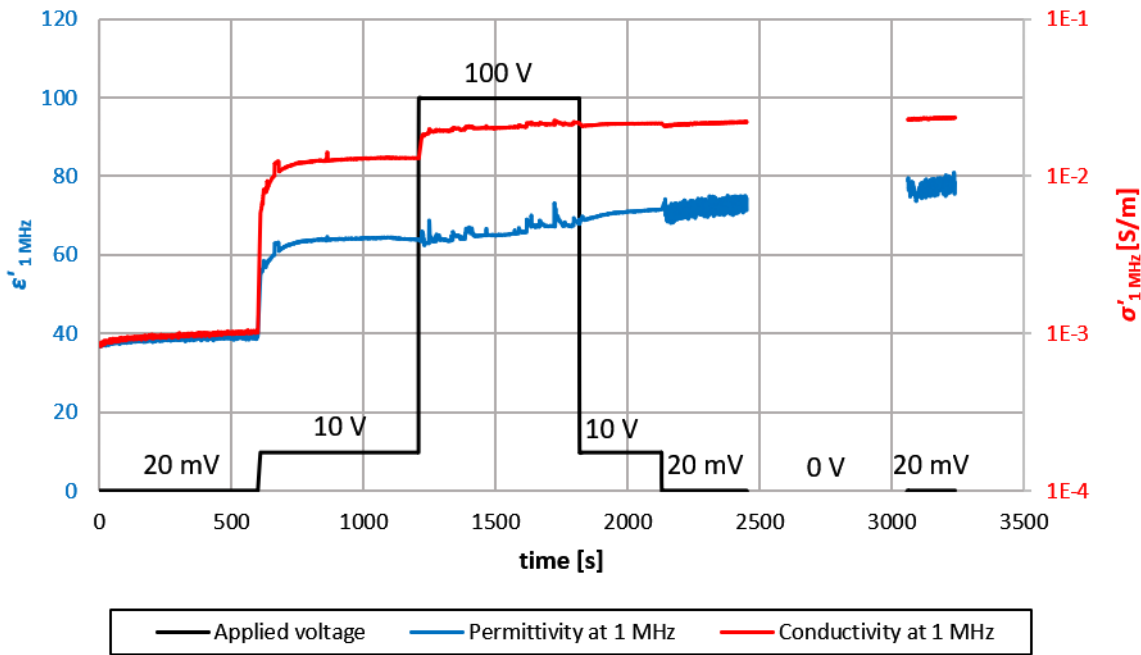
Epoxy/SWNT composites were produced with an electric field treatment (see section 3.2.4) that is expected to induce alignment and the formation of networks of SWNT. The e-PvSB model is applied in this chapter to detect those features.

### 6.2 In-situ Characterization

The dielectric properties of epoxy/SWNT composites were measured before and during curing with the setup described in chapter 3.

#### 6.2.1 Monitorization of the Electric Treatment

A dispersion of SWNT in epoxy resin (without curing agent) was characterized under electric fields of different magnitudes to observe the change in electric properties due to the reorientation and/or migration of SWNTs. In Figure 68, the change over time in permittivity and conductivity in response to electric fields of different magnitudes (0 V, 20 mV, 10 V, 100 V over a distance of 2 mm) is shown. The voltage was applied at 1 MHz (it has been reported that the electric field treatment is more efficient at higher frequencies [63]) and was used to induce alignment and measure the electric properties at the same time (for this reason, no measured values of conductivity and permittivity are available when the voltage is 0). The magnitude of the electric field was changed in steps of approximately 5 minutes in a continuous measurement.



**Figure 68.** Time evolution of permittivity and conductivity at 1 MHz of an epoxy resin with a SWNT mass concentration of 0.005 %. Different voltages were applied over a distance of 2 mm.

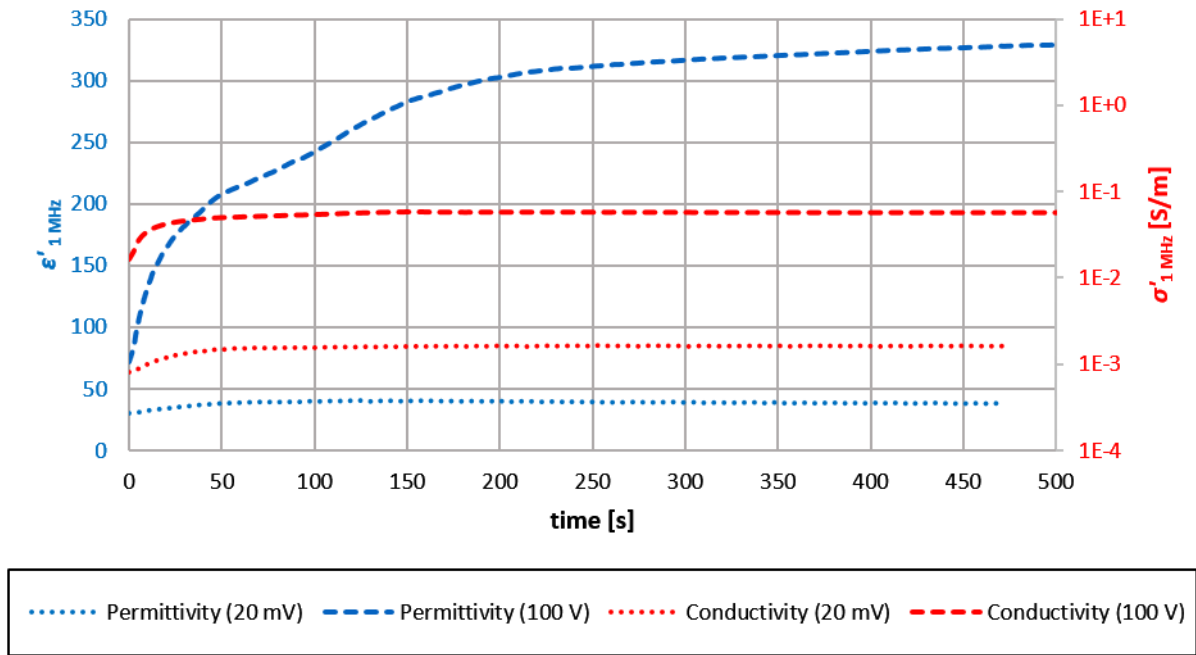
It can be observed how the lowest voltage (20 mV) induces only a slight increase in permittivity and conductivity, while the higher voltages (10 V and 100 V) make them almost double and increase one order of magnitude, respectively. The DC conductivity may have increased more than the measured conductivity at 1 MHz (see conductivity spectra in Appendix C). For values of permittivity over 70, the measurements become noisy when measured with low voltages (20 mV).

Each time the voltage is increased, the conductivity increases to what seems to be an equilibrium value. Once this value is achieved, the conductivity does not decrease after reducing or even removing the electric field. This might be due to the formation of percolating networks of SWNTs, which are relatively stable [67], [113], [114].

### 6.2.2 Monitorization of the curing process

The curing of the epoxy composites was monitorized by dielectric measurements. An electric field was applied in order to perform the measurements and induce alignment, at the same time. In Figure 69, the change over time in permittivity and conductivity at 1 MHz during the curing of an epoxy composite with a SWNT mass concentration of 0.005 % is shown.





**Figure 69.** Time evolution of permittivity and conductivity at 1 MHz during the curing of epoxy composites with a SWNT mass concentration of 0.005 % under 100 V (electric field treatment) and 20 mV.

In view of the results in Figure 68 (with 20 mV changes in permittivity and conductivity are negligible), the voltage of the dielectric measurement was set to 100 V or 20 mV, to induce or avoid alignment of the SWNT, respectively. The time scale at which the alignment takes places (tens of seconds, see Figure 68), is much lower than the time scale of the curing (hundreds of seconds). Therefore, the alignment process is expected to happen to a sufficient extent before the epoxy becomes too viscous due to the curing.

It must be noted that the value of conductivity is measured at 1 MHz and is not proportional to the DC conductivity, making it less significant (see Appendix C, where the conductivity spectra of epoxy/SWNT composites are shown; samples with different DC conductivity have similar values of conductivity at 1 MHz).

When curing epoxy without SWNTs, a decrease in permittivity is observed (Figure 70), due to the decrease of viscosity, and hence, the decrease of mobility of polar groups.

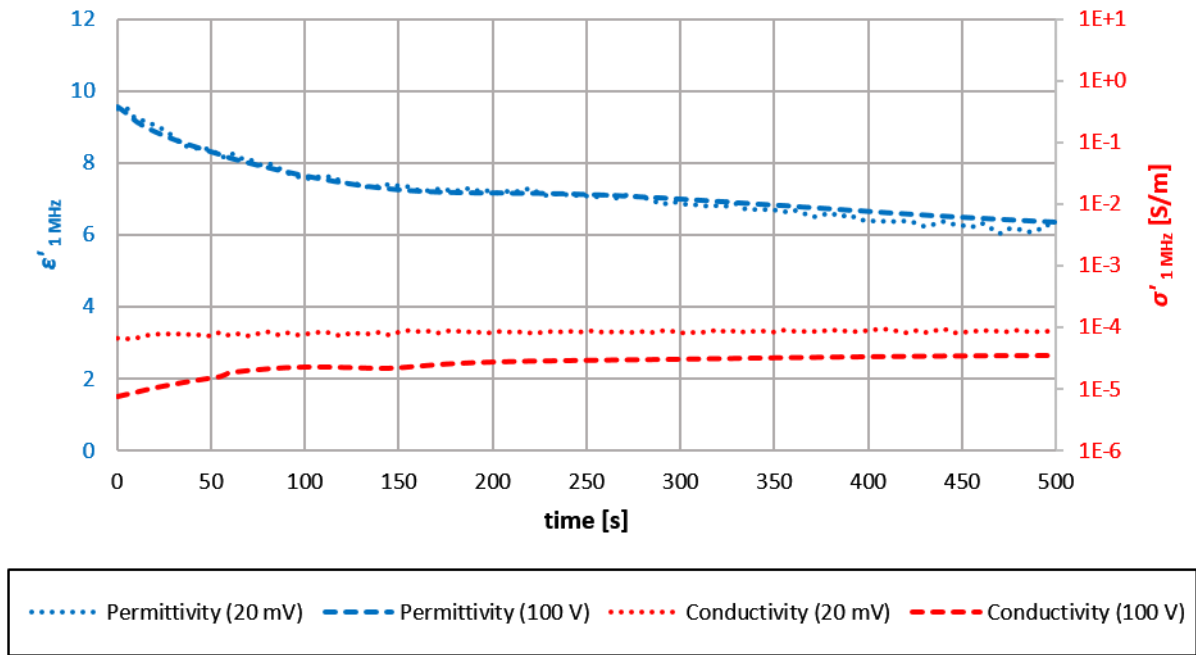
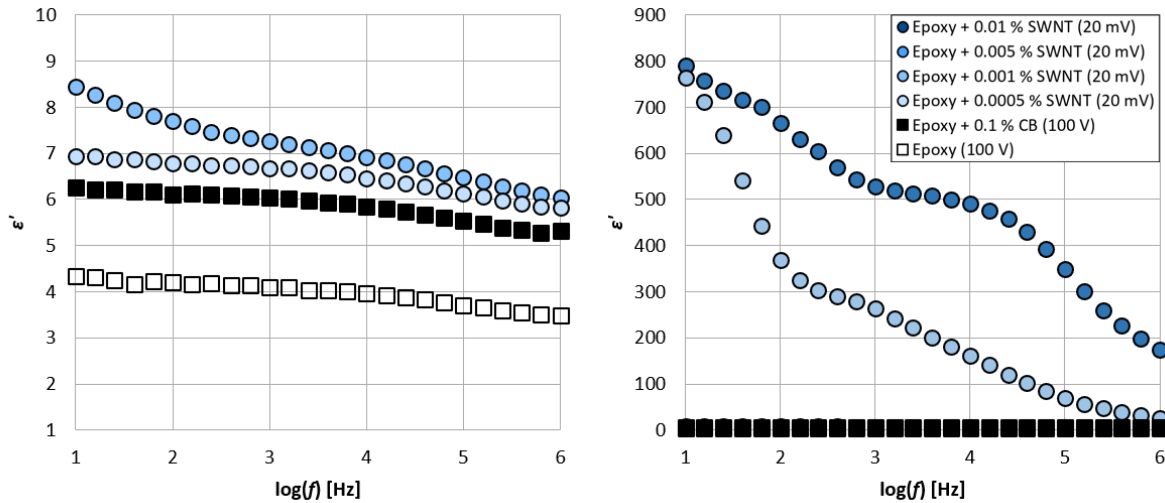


Figure 70. Time evolution of permittivity and conductivity at 1 MHz during the curing of epoxy without SWNTs.

### 6.3 Ex-situ characterization

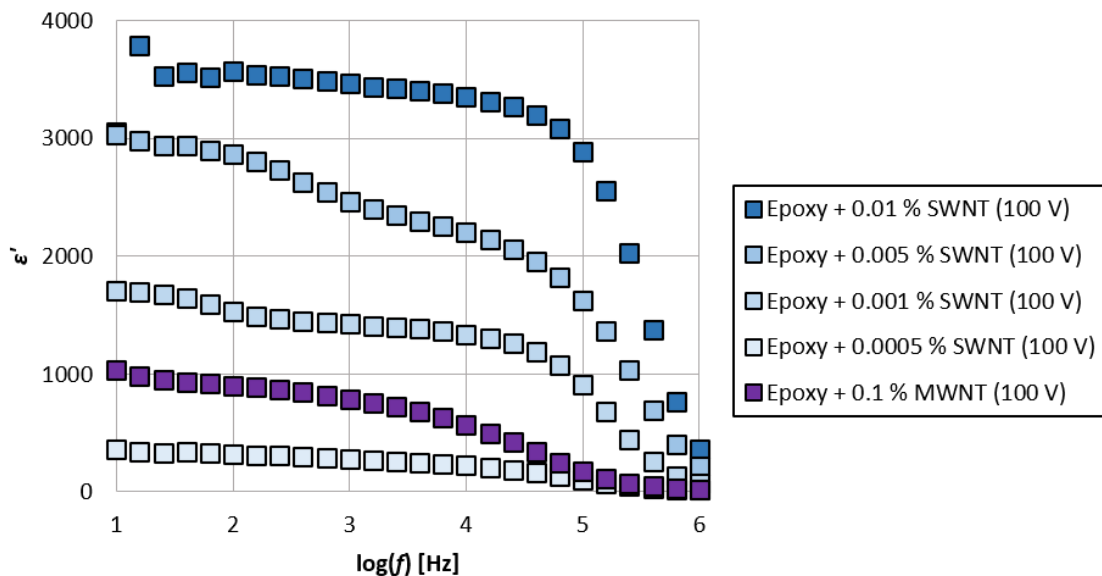
In this section, the results of dielectric spectroscopy are presented and discussed. The dielectric spectra were measured as described in section 3.3.1.1, between 1 Hz and 1 MHz

In Figure 71 and Figure 72, the dielectric spectra of composites cured without and with electric field treatment (which will be called aligned and non-aligned composites for the sake of simplicity, although it may not represent the real morphology of the composites), respectively, are shown. A reference sample of unfilled epoxy (black, Figure 71), as well as aligned samples with multi-walled carbon nanotubes (blue, Figure 72) and carbon black (purple, Figure 71) are shown for comparison.



**Figure 71.** Dielectric spectra of non-aligned composites for SWNT mass concentrations between 0.0005 % and 0.01 %. The spectra of unfilled epoxy (white) and an aligned epoxy/CB composite are also included. Data are split in two plots to visualize the different magnitudes of  $\epsilon'$  (a logarithm scale would hide important features).

It must be noted how the dielectric spectra of the non-aligned composites are mostly flat, especially for low concentrations. Only the composites at higher concentrations features dielectric steps, similar to the aligned composites of Figure 72. At frequencies lower than 10 Hz the measurement was noisy for the samples with higher permittivity, which might be an effect of electrode polarization, characteristic of conductive samples (see section 2.1.5.4).



**Figure 72.** Dielectric spectra of aligned composites for SWNT mass concentrations between 0.0005 % and 0.01 %. The spectrum of a composite of epoxy/MWNT (purple) after electrical treatment is also included.

The aligned 0.1 % MWNT composite in Figure 72 shows a much smaller increase in permittivity with respect to the unfilled epoxy than the aligned composites with up to 0.01 % SWNT. This suggests that the SWNT are much more influenced by the electric field treatment than the MWNT [115].

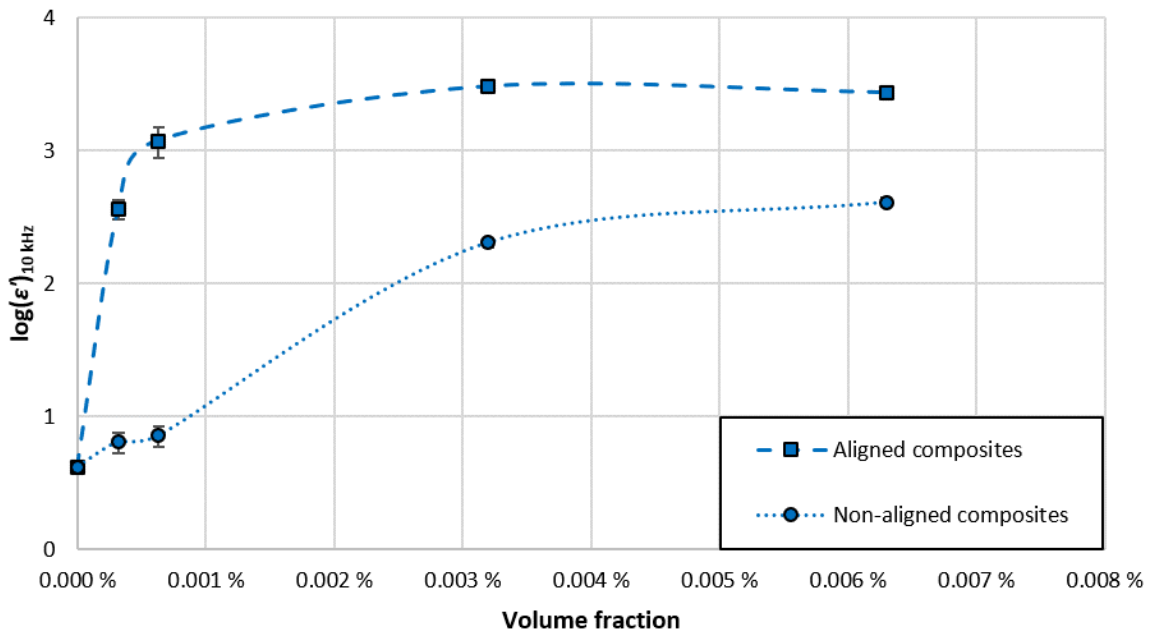
The aligned 0.1 % CB composite shows an even smaller increase in permittivity with respect to the unfilled epoxy (Figure 71). This suggests that the low aspect ratio of CB (around 1) greatly hinders the effect of the electric field treatment in forming networks.

The dielectric spectra of the aligned composites feature two dielectric steps (one around 100 Hz-1 kHz and one around 100 kHz-1 MHz), which represent two Maxwell/Wagner polarization processes (see section 2.1.5.3). Two dielectric steps imply the presence of two different interphases, i.e., two fillers with different conductivity. SWNTs are typically produced as a mix of semiconductive and metallic SWNTs [116], [117].

The mechanism of both Maxwell/Wagner dielectric steps is therefore hypothesized as coming from a metallic SWNT/epoxy interphase (for the step at high frequencies) and a semiconductive SWNT/epoxy interphase. The presence of a single dielectric step in the spectrum of the composite with MWNTs supports this hypothesis, but its demonstration goes beyond the scope of this thesis. A quantification of the ratio metallic SWNT / semiconductive SWNT from the dielectric spectra would be challenging, due to the number of factors influencing the size of the dielectric step, including possible different degrees of alignment of metallic and semiconductive SWNTs.

#### **6.4 Analysis with e-PvSB Model**

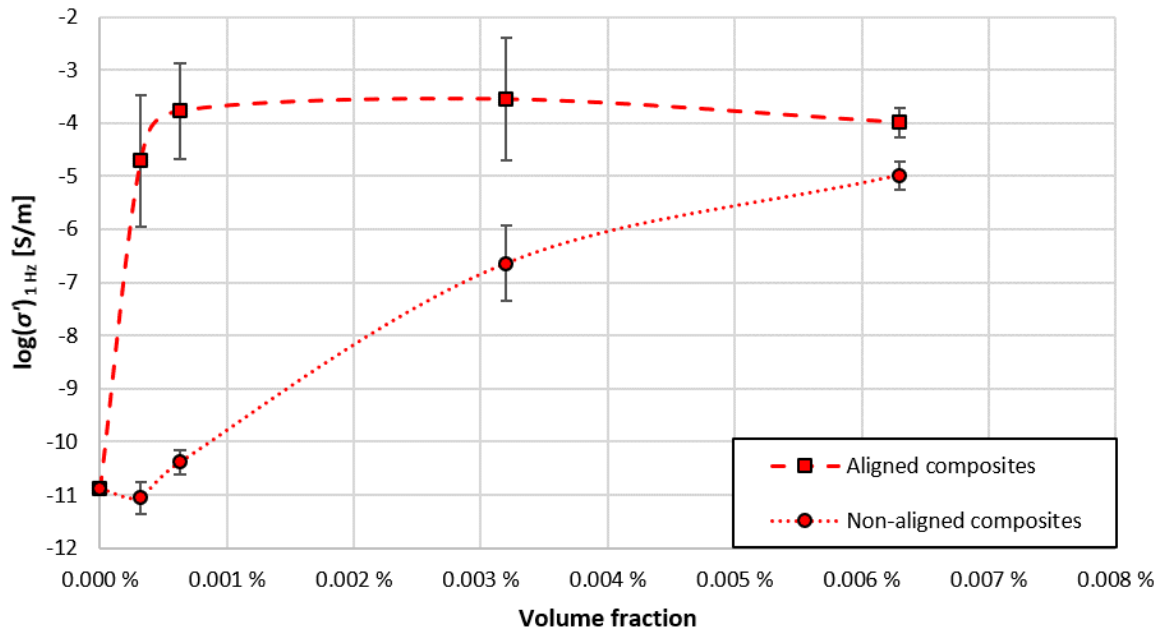
In Figure 73, the permittivity of the cured composites is shown as a function of concentration. The values of permittivity were considered at an arbitrary frequency (10 kHz) for convenience. Choosing other frequencies higher than 100 Hz (at 10 Hz or lower frequencies the measurement was noisy for the samples with higher permittivity) does not alter the conclusions of this chapter.



**Figure 73.** Permittivity at 10 kHz for aligned (squares) and non-aligned (circles) epoxy/SWNT composites. Error bars are the standard deviation of 4 samples and are visible when the error is larger than the marker size. Lines are a visual guidance.

A huge increase in permittivity is observed for the aligned composites with respect to the non-aligned composites.

In Figure 74 the conductivity of the cured composites is shown as a function of concentration. The values of conductivity were considered at the lowest available frequency (1 Hz), for which the conductivity corresponds to the DC conductivity (except for the samples with conductivity lower than  $10^{-10}$  S/m at 1 Hz (see the conductivity spectra in Appendix C for more details)).



**Figure 74. Conductivity at 1 Hz for aligned (squares) and non-aligned (circles) epoxy/SWNT composites. Error bars are the standard deviation of 4 samples and are visible when the error is larger than the marker size. Lines are a visual guidance.**

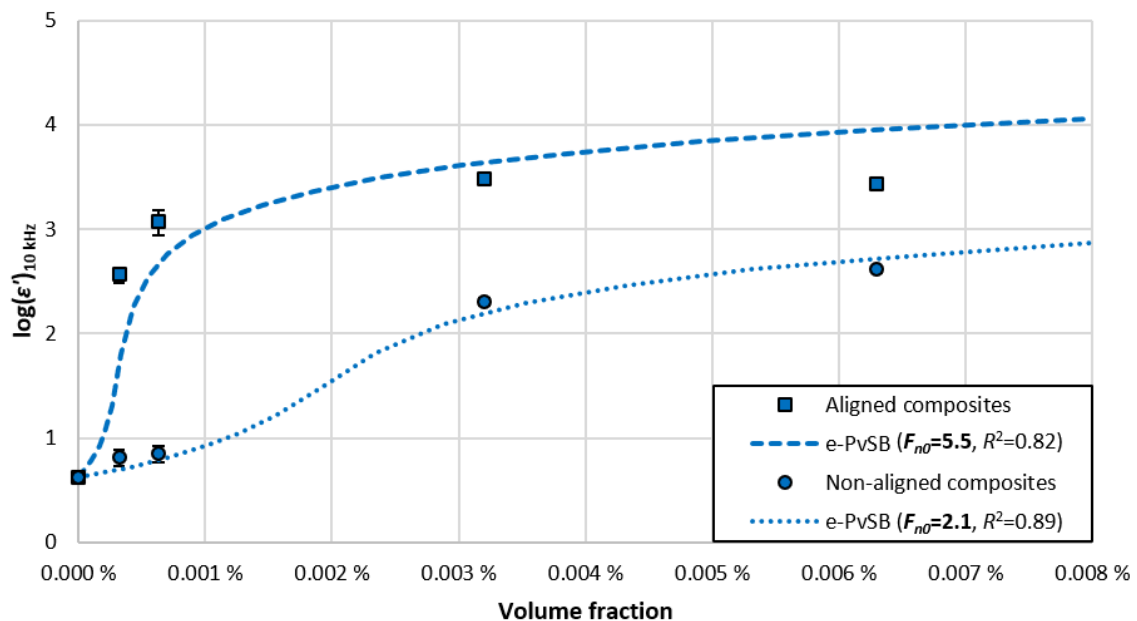
It must be noted the huge effect of the electric field treatment on conductivity, making the conductivity apparently independent of concentration. This suggest that during the electric field treatment, SWNTs make new contacts and create thus percolating networks (this effect has been reported before [63], [64]). Composites without the electric field treatment do not create this percolating network until the concentration exceed the percolation threshold, which in this case happens at volume concentrations between 0.001 % and 0.005 %.

The electric field treatment can therefore be considered as a method to induce percolation in composites at low concentrations.

It must be noted that, unlike in previous chapters, some values of permittivity are measured above the percolation threshold. However, when applied above the percolation threshold, the e-PvSB model cannot be simplified (as in section 4.1.2) and hence the permittivity of the composites must be solved numerically. The matrix of possible solutions is therefore computationally expensive to calculate and is not provided in this thesis. The value of reference network factor ( $F_{n0}$ ) can be however calculated by a single nonlinear regression.

The values of ( $F_{n0}$ ) were found (by non-linear regression) to be 5.5 and 2.1 (Figure 75) with coefficients of regression of 0.82 and 0.89, for the aligned and non-aligned composites,

respectively. The coefficients of regression indicate a rather inaccurate fitting to the experimental data. The inaccuracy stems, on one hand, from the higher deviations in the observed values. But on the other hand, the process of alignment and formation of new networks is chaotic and cannot be assumed to provide the same values of  $F_{n0}$  for every concentration of SWNT.



**Figure 75.** Measured (squares and circles) and modelled (lines) permittivity of aligned and non-aligned composites for different volume concentrations.

The value of  $F_{n0}$  increases highly with the electric treatment: it increases more than a 150 %, when it increases only around a 20 % for the PLA/MWNT composites of chapter 5. This high increase suggests that the SWNT are forming new networks along the direction of the electric field treatment. The e-PvSB model therefore describes the expected behaviour.

The morphology suggested by this analysis is compatible with the hypothesis of alignment and network formation due to the electric field treatment.

## 6.5 Discussion

The e-PvSB was used to compare composites with different degrees of alignment and network formation.

The dielectric properties of composites of epoxy with SWNTs were measured at different concentrations. The samples were prepared with and without an electric treatment that is thought to induce some degree of alignment and/or form new contacts between SWNTs. The inducement of alignment by an electric field is theoretically based on the dielectrophoretic effects experimented by carbon nanotubes [63] and other particles [118] in an electric field, and experimentally supported in [64], [71], [119], [120].

For this purpose, a setup was developed that allowed the dielectric monitorization of the curing process of the composite.

The dielectric spectra of the composites feature two relaxation processes that might originate from the presence of a mixture of metallic and semiconductive SWNTs. However, quantifying the ratio of this mixture is challenging and goes beyond the scope of this thesis.

The method described in section 4.5 to obtain morphological information of a composite using the e-PVSB model was successfully applied to the experimental data. The observed values of reference network factor ( $F_{n0}$ ) support the idea of the electric treatment inducing SWNTs to form new connections and/or aligning along the electric field. Moreover, networks are expected to be more aligned and/or larger in the direction of the electric field.

The reference network factor ( $F_{n0}$ ) can therefore be used as a parameter to compare similar composites with different expected degrees of alignment. It could therefore be used as a parameter representing the degree of filler alignment.



## 7. Conclusions

An effective medium model (PvSB) has been considered to predict the dielectric properties of composites of conductive fillers in a non-conductive matrix as a function of their filler dispersion and orientation. Two parameters, alignment and dispersion, were defined in terms of the components of the model. The model was experimentally validated using reference samples with controlled conditions of dispersion and orientation.

An extension to the PvSB model (e-PvSB) has been proposed to account for the contact or networking formation of the fillers in a composite. A methodology is proposed to use the e-PvSB model to obtain morphological information from experimental data. A parameter, the reference network factor, was introduced to account for the effects of the network formation and orientation.

Percolation theories have been widely used to describe the electrical properties of nanocomposites. However, percolation theories lack of any direct relation between dielectric properties and morphological characteristics of the composites like filler aspect ratio, dispersion or alignment. The quantitative description proposed in this thesis takes into account all of these factors.

The method was applied to experimental data of polymer composites with carbon nanotubes and carbon black. The values of the reference network factor predicted by the e-PvSB model qualitatively agree with the results of microscopic techniques and the expected morphology of the composites.

Due to the volumetric nature of the dielectric measurements, this method provides a general or averaging picture of the morphology of a composite. That is, the method considers effective properties that describe the behaviour of the sample as a whole and provides no direct information of local effects.

Due to the simple sample preparation and the short measurement times of dielectric measurements, relative to existing characterization techniques, this method constitutes a tool for a fast estimation of the morphological properties of composites.

The characterization method proposed in this thesis can be used to complement other characterization techniques, like scanning electron microscopy, that can provide detailed information about the morphology of a composite, but typically in a small region of a

macroscopic sample. Once the morphology of a composite, produced with a given fabrication process, is analysed with the assistance of other characterization techniques, the value of the reference network factor can be used as a quality control parameter for mass production. Potentially, the method could be used in in-line measurements during the fabrication of a composite, so that the reference network factor could be used in a Shewhart chart or control chart as a quality control tool.

The reference network factor can therefore be used as a parameter to compare similar composites with different expected degrees of dispersion or alignment.

In a fabrication process where no filler alignment is expected or detected by other techniques, the reference network factor can be used as a parameter representing the quality of the filler dispersion in the composite. The reference network factor could be used, e.g., to compare the quality of the dispersion obtained with different combinations of process parameters during extrusion.

When a process is expected to induce filler alignment, the reference network factor can be used as a parameter representing the degree of filler alignment. The reference network factor could be used, e.g., to compare the degree of filler alignment induced by flow effects in injection moulding or the filler alignment induced by an electrical field, as described in Chapter 6.

## References

- [1] B. Bhushan, Ed., *Encyclopedia of Nanotechnology*. Dordrecht: Springer Netherlands, 2012, DOI: <https://doi.org/10.1007/978-90-481-9751-4>.
- [2] S. A. Curran, P. M. Ajayan, W. J. Blau, D. L. Carroll, J. N. Coleman, A. B. Dalton, A. P. Davey, A. Drury, B. McCarthy, S. Maier, *et al.*, “A Composite from Poly(m-phenylenevinylene-co-2,5-dioctoxy-p-phenylenevinylene) and Carbon Nanotubes: A Novel Material for Molecular Optoelectronics,” *Adv. Mater.*, vol. 10, no. 14, pp. 1091–1093, Oct. 1998, DOI: [https://doi.org/10.1002/\(SICI\)1521-4095\(199810\)10:14<1091::AID-ADMA1091>3.0.CO;2-L](https://doi.org/10.1002/(SICI)1521-4095(199810)10:14<1091::AID-ADMA1091>3.0.CO;2-L).
- [3] M. S. P. Shaffer and A. H. Windle, “Fabrication and Characterization of Carbon Nanotube/Poly(vinyl alcohol) Composites,” *Adv. Mater.*, vol. 11, no. 11, pp. 937–941, Aug. 1999, DOI: [https://doi.org/10.1002/\(SICI\)1521-4095\(199908\)11:11<937::AID-ADMA937>3.0.CO;2-9](https://doi.org/10.1002/(SICI)1521-4095(199908)11:11<937::AID-ADMA937>3.0.CO;2-9).
- [4] B. Vigolo, P. Poulin, M. Lucas, P. Launois, and P. Bernier, “Improved structure and properties of single-wall carbon nanotube spun fibers,” *Appl. Phys. Lett.*, vol. 81, no. 7, pp. 1210–1212, Aug. 2002, DOI: <https://doi.org/10.1063/1.1497706>.
- [5] M. Cadek, B. Le Foulgoc, J. N. Coleman, V. Barron, J. Sandler, M. S. P. Shaffer, A. Fonseca, M. van Es, K. Schulte, and W. J. Blau, “Mechanical and Thermal Properties of CNT and CNF Reinforced Polymer Composites,” in *AIP Conference Proceedings*, Oct. 2002, vol. 633, no. 1, pp. 562–565, DOI: <https://doi.org/10.1063/1.1514183>.
- [6] P. Pötschke, A. R. Bhattacharyya, and A. Janke, “Carbon nanotube-filled polycarbonate composites produced by melt mixing and their use in blends with polyethylene,” *Carbon N. Y.*, vol. 42, no. 5–6, pp. 965–969, Jan. 2004, DOI: <https://doi.org/10.1016/j.carbon.2003.12.001>.
- [7] F. Nanni and M. Valentini, “11 – Electromagnetic properties of polymer–carbon nanotube composites,” in *Polymer–Carbon Nanotube Composites*, Cambridge: Elsevier (Woodhead Publishing United Kingdom), 2011, pp. 329–346, DOI: <https://doi.org/10.1533/9780857091390.2.329>.
- [8] S. C. Tjong, G. D. Liang, and S. P. Bao, “Electrical behavior of polypropylene/multiwalled carbon nanotube nanocomposites with low percolation threshold,” *Scr. Mater.*, vol. 57, no. 6, pp. 461–464, Sep. 2007, DOI: <https://doi.org/10.1016/j.scriptamat.2007.05.035>.
- [9] S. Paszkiewicz, A. Szymczyk, X. M. Sui, H. D. Wagner, A. Linares, T. A. Ezquerra, and Z. Rosłaniec, “Synergetic effect of single-walled carbon nanotubes (SWCNT) and

- graphene nanoplatelets (GNP) in electrically conductive PTT-block-PTMO hybrid nanocomposites prepared by in situ polymerization,” *Compos. Sci. Technol.*, vol. 118, pp. 72–77, Oct. 2015, DOI: <https://doi.org/10.1016/j.compscitech.2015.08.011>.
- [10] K. Tsuchiya, A. Sakai, T. Nagaoka, K. Uchida, T. Furukawa, and H. Yajima, “High electrical performance of carbon nanotubes/rubber composites with low percolation threshold prepared with a rotation–revolution mixing technique,” *Compos. Sci. Technol.*, vol. 71, no. 8, pp. 1098–1104, May 2011, DOI: <https://doi.org/10.1016/j.compscitech.2011.03.015>.
- [11] M. Cadek, J. N. Coleman, V. Barron, K. Hedicke, and W. J. Blau, “Morphological and mechanical properties of carbon-nanotube-reinforced semicrystalline and amorphous polymer composites,” *Appl. Phys. Lett.*, vol. 81, no. 27, p. 5123, Dec. 2002, DOI: <https://doi.org/10.1063/1.1533118>.
- [12] C. Schilde, M. Schlömann, A. Overbeck, S. Linke, and A. Kwade, “Thermal, mechanical and electrical properties of highly loaded CNT-epoxy composites – A model for the electric conductivity,” *Compos. Sci. Technol.*, vol. 117, pp. 183–190, Sep. 2015, DOI: <https://doi.org/10.1016/j.compscitech.2015.06.013>.
- [13] M. Monti, I. Armentano, G. Faiella, V. Antonucci, J. M. Kenny, L. Torre, and M. Giordano, “Toward the microstructure–properties relationship in MWCNT/epoxy composites: Percolation behavior and dielectric spectroscopy,” *Compos. Sci. Technol.*, vol. 96, pp. 38–46, May 2014, DOI: <https://doi.org/10.1016/j.compscitech.2014.03.008>.
- [14] P. Pötschke, A. R. Bhattacharyya, and A. Janke, “Morphology and electrical resistivity of melt mixed blends of polyethylene and carbon nanotube filled polycarbonate,” *Polymer (Guildf.)*, vol. 44, no. 26, pp. 8061–8069, Dec. 2003, DOI: <https://doi.org/10.1016/j.polymer.2003.10.003>.
- [15] K. Trommer and C. Petzold, “Visualization of CNT-distribution in a polymer matrix by atomic force microscopy,” in *Annual Conference NanoCarbon (Network NanoCarbon, Würzburg)*, Poster [Not published], 2016.
- [16] B. McCarthy, J. N. Coleman, R. Czerw, A. B. Dalton, M. in het Panhuis, A. Maiti, A. Drury, P. Bernier, J. B. Nagy, B. Lahr, *et al.*, “A Microscopic and Spectroscopic Study of Interactions between Carbon Nanotubes and a Conjugated Polymer,” *J. Phys. Chem. B*, vol. 106, no. 9, pp. 2210–2216, Mar. 2002, DOI: <https://doi.org/10.1021/jp013745f>.
- [17] J. P. Runt and J. Fitzgerald, *Dielectric spectroscopy of polymeric materials: Fundamentals and Applications*. American Chemical Society, Professional Reference Book, 1999, ISBN: 9780841233355.
- [18] A. A. Volkov and A. S. Prokhorov, “Broadband Dielectric Spectroscopy of Solids,”

- Radiophys. Quantum Electron.*, vol. 46, no. 8/9, pp. 657–665, Aug. 2003, DOI: <https://doi.org/10.1023/B:RAQE.0000024994.15881.c9>.
- [19] A. Schönhals and F. Kremer, “Broadband Dielectric Measurement Techniques (10-6 Hz to 1012 Hz),” in *Broadband Dielectric Spectroscopy*, Berlin, Heidelberg: Springer Berlin Heidelberg, 2003, pp. 35–57, DOI: [https://doi.org/10.1007/978-3-642-56120-7\\_2](https://doi.org/10.1007/978-3-642-56120-7_2).
- [20] K. A. Mauritz, “Dielectric Spectroscopy (An illustration of the frequency response of various dielectric mechanisms in terms of the real and imaginary parts of the permittivity.),” 2008, Accessed: Apr. 03, 2019. [Online]. Available: [https://commons.wikimedia.org/wiki/File:Dielectric\\_responses.svg](https://commons.wikimedia.org/wiki/File:Dielectric_responses.svg).
- [21] E. Barsoukov and J. R. Macdonald, *Impedance Spectroscopy*. Hoboken, NJ, USA: John Wiley & Sons, Inc., 2005, DOI: <https://doi.org/10.1002/0471716243>.
- [22] A. Schönhals and F. Kremer, “Theory of Dielectric Relaxation,” in *Broadband Dielectric Spectroscopy*, Berlin, Heidelberg: Springer Berlin Heidelberg, 2003, pp. 1–33, DOI: [https://doi.org/10.1007/978-3-642-56120-7\\_1](https://doi.org/10.1007/978-3-642-56120-7_1).
- [23] A. Schönhals and F. Kremer, “Analysis of Dielectric Spectra,” in *Broadband Dielectric Spectroscopy*, Berlin, Heidelberg: Springer Berlin Heidelberg, 2003, pp. 59–98, DOI: [https://doi.org/10.1007/978-3-642-56120-7\\_3](https://doi.org/10.1007/978-3-642-56120-7_3).
- [24] P. A. M. Steeman and J. van Turnhout, “Dielectric Properties of Inhomogeneous Media,” in *Broadband Dielectric Spectroscopy*, Berlin, Heidelberg: Springer Berlin Heidelberg, 2003, pp. 495–522, DOI: [https://doi.org/10.1007/978-3-642-56120-7\\_13](https://doi.org/10.1007/978-3-642-56120-7_13).
- [25] C. J. F. Böttcher, O. C. van. Belle, P. Bordewijk, and A. Rip, *Theory of electric polarization*. Amsterdam: Elsevier Scientific Pub. Co, 1973, ISBN: 0444415793.
- [26] P. Debye, *Polar molecules*. [New York]: Dover, Book, 1929, Accessed: Apr. 03, 2019. [Online]. Available: <https://www.worldcat.org/title/polar-molecules/oclc/6771812>.
- [27] H. Fröhlich, “Theory of dielectrics.” Clarendon Press, Book, 1949, Accessed: Apr. 03, 2019. [Online]. Available: <http://cds.cern.ch/record/107973>.
- [28] K. S. Cole and R. H. Cole, “Dispersion and Absorption in Dielectrics I. Alternating Current Characteristics,” *J. Chem. Phys.*, vol. 9, no. 4, pp. 341–351, Apr. 1941, DOI: <https://doi.org/10.1063/1.1750906>.
- [29] D. W. Davidson and R. H. Cole, “Dielectric Relaxation in Glycerine,” *J. Chem. Phys.*, vol. 18, no. 10, pp. 1417–1417, Oct. 1950, DOI: <https://doi.org/10.1063/1.1747496>.
- [30] D. W. Davidson and R. H. Cole, “Dielectric Relaxation in Glycerol, Propylene Glycol, and *n*-Propanol,” *J. Chem. Phys.*, vol. 19, no. 12, pp. 1484–1490, Dec. 1951, DOI:

- <https://doi.org/10.1063/1.1748105>.
- [31] R. M. Fuoss and J. G. Kirkwood, "Electrical Properties of Solids. VIII. Dipole Moments in Polyvinyl Chloride-Diphenyl Systems," *J. Am. Chem. Soc.*, vol. 63, no. 2, pp. 385–394, Feb. 1941, DOI: <https://doi.org/10.1021/ja01847a013>.
- [32] S. Havriliak and S. Negami, "A complex plane analysis of  $\alpha$ -dispersions in some polymer systems," *J. Polym. Sci. Part C Polym. Symp.*, vol. 14, no. 1, pp. 99–117, Mar. 1966, DOI: <https://doi.org/10.1002/polc.5070140111>.
- [33] S. Havriliak and S. Negami, "A complex plane representation of dielectric and mechanical relaxation processes in some polymers," *Polymer (Guildf.)*, vol. 8, pp. 161–210, Jan. 1967, DOI: [https://doi.org/10.1016/0032-3861\(67\)90021-3](https://doi.org/10.1016/0032-3861(67)90021-3).
- [34] P. Pissis, D. Fragiadakis, A. Kanapitsas, and K. Delides, "Broadband dielectric relaxation spectroscopy in polymer nanocomposites," *Macromol. Symp.*, vol. 265, pp. 12–20, 2008, DOI: <https://doi.org/10.1002/masy.200850502>.
- [35] P. Klonos, A. Kyritsis, L. Bokobza, V. M. Gun'ko, and P. Pissis, "Interfacial effects in PDMS/titania nanocomposites studied by thermal and dielectric techniques," *Colloids Surfaces A Physicochem. Eng. Asp.*, vol. 519, pp. 212–222, Apr. 2017, DOI: <https://doi.org/10.1016/j.colsurfa.2016.04.020>.
- [36] P. Klonos, Z. Terzopoulou, S. Koutsoumpis, S. Zidropoulos, S. Kriptou, G. Z. Papageorgiou, D. N. Bikiaris, A. Kyritsis, and P. Pissis, "Rigid amorphous fraction and segmental dynamics in nanocomposites based on poly(l-lactic acid) and nano-inclusions of 1–3D geometry studied by thermal and dielectric techniques," *Eur. Polym. J.*, vol. 82, pp. 16–34, Sep. 2016, DOI: <https://doi.org/10.1016/j.eurpolymj.2016.07.002>.
- [37] P. Klonos, S. Kriptou, A. Kyritsis, G. Z. Papageorgiou, D. Bikiaris, D. Gournis, and P. Pissis, "Glass transition and segmental dynamics in poly(l-lactic acid)/graphene oxide nanocomposites," *Thermochim. Acta*, vol. 617, pp. 44–53, Oct. 2015, DOI: <https://doi.org/10.1016/j.tca.2015.08.020>.
- [38] P. J. Purohit, D.-Y. Wang, A. Wurm, C. Schick, and A. Schönhals, "Comparison of thermal and dielectric spectroscopy for nanocomposites based on polypropylene and Layered Double Hydroxide – Proof of interfaces," *Eur. Polym. J.*, vol. 55, pp. 48–56, Jun. 2014, DOI: <https://doi.org/10.1016/j.eurpolymj.2014.03.005>.
- [39] F. Kremer and A. Schönhals, Eds., *Broadband Dielectric Spectroscopy*. Berlin, Heidelberg: Springer Berlin Heidelberg, 2003, DOI: <https://doi.org/10.1007/978-3-642-56120-7>.
- [40] J. S. Sedita and J. M. O'Reilly, "A Thermally Stimulated Depolarization Current Study

- of Polymers in the Glass Transition Region,” *Polym. Eng. Sci.*, vol. 41, no. 1, pp. 15–22, 2001, DOI: <https://doi.org/10.1002/pen.10704>.
- [41] G. Floudas, “Dielectric Spectroscopy,” in *Polymer Science: A Comprehensive Reference*, Amsterdam: Elsevier, 2012, pp. 825–845, DOI: <https://doi.org/10.1016/B978-0-444-53349-4.00057-1>.
- [42] F. Henry, L. C. Costa, and M. Devassine, “The evolution of poly(lactic acid) degradability by dielectric spectroscopy measurements,” *Eur. Polym. J.*, vol. 41, no. 9, pp. 2122–2126, 2005, DOI: <https://doi.org/10.1016/j.eurpolymj.2005.03.006>.
- [43] Z.-M. Dang, J.-K. Yuan, J.-W. Zha, T. Zhou, S.-T. Li, and G.-H. Hu, “Fundamentals, processes and applications of high-permittivity polymer–matrix composites,” *Prog. Mater. Sci.*, vol. 57, no. 4, pp. 660–723, May 2012, DOI: <https://doi.org/10.1016/j.pmat sci.2011.08.001>.
- [44] T. A. Ezquerra, J. Majszczyk, F. J. Baltà-Calleja, E. López-Cabarcos, K. H. Gardner, and B. S. Hsiao, “Molecular dynamics of the  $\alpha$  relaxation during crystallization of a glassy polymer: A real-time dielectric spectroscopy study,” *Phys. Rev. B*, vol. 50, no. 9, pp. 6023–6031, Sep. 1994, DOI: <https://doi.org/10.1103/PhysRevB.50.6023>.
- [45] A. K. Jonscher, “The ‘universal’ dielectric response,” *Nature*, vol. 267, no. 5613, pp. 673–679, Jun. 1977, DOI: <https://doi.org/10.1038/267673a0>.
- [46] A. K. Jonscher, “The universal dielectric response and its physical significance,” *IEEE Trans. Electr. Insul.*, vol. 27, no. 3, pp. 407–423, Jun. 1992, DOI: <https://doi.org/10.1109/14.142701>.
- [47] C. T. Moynihan, “Analysis of electrical relaxation in glasses and melts with large concentrations of mobile ions,” *J. Non. Cryst. Solids*, vol. 172–174, pp. 1395–1407, Sep. 1994, DOI: [https://doi.org/10.1016/0022-3093\(94\)90668-8](https://doi.org/10.1016/0022-3093(94)90668-8).
- [48] J. C. Dyre and T. B. Schröder, “Universality of ac conduction in disordered solids,” *Rev. Mod. Phys.*, vol. 72, no. 3, pp. 873–892, Jul. 2000, DOI: <https://doi.org/10.1103/RevModPhys.72.873>.
- [49] A. S. Nowick and B.S. Lim, “Analysis of ac conductivity data for Na<sub>2</sub>O·3SiO<sub>2</sub> glass by stretched exponential and Jonscher power-law methods,” *J. Non. Cryst. Solids*, vol. 172–174, pp. 1389–1394, Sep. 1994, DOI: [https://doi.org/10.1016/0022-3093\(94\)90667-X](https://doi.org/10.1016/0022-3093(94)90667-X).
- [50] J. L. Barton, “Dielectric relaxation of some ternary alkali-alkaline earth-silicate glasses,” *Verres Refract*, vol. 20, p. 328, 1966.
- [51] T. Nakajima, “Annual Report,” in *Conference on Electric Insulation and Dielectric Phenomena (National Academy of Sciences, Washington D.C.)*, 1972, p. 168.

- [52] H. Namikawa, "Characterization of the diffusion process in oxide glasses based on the correlation between electric conduction and dielectric relaxation," *J. Non. Cryst. Solids*, vol. 18, no. 2, pp. 173–195, Sep. 1975, DOI: [https://doi.org/10.1016/0022-3093\(75\)90019-8](https://doi.org/10.1016/0022-3093(75)90019-8).
- [53] J. C. Maxwell, "ELECTRICITY AND MAGNETISM," in *A Treatise on Electricity and Magnetism*, Cambridge: Cambridge University Press, 1873, pp. xxxi–xxxiv, DOI: <https://doi.org/10.1017/CBO9780511709333.002>.
- [54] K. W. Wagner, "Erklärung der dielektrischen Nachwirkungsvorgänge auf Grund Maxwellscher Vorstellungen," *Arch. für Elektrotechnik*, vol. 2, no. 9, pp. 371–387, Sep. 1914, DOI: <https://doi.org/10.1007/BF01657322>.
- [55] R. W. Sillars, "The properties of a dielectric containing semiconducting particles of various shapes," *J. Inst. Electr. Eng.*, vol. 80, no. 484, pp. 378–394, Apr. 1937, DOI: <https://doi.org/10.1049/jiee-1.1937.0058>.
- [56] R. R. Bilboul, "A note on the permittivity of a double-layer ellipsoid," *J. Phys. D. Appl. Phys.*, vol. 2, no. 6, pp. 921–923, Jun. 1969, DOI: <https://doi.org/10.1088/0022-3727/2/6/420>.
- [57] G. Bánhegyi, "Comparison of electrical mixture rules for composites," *Colloid Polym. Sci.*, vol. 264, no. 12, pp. 1030–1050, Dec. 1986, DOI: <https://doi.org/10.1007/BF01410321>.
- [58] D. A. G. Bruggeman, "Berechnung verschiedener physikalischer Konstanten von heterogenen Substanzen. I. Dielektrizitätskonstanten und Leitfähigkeiten der Mischkörper aus isotropen Substanzen," *Ann. Phys.*, vol. 416, no. 7, pp. 636–664, 1935, DOI: <https://doi.org/10.1002/andp.19354160705>.
- [59] C. J. F. Böttcher, "The dielectric constant of crystalline powders," *Recl. des Trav. Chim. des Pays-Bas*, vol. 64, no. 2, pp. 47–51, 1945, DOI: <https://doi.org/10.1002/recl.19450640205>.
- [60] D. Polder and J. H. van Santen, "The effective permeability of mixtures of solids," *Physica*, vol. 12, no. 5, pp. 257–271, Aug. 1946, DOI: [https://doi.org/10.1016/S0031-8914\(46\)80066-1](https://doi.org/10.1016/S0031-8914(46)80066-1).
- [61] W. Y. Hsu, T. D. Gierke, and C. J. Molnar, "Morphological effects on the physical properties of polymer composites," *Macromolecules*, vol. 16, no. 12, pp. 1945–1947, Dec. 1983, DOI: <https://doi.org/10.1021/ma00246a028>.
- [62] H. Fricke, "A Mathematical Treatment of the Electric Conductivity and Capacity of Disperse Systems I. The Electric Conductivity of a Suspension of Homogeneous



- Spheroids,” *Phys. Rev.*, vol. 24, no. 5, pp. 575–587, Nov. 1924, DOI: <https://doi.org/10.1103/PhysRev.24.575>.
- [63] A. I. Oliva-Avilés, F. Avilés, V. Sosa, and G. D. Seidel, “Dielectrophoretic modeling of the dynamic carbon nanotube network formation in viscous media under alternating current electric fields,” *Carbon N. Y.*, vol. 69, pp. 342–354, Apr. 2014, DOI: <https://doi.org/10.1016/j.carbon.2013.12.035>.
- [64] C. Park, J. Wilkinson, S. Banda, Z. Ounaies, K. E. Wise, G. Sauti, P. T. Lillehei, and J. S. Harrison, “Aligned single-wall carbon nanotube polymer composites using an electric field,” *J. Polym. Sci. Part B Polym. Phys.*, vol. 44, no. 12, pp. 1751–1762, Jun. 2006, DOI: <https://doi.org/10.1002/polb.20823>.
- [65] J. Shang, Y. Zhang, L. Yu, B. Shen, F. Lv, and P. K. Chu, “Fabrication and dielectric properties of oriented polyvinylidene fluoride nanocomposites incorporated with graphene nanosheets,” *Mater. Chem. Phys.*, vol. 134, no. 2–3, pp. 867–874, Jun. 2012, DOI: <https://doi.org/10.1016/j.matchemphys.2012.03.082>.
- [66] S. Wu, R. B. Ladani, J. Zhang, E. Bafekrpour, K. Ghorbani, A. P. Mouritz, A. J. Kinloch, and C. H. Wang, “Aligning multilayer graphene flakes with an external electric field to improve multifunctional properties of epoxy nanocomposites,” *Carbon N. Y.*, vol. 94, pp. 607–618, Nov. 2015, DOI: <https://doi.org/10.1016/j.carbon.2015.07.026>.
- [67] P. S. Goh, A. F. Ismail, and B. C. Ng, “Directional alignment of carbon nanotubes in polymer matrices: Contemporary approaches and future advances,” *Compos. Part A Appl. Sci. Manuf.*, vol. 56, pp. 103–126, 2014, DOI: <https://doi.org/10.1016/j.compositesa.2013.10.001>.
- [68] C. Park and R. E. Robertson, “Alignment of particles by an electric field,” *Mater. Sci. Eng. A*, vol. 257, no. 2, pp. 295–311, Dec. 1998, DOI: [https://doi.org/10.1016/S0921-5093\(98\)00848-X](https://doi.org/10.1016/S0921-5093(98)00848-X).
- [69] T. I. W. Schnoor, G. Smith, D. Eder, K. K. K. Koziol, G. Tim Burstein, A. H. Windle, and K. Schulte, “The production of aligned MWCNT/polypyrrole composite films,” *Carbon N. Y.*, vol. 60, pp. 229–235, 2013, DOI: <https://doi.org/10.1016/j.carbon.2013.04.016>.
- [70] R. J. Castellano, C. Akin, G. Giraldo, S. Kim, F. Fornasiero, and J. W. Shan, “Electrokinetics of scalable, electric-field-assisted fabrication of vertically aligned carbon-nanotube/polymer composites,” *J. Appl. Phys.*, vol. 117, no. 21, p. 214306, Jun. 2015, DOI: <https://doi.org/10.1063/1.4921948>.
- [71] C. A. Martin, J. K. W. Sandler, A. H. Windle, M.-K. Schwarz, W. Bauhofer, K. Schulte, and M. S. P. Shaffer, “Electric field-induced aligned multi-wall carbon nanotube

- networks in epoxy composites,” *Polymer (Guildf.)*, vol. 46, no. 3, pp. 877–886, Jan. 2005, DOI: <https://doi.org/10.1016/j.polymer.2004.11.081>.
- [72] O. Osazuwa, M. Kontopoulou, P. Xiang, Z. Ye, and A. Docoslis, “Electrically conducting polyolefin composites containing electric field-aligned multiwall carbon nanotube structures: The effects of process parameters and filler loading,” *Carbon N. Y.*, vol. 72, pp. 89–99, Jun. 2014, DOI: <https://doi.org/10.1016/j.carbon.2014.01.059>.
- [73] R. Landauer, “Electrical conductivity in inhomogeneous media,” in *AIP Conference Proceedings*, Jul. 1978, vol. 40, no. 1, pp. 2–45, DOI: <https://doi.org/10.1063/1.31150>.
- [74] K. S. Mendelson and M. H. Cohen, “The effect of grain anisotropy on the electrical properties of sedimentary rocks,” *Geophysics*, vol. 47, no. 2, pp. 257–263, Feb. 1982, DOI: <https://doi.org/10.1190/1.1441332>.
- [75] D. S. McLachlan, C. Chiteme, W. D. Heiss, and J. Wu, “Fitting the DC conductivity and first order AC conductivity results for continuum percolation media, using percolation theory and a single phenomenological equation,” *Phys. B Condens. Matter*, vol. 338, no. 1–4, pp. 261–265, Oct. 2003, DOI: <https://doi.org/10.1016/j.physb.2003.08.003>.
- [76] D. S. McLachlan, M. Blaszkiewicz, and R. E. Newnham, “Electrical Resistivity of Composites,” *J. Am. Ceram. Soc.*, vol. 73, no. 8, pp. 2187–2203, Aug. 1990, DOI: <https://doi.org/10.1111/j.1151-2916.1990.tb07576.x>.
- [77] D. S. McLachlan, “Analytical Functions for the dc and ac Conductivity of Conductor-Insulator Composites,” *J. Electroceramics*, vol. 5, no. 2, pp. 93–110, 2000, DOI: <https://doi.org/10.1023/A:1009954017351>.
- [78] D. S. McLachlan, C. Chiteme, C. Park, K. E. Wise, S. E. Lowther, P. T. Lillehei, E. J. Siochi, and J. S. Harrison, “AC and DC percolative conductivity of single wall carbon nanotube polymer composites,” *J. Polym. Sci. Part B Polym. Phys.*, vol. 43, no. 22, pp. 3273–3287, Nov. 2005, DOI: <https://doi.org/10.1002/polb.20597>.
- [79] X. Tian, M. E. Itkis, E. B. Bekyarova, and R. C. Haddon, “Anisotropic Thermal and Electrical Properties of Thin Thermal Interface Layers of Graphite Nanoplatelet-Based Composites,” *Sci. Rep.*, vol. 3, no. 1, p. 1710, Dec. 2013, DOI: <https://doi.org/10.1038/srep01710>.
- [80] S. Y. Kim, Y. J. Noh, and J. Yu, “Thermal conductivity of graphene nanoplatelets filled composites fabricated by solvent-free processing for the excellent filler dispersion and a theoretical approach for the composites containing the geometrized fillers,” *Compos. Part A Appl. Sci. Manuf.*, vol. 69, pp. 219–225, Feb. 2015, DOI: <https://doi.org/10.1016/J.COMPOSITESA.2014.11.018>.

- [81] M. Gresil, Z. Wang, Q.-A. Poutrel, and C. Soutis, “Thermal Diffusivity Mapping of Graphene Based Polymer Nanocomposites,” *Sci. Rep.*, vol. 7, no. 1, p. 5536, Dec. 2017, DOI: <https://doi.org/10.1038/s41598-017-05866-0>.
- [82] R. Pal, “On the Lewis–Nielsen model for thermal/electrical conductivity of composites,” *Compos. Part A Appl. Sci. Manuf.*, vol. 39, no. 5, pp. 718–726, May 2008, DOI: <https://doi.org/10.1016/J.COMPOSITESA.2008.02.008>.
- [83] T. Mori and K. Tanaka, “Average stress in matrix and average elastic energy of materials with misfitting inclusions,” *Acta Metall.*, vol. 21, no. 5, pp. 571–574, May 1973, DOI: [https://doi.org/10.1016/0001-6160\(73\)90064-3](https://doi.org/10.1016/0001-6160(73)90064-3).
- [84] Y. Benveniste, “A new approach to the application of Mori-Tanaka’s theory in composite materials,” *Mech. Mater.*, vol. 6, no. 2, pp. 147–157, Jun. 1987, DOI: [https://doi.org/10.1016/0167-6636\(87\)90005-6](https://doi.org/10.1016/0167-6636(87)90005-6).
- [85] M. M. Shokrieh, S. M. Ghoreishi, and M. Esmkhani, “Toughening mechanisms of nanoparticle-reinforced polymers,” in *Toughening Mechanisms in Composite Materials*, Cambridge: Elsevier (Woodhead Publishing United Kingdom), 2015, pp. 295–320, DOI: <https://doi.org/10.1016/B978-1-78242-279-2.00011-1>.
- [86] D. Lee and Y. S. Song, “Modeling the effects of elastic modulus and thermal expansion coefficient on the shrinkage of glass fiber reinforced composites,” *Compos. Part B Eng.*, vol. 146, pp. 98–105, Aug. 2018, DOI: <https://doi.org/10.1016/J.COMPOSITESB.2018.03.047>.
- [87] W. Voigt, “Ueber die Beziehung zwischen den beiden Elasticitätsconstanten isotroper Körper,” *Ann. Phys.*, vol. 274, no. 12, pp. 573–587, Jan. 1889, DOI: <https://doi.org/10.1002/andp.18892741206>.
- [88] A. Reuss, “Berechnung der Fließgrenze von Mischkristallen auf Grund der Plastizitätsbedingung für Einkristalle,” *ZAMM - Zeitschrift für Angew. Math. und Mech.*, vol. 9, no. 1, pp. 49–58, Jan. 1929, DOI: <https://doi.org/10.1002/zamm.19290090104>.
- [89] H. Fricke, “The Electric Permittivity of a Dilute Suspension of Membrane-Covered Ellipsoids,” *J. Appl. Phys.*, vol. 24, no. 5, pp. 644–646, May 1953, DOI: <https://doi.org/10.1063/1.1721343>.
- [90] J. C. M. Garnett, “Colours in Metal Glasses and in Metallic Films,” *Philos. Trans. R. Soc. A Math. Phys. Eng. Sci.*, vol. 203, no. 359–371, pp. 385–420, Jan. 1904, DOI: <https://doi.org/10.1098/rsta.1904.0024>.
- [91] M. Wang and N. Pan, “Predictions of effective physical properties of complex multiphase materials,” *Mater. Sci. Eng. R Reports*, vol. 63, no. 1, pp. 1–30, Dec. 2008, DOI:

- <https://doi.org/10.1016/J.MSER.2008.07.001>.
- [92] Nanocyl SA, “Technical data sheet NC7000-V08.” Accessed: Apr. 03, 2019. [Online]. Available: <https://www.nanocyl.com/product/nc7000/>.
- [93] OcSiAl, “Technical information Tuball.” Accessed: Apr. 03, 2019. [Online]. Available: <http://tuball.com/en/about-tuball>.
- [94] Unipetrol, “Product Sheet Chezacarb.” Accessed: Apr. 03, 2019. [Online]. Available: <http://www.unipetrol.cz/en/OurProducts/PetrochemicalProducts/CarbonBlackCHEZACARB/Pages/default.aspx>.
- [95] Total-Corbion, “Technical sheet Luminy PLA neat resins.” Accessed: Apr. 03, 2019. [Online]. Available: <https://www.total-corbion.com/downloads/>.
- [96] Hexion Inc., “Technical data sheet EPIKOTE Resin MGS RIMR426.” Accessed: Apr. 03, 2019. [Online]. Available: <https://www.hexion.com/en-GB/brand/EPIKOTE/>.
- [97] Rubitherm Technologies GmbH, “RT42 data sheet.” Accessed: Apr. 03, 2019. [Online]. Available: [https://www.rubitherm.eu/media/products/datasheets/Techdata\\_RT42\\_EN\\_06082018.PDF](https://www.rubitherm.eu/media/products/datasheets/Techdata_RT42_EN_06082018.PDF).
- [98] C. Laurent, E. Flahaut, and A. Peigney, “The weight and density of carbon nanotubes versus the number of walls and diameter,” *Carbon N. Y.*, vol. 48, no. 10, pp. 2994–2996, Aug. 2010, DOI: <https://doi.org/10.1016/J.CARBON.2010.04.010>.
- [99] G. Liu, Y. Zhao, K. Deng, Z. Liu, W. Chu, J. Chen, Y. Yang, K. Zheng, H. Huang, W. Ma, *et al.*, “Highly Dense and Perfectly Aligned Single-Walled Carbon Nanotubes Fabricated by Diamond Wire Drawing Dies,” *Nano Lett.*, vol. 8, no. 4, pp. 1071–1075, Apr. 2008, DOI: <https://doi.org/10.1021/nl073007o>.
- [100] L. D. Filip and V. Filip, “Influence of electron quantum confinement on the strength of carbon nanotube bundles,” *Solid State Electron. Lett.*, vol. 1, no. 1, pp. 1–9, Jan. 2019, DOI: <https://doi.org/10.1016/J.SSEL.2018.09.001>.
- [101] C. J. Edgcombe, S. M. Masur, E. B. Linscott, J. A. J. Whaley-Baldwin, and C. H. W. Barnes, “Analysis of a capped carbon nanotube by linear-scaling density-functional theory,” *Ultramicroscopy*, vol. 198, pp. 26–32, Mar. 2019, DOI: <https://doi.org/10.1016/J.ULTRAMIC.2018.11.007>.
- [102] G. Kirchhoff, “Zur Theorie des Condensators,” *Berlin Verl. d. Kgl. Akad. d. Wiss.*, vol. March, p. 144, 1877, Accessed: Apr. 03, 2019. [Online]. Available: <http://histmath-heidelberg.de/txt/bbaw-kirchhoff.htm>.
- [103] NOVOCONTROL Technologies GmbH & Co. KG, “Alpha and Beta Analyzers User’s

- Manual,” 2005. Accessed: Apr. 03, 2019. [Online]. Available: <https://www.novocontrol.de/php/request.php>.
- [104] J. M. S. Prewitt and M. L. Mendelsohn, “The Analysis of Cell Images,” *Ann. N. Y. Acad. Sci.*, vol. 128, no. 3, pp. 1035–1053, Dec. 2006, DOI: <https://doi.org/10.1111/j.1749-6632.1965.tb11715.x>.
- [105] L. S. Lasdon, R. L. Fox, and M. W. Ratner, “Nonlinear optimization using the generalized reduced gradient method,” *Rev. française d’automatique, informatique, Rech. opérationnelle. Rech. opérationnelle*, vol. 8, no. V3, pp. 73–103, Mar. 1974, DOI: <https://doi.org/10.1051/ro/197408V300731>.
- [106] G. Banhegyi, “Numerical analysis of complex dielectric mixture formulae,” *Colloid Polym. Sci.*, vol. 266, no. 1, pp. 11–28, Jan. 1988, DOI: <https://doi.org/10.1007/BF01451527>.
- [107] C.-W. Nan, “Physics of inhomogeneous inorganic materials,” *Prog. Mater. Sci.*, vol. 37, no. 1, pp. 1–116, Jan. 1993, DOI: [https://doi.org/10.1016/0079-6425\(93\)90004-5](https://doi.org/10.1016/0079-6425(93)90004-5).
- [108] S. Pfeifer, S.-H. Park, and P. R. Bandaru, “Modeling the Relative Dielectric Permittivity and Impedance of Carbon Nanotube Constituted Polymer Composites in the Sub-GHz Regime,” *ECS Solid State Lett.*, vol. 2, no. 1, pp. M5–M7, Oct. 2012, DOI: <https://doi.org/10.1149/2.006301ssl>.
- [109] H. Pang, L. Xu, D.-X. Yan, and Z.-M. Li, “Conductive polymer composites with segregated structures,” *Prog. Polym. Sci.*, vol. 39, no. 11, pp. 1908–1933, Nov. 2014, DOI: <https://doi.org/10.1016/j.progpolymsci.2014.07.007>.
- [110] T. Villmow, S. Pegel, P. Pötschke, and U. Wagenknecht, “Influence of injection molding parameters on the electrical resistivity of polycarbonate filled with multi-walled carbon nanotubes,” *Compos. Sci. Technol.*, vol. 68, no. 3–4, pp. 777–789, Mar. 2008, DOI: <https://doi.org/10.1016/j.compscitech.2007.08.031>.
- [111] T. Villmow, P. Pötschke, S. Pegel, L. Häussler, and B. Kretschmar, “Influence of twin-screw extrusion conditions on the dispersion of multi-walled carbon nanotubes in a poly(lactic acid) matrix,” *Polymer (Guildf.)*, vol. 49, no. 16, pp. 3500–3509, Jul. 2008, DOI: <https://doi.org/10.1016/j.polymer.2008.06.010>.
- [112] P. Pötschke, S. M. Dudkin, and I. Alig, “Dielectric spectroscopy on melt processed polycarbonate—multiwalled carbon nanotube composites,” *Polymer (Guildf.)*, vol. 44, no. 17, pp. 5023–5030, Aug. 2003, DOI: [https://doi.org/10.1016/S0032-3861\(03\)00451-8](https://doi.org/10.1016/S0032-3861(03)00451-8).
- [113] I. Alig, P. Pötschke, D. Lellinger, T. Skipa, S. Pegel, G. R. Kasaliwal, and T. Villmow,

- “Establishment, morphology and properties of carbon nanotube networks in polymer melts,” *Polymer (Guildf)*, vol. 53, no. 1, pp. 4–28, Jan. 2012, DOI: <https://doi.org/10.1016/j.polymer.2011.10.063>.
- [114] C. A. Martin, J. K. W. Sandler, M. S. P. Shaffer, M.-K. Schwarz, W. Bauhofer, K. Schulte, and A. H. Windle, “Formation of percolating networks in multi-wall carbon-nanotube–epoxy composites,” *Compos. Sci. Technol.*, vol. 64, no. 15, pp. 2309–2316, Nov. 2004, DOI: <https://doi.org/10.1016/j.compscitech.2004.01.025>.
- [115] P. L. McEuen and M. S. Fuhrer, “Single-walled carbon nanotube electronics,” *IEEE Trans. Nanotechnol.*, vol. 1, no. 1, pp. 78–85, Mar. 2002, DOI: <https://doi.org/10.1109/TNANO.2002.1005429>.
- [116] E. A. Laird, F. Kueemeth, G. A. Steele, K. Grove-Rasmussen, J. Nygård, K. Flensberg, and L. P. Kouwenhoven, “Quantum transport in carbon nanotubes,” *Rev. Mod. Phys.*, vol. 87, no. 3, pp. 703–764, Jul. 2015, DOI: <https://doi.org/10.1103/RevModPhys.87.703>.
- [117] L. Xin and Z. Chen, “Curved Pi-Conjugation, Aromaticity, and the Related Chemistry of Small Fullerenes and Single-Walled Carbon Nanotubes,” *Chem. Rev.*, vol. 105, no. 10, pp. 3643–3696, 2005, DOI: <https://doi.org/10.1021/CR030093D>.
- [118] M. P. Hughes, “AC electrokinetics: applications for nanotechnology,” *Nanotechnology*, vol. 11, no. 2, pp. 124–132, Jun. 2000, DOI: <https://doi.org/10.1088/0957-4484/11/2/314>.
- [119] T. Prasse, “Electric anisotropy of carbon nanofibre/epoxy resin composites due to electric field induced alignment,” *Compos. Sci. Technol.*, vol. 63, no. 13, pp. 1835–1841, Oct. 2003, DOI: [https://doi.org/10.1016/S0266-3538\(03\)00019-8](https://doi.org/10.1016/S0266-3538(03)00019-8).
- [120] F. Lionetto, E. Calò, F. Di Benedetto, D. Pisignano, and A. Maffezzoli, “A methodology to orient carbon nanotubes in a thermosetting matrix,” *Compos. Sci. Technol.*, vol. 96, pp. 47–55, 2014, DOI: <https://doi.org/10.1016/j.compscitech.2014.02.016>.

## List of Publications

- J. F. Blanco-Villalba, I. Recio, J. Gómez-Cordón, C. Hübner, “Improving the processability of graphene nanoplatelets in polyamide 6 during melt compounding extrusion,” in *AIP Conference Proceedings*, 2019, vol. 2055, no. 1, pp. 090010, DOI: <https://doi.org/10.1063/1.5084888>. (Peer-reviewed article).
- J. F. Blanco-Villalba, I. Mikonsaari, C. Hübner, “Dielectric spectroscopy and effective medium models to characterize polymer nanocomposites,” in *NanoCarbon Annual Conference 2018*, Würzburg, February 2018 (Presentation and poster).
- J. F. Blanco-Villalba, I. Recio, J. Gómez-Cordón, C. Hübner, “Improving the processability of graphene nanoplatelets in polyamide 6 during melt compounding extrusion,” in *Europe/Africa Conference, Polymer Processing Society PPS*, Dresden, June 2017. (Presentation).
- J.F. Blanco-Villalba, R. Valente, D. Vlasveld, I. Mikonsaari, C. Hübner, “Effect of the fluid flow on the distribution of carbon nanotubes during the injection moulding of polymer nanocomposites,” in *Programme and Book of Abstracts of the 9th International Conference on Broadband Dielectric Spectroscopy and its Applications*, 2016, p. 171, ISBN: 97888652283547, Pisa, September 2016. (Abstract and poster).

## Appendix A: Proof of the Multiplicity of Solutions in the Regression Analysis on the e-PvSB Model

Given a composite with a dispersion  $d$  and agglomerates described by the network factor  $F_n$  (with corresponding depolarization factor  $A_n = f(F_n)$ ), it can be proved that there are infinite other composites, dispersion  $d_2$  and agglomerates described by the network factor  $F_{n2}$  (with corresponding depolarization factor  $A_{n2} = f(F_{n2})$ ), that feature an identical experimental curve of composite permittivity ( $\bar{\epsilon}$ ) versus filler volume concentration ( $v$ ).

Given the e-PvSB model (equation 4-19), assuming that both composites share the same matrix ( $\bar{\epsilon}_m$ ) and filler ( $a_f, A_{f\parallel}, A_{f\perp}$ ), and imposing identical values of composite permittivity ( $\bar{\epsilon}$ ) and filler volume concentration ( $v$ ), we obtain:

$$\bar{\epsilon} = \frac{\epsilon_m}{1 - vd \left[ \frac{a_f}{A_{f\parallel}} + \frac{(1 - a_f)}{A_{f\perp}} \right] + \frac{v(1 - d)}{A_n}} = \frac{\epsilon_m}{1 - vd_2 \left[ \frac{a_f}{A_{f\parallel}} + \frac{(1 - a_f)}{A_{f\perp}} \right] + \frac{v(1 - d_2)}{A_{n2}}} \quad \text{A-1}$$

The denominators in the second and third members of previous equality are equal:

$$1 - vd \left[ \frac{a_f}{A_{f\parallel}} + \frac{(1 - a_f)}{A_{f\perp}} \right] + \frac{v(1 - d)}{A_n} = 1 - vd_2 \left[ \frac{a_f}{A_{f\parallel}} + \frac{(1 - a_f)}{A_{f\perp}} \right] + \frac{v(1 - d_2)}{A_{n2}} \quad \text{A-2}$$

Solving for  $A_{n2}$  we obtain:

$$A_{n2} = \frac{1 - d_2}{(d - d_2) \left( \frac{a_f}{A_{f\parallel}} + \frac{(1 - a_f)}{A_{f\perp}} \right) + \frac{1 - d}{A_n}} \quad \text{A-3}$$

Equation A-3 provides an infinite number of combinations of  $A_{n2}$  and  $d_2$  that provides composites with identical permittivity to the original composite if  $A_n$  and  $d$  (*Q.E.D.*).

The value of reference network factor ( $F_n(d = 0) \equiv F_{n0}$ ) and the corresponding depolarization factor ( $A_{n0}$ ) can unequivocally describe a set of equivalent composites. It can be proved by imposing  $d_2 = 0$  in equation A-4:



$$A_{n0} = \frac{1}{d \left( \frac{a_f}{A_{f\parallel}} + \frac{(1 - a_f)}{A_{f\perp}} \right) + \frac{1 - d}{A_n}} \quad \text{A-4}$$

Equation A-4 provides the curves that emerge in the matrices of coefficients of determination of Appendix B.

## Appendix B: Matrices of Coefficients of Determination

Matrices of coefficients of determination ( $R^2$ ) of the e-PvSB model with respect to data of experimental or simulated composites. Colours represent the value of the coefficient of determination, ranging from red ( $R^2 \leq 0.7$ , insufficient fitting) to green ( $R^2 = 1$ , perfect fitting), going through yellow ( $R^2 = 0.9$ , acceptable fitting).

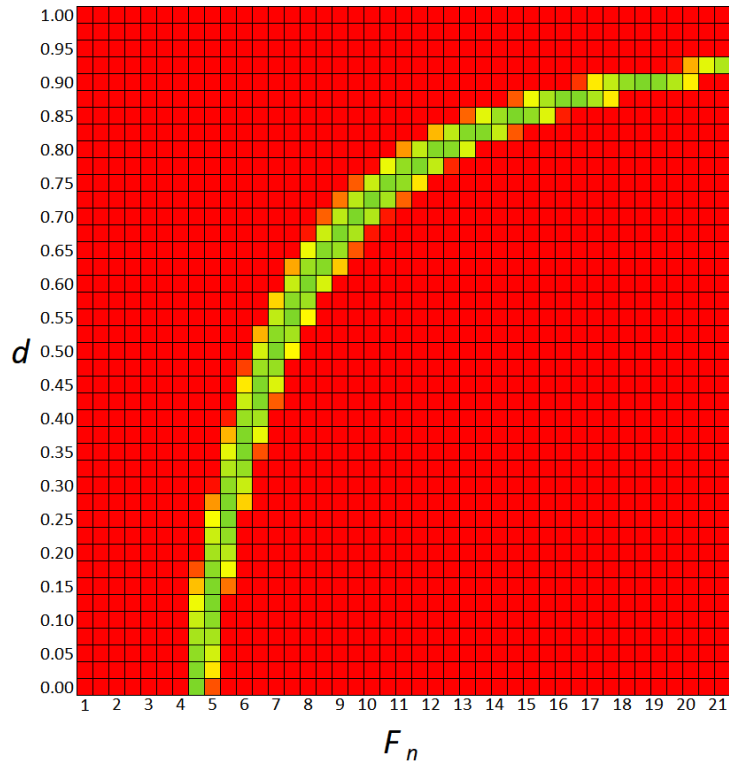


Figure 76. Matrix of coefficients of determination ( $R^2$ ) of the e-PvSB model with respect to a simulated composite (Figure 46,  $\underline{d} = \underline{0}$ ) for different combinations of dispersion ( $d$ ) and network factor ( $F_n$ ).

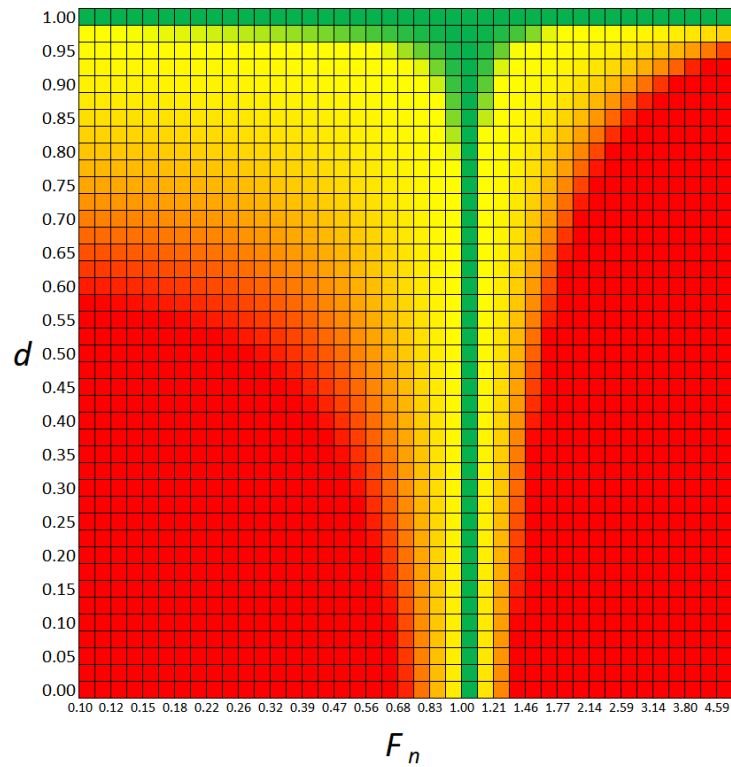


Figure 77. Matrix of coefficients of determination ( $R^2$ ) of the e-PvSB model with respect to a simulated composite (Figure 46,  $d = 1$ ) for different combinations of dispersion ( $d$ ) and network factor ( $F_n$ ).

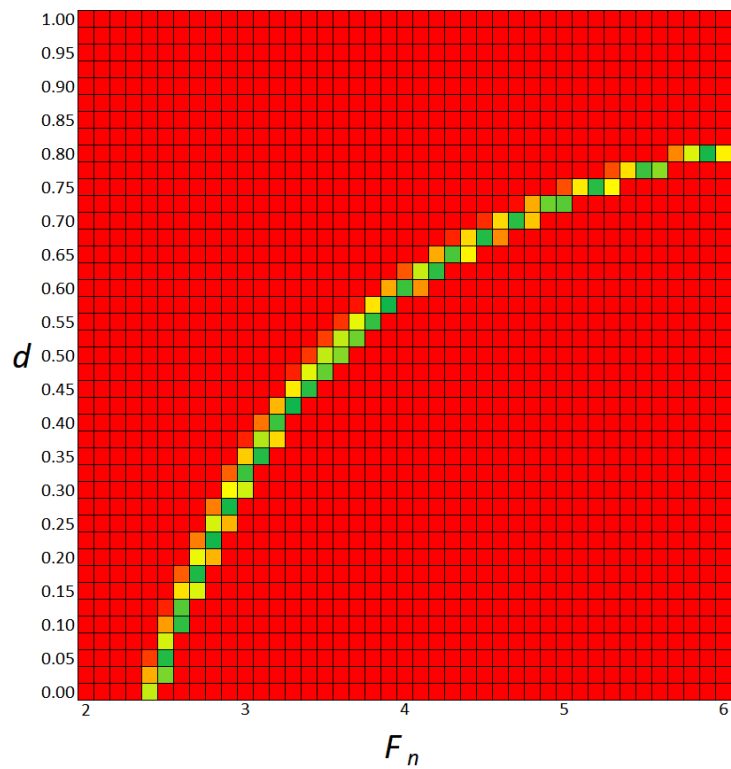


Figure 78. Matrix of coefficients of determination ( $R^2$ ) of the e-PvSB model with respect to PLA/MWNT composites with good dispersion for different combinations of dispersion ( $d$ ) and network factor ( $F_n$ ).

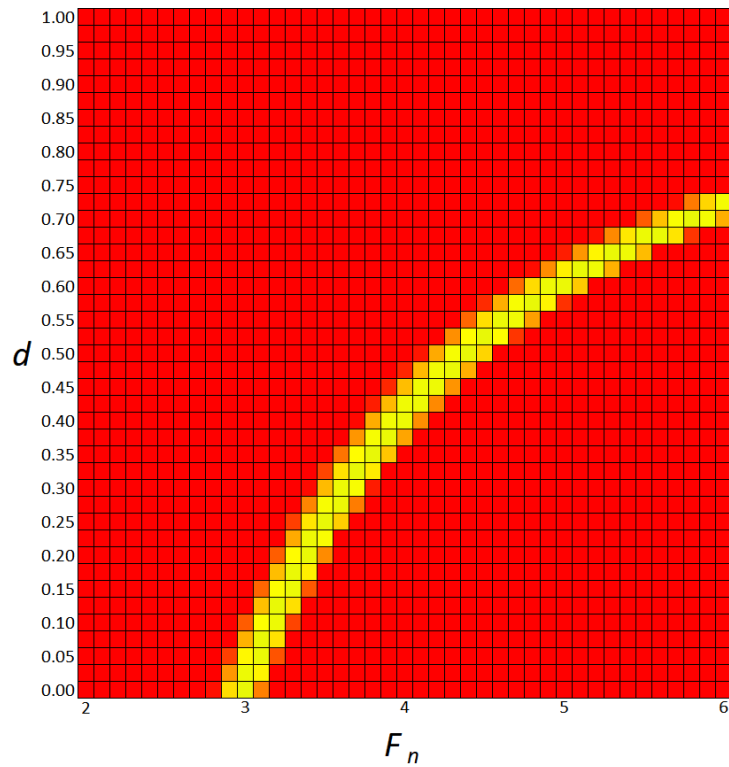


Figure 79. Matrix of coefficients of determination ( $R^2$ ) of the e-PvSB model with respect to PLA/MWNT composites with bad dispersion for different combinations of dispersion ( $d$ ) and network factor ( $F_n$ ).

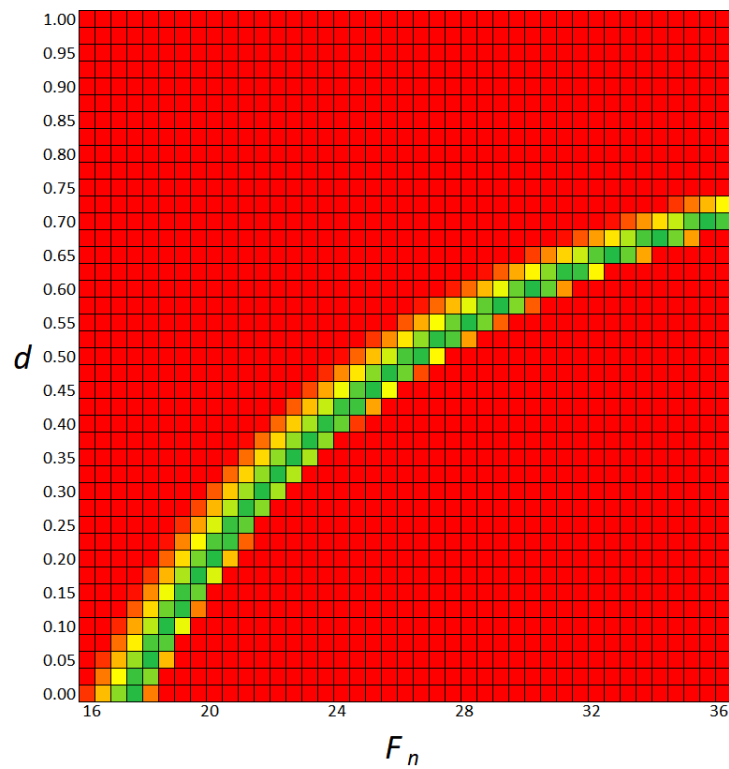


Figure 80. Matrix of coefficients of determination ( $R^2$ ) of the e-PvSB model with respect to PLA/CB composites with good dispersion for different combinations of dispersion ( $d$ ) and network factor ( $F_n$ ).

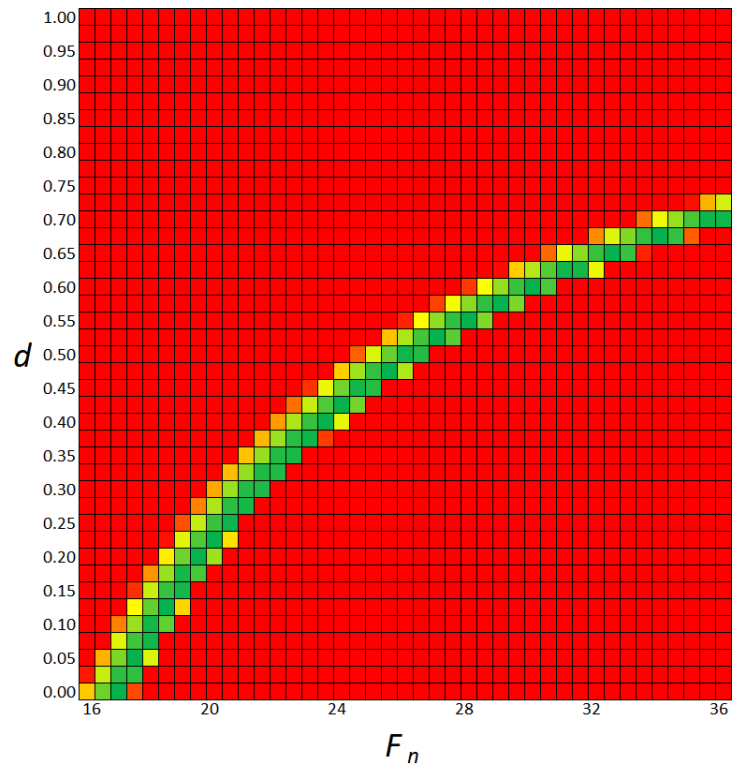


Figure 81. Matrix of coefficients of determination ( $R^2$ ) of the e-PvSB model with respect to PLA/CB composites with bad dispersion for different combinations of dispersion ( $d$ ) and network factor ( $F_n$ ).

## Appendix C: Conductivity Spectra of Epoxy Composites

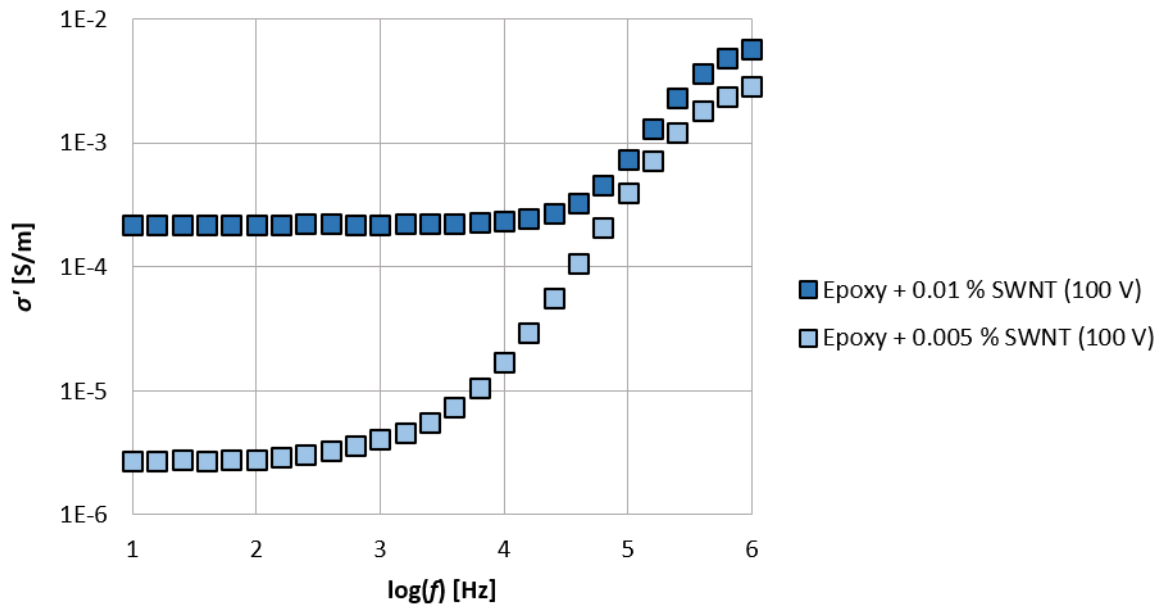


Figure 82. Conductivity spectra of two aligned composites with a significant different in DC conductivity (low-frequency limit). The values of conductivity at 1 MHz do not represent that different.

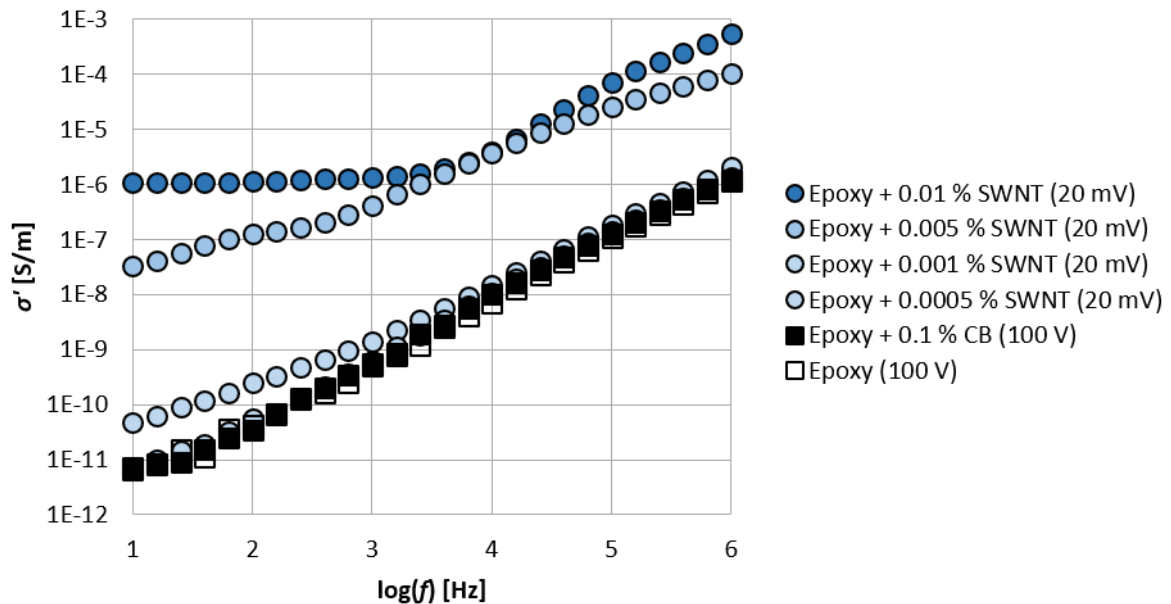


Figure 83. Conductivity spectra of non-aligned composites for SWNT mass concentrations between 0.0005 % and 0.01 %. The spectra of unfilled epoxy (black) and an aligned epoxy/CB composite are also included. The DC conductivity cannot be determined for the samples without a low-frequency plateau.

## List of Figures

- Figure 1. Characteristic frequency dependence of the real (red) and imaginary (blue) parts of permittivity for different dielectric mechanisms. (Reproduced from [20])..... 4
- Figure 2. Sinusoidal input and output signals (voltage and current, respectively) versus time. The amplitudes ( $U_0, I_0$ ), phase difference ( $\phi$ ) and period or inverse of frequency ( $f^{-1}$ ) are indicated. .... 6
- Figure 3. Real (blue) and imaginary (red) part of permittivity as a function of angular frequency for a material featuring electrode polarization, conductivity and a relaxation process..... 9
- Figure 4. Complex dielectric permittivity for the Havriliak/Negami function with: (a)  $\gamma = 1$ ; (b)  $\beta = 1$  ( $\tau_{HN} = 1$  [s],  $\Delta\epsilon = 1$ ,  $\epsilon_\infty = 1$ ). Reproduced from [23]..... 10
- Figure 5. Imaginary part of permittivity ( $\epsilon''$ ) for Jonscher processes with  $s = 1$  and  $s = 0.8$  and an ohmic process (equivalent to a Jonscher process with  $s = 0$ ). .... 12
- Figure 6. (a) Two layers of different materials in series, with  $\epsilon_i$  and  $\sigma_{ri}$  their permittivity and conductivity, respectively. (b) Equivalent circuit, with:  $C_i$ , capacity;  $G_i$ , conductance;  $A$ , area of the electrodes;  $D_i$ , depth of the layer  $i$ . Reproduced from [23]. .... 13
- Figure 7. (a) Spherical particle to derive Maxwell's equations for a suspension. (b) Model to derive the mixture equations. The small particles are the same as sketched in (a). Reproduced from [23]. .... 14
- Figure 8. Schematic representation of a two-component composite, layered parallel to the disturbance field, as established in the Voigt model. .... 17
- Figure 9. Schematic representation of a two-component composite, layered perpendicular to the disturbance field, as established in the Reuss model. .... 17
- Figure 10. Schematic representation of the effective medium approach. .... 18
- Figure 11. Parallel ( $A_1$ ) and perpendicular ( $A_2 = A_3$ ) depolarization factors of spheroids as a function of the aspect ratio ( $AR$ ). The convention for orientation described in section 2.2.5 is applied. .... 24

Figure 12. Leistritz Micro 27 mm 40 L/D Extruder.....	28
Figure 13. Thermo Haake™ MiniLab with conical counter-rotating screws.....	29
Figure 14. Profile view of the cell where the epoxy/SWNT suspensions were simultaneously cured and characterized.....	30
Figure 15. Schematic representation of the reference samples for the cases of: parallel (left) and perpendicular (right) alignment with respect to the electric field.....	31
Figure 16. Experimental setup for the measurement of dielectric properties at controlled temperatures.....	33
Figure 17. Representation of an infinite parallel-plate capacitor (left) and border or fringing effects on a real finite capacitor (right).....	35
Figure 18. Relative influence of the border effects for a 40 mm diameter electrode for different thicknesses. Comparison of theoretical values with FEM (finite element method) simulations in Comsol Multiphysics®.....	36
Figure 19. Novocontrol's Alpha impedance analyzer accuracy specification [103].....	37
Figure 20. Definition of the alignment parameter, $a$ , and schematic representation of composites for different values of $a$ : 1, 1/3 and 0.....	40
Figure 21. Definition of the dispersion parameter, $d$ , and schematic representation of composites for different values of $d$ : 1, 1/2 and 0.....	41
Figure 22. Schematic representation of the reference samples for the cases of: parallel (left) and perpendicular (right) alignment with respect to the electric field.....	42
Figure 23. Modelled and measured permittivity for wax/silver reference samples with different orientations.....	43
Figure 24. Modelled and measured permittivity for wax/silver reference samples with different filler concentrations.....	44
Figure 25. Modelled and measured permittivity for wax/silver and wax/graphite reference samples.....	45



Figure 26. Simulated geometry: Prismatic composite with an ellipsoidal filler (left) and its corresponding mesh (right). .....	46
Figure 27. Relative permittivity of composites with different volume concentrations of conductive spherical fillers.....	47
Figure 28. Relative permittivity of composites with different volume concentrations of conductive prolate ellipsoidal fillers oriented: parallel (top), randomly (middle) and perpendicular (bottom) with respect to the electric field. ....	48
Figure 29. Simulated composites with different filler distances. Cases in left and right are equivalent. ....	49
Figure 30. Permittivity of the composites described in Figure 29. The fillers are evenly distributed when the relative closeness is 0, and make contact when its value is $\pm 1$ . The line is a visual guidance. ....	50
Figure 31. Simulated composites with different distances between fillers and electrodes. ....	51
Figure 32. Permittivity of the composites showed in Figure 31. The line is a visual guidance. ....	51
Figure 33. Simulated composites with different number of layers of fillers. The filler concentration remains constant. ....	52
Figure 34. Permittivity of the composites described in Figure 33. The line is a visual guidance. ....	53
Figure 35. Simulated fillers with different curvature angles ( $\alpha_{max}$ ), for an electric field in the vertical direction.....	53
Figure 36. Simulated and modelled permittivity of the composites with curved fillers described in Figure 35 for different values of the curve angle ( $\alpha_{max}$ ). ....	55
Figure 37. Simulated composites with spherical fillers forming spheroidal (left) and elongated (right) agglomerates. Both agglomerates have the same number of equally sized spheres. ....	56

Figure 38. Permittivity of composites with volume concentration of 1 % of spherical filler in different configurations: isolated fillers, spheroidal agglomerates and elongated agglomerates. ....	56
Figure 39. Chains of ellipsoidal fillers arranged parallel (left) and perpendicular (right) to the electric field. ....	57
Figure 40. Permittivity of composites with different unidirectional chains of fillers as a function of the number of fillers per chain for a given volumetric concentration of 0.1 %. ....	58
Figure 41. Spheroidal (left) and elongated (right) agglomerates. The aspect ratio of their equivalent ellipsoids parallel to the electric field ( $AR_{ee\parallel}$ ), as calculated with the PvSB model, are indicated. ....	59
Figure 42. Network factor, in logarithmic scale, of the networks shown in Table 5. ....	61
Figure 43. Network factor of the networks represented in Table 6. ....	63
Figure 44. Visual representation of the e-PvSB model (equations 4-17 and 4-18), featuring examples of fillers. ....	64
Figure 45. Method to obtain morphological information from experimental data using the e-PvSB model. ....	64
Figure 46. Spherical fillers: isolated (grey) and forming chains (blue). Simulated composites with different degrees of dispersion: 0, 0.5 and 1. ....	66
Figure 47. Simulated and modelled permittivity for the composite represented in Figure 46. The values of dispersion (shown in this figure) were inputs to the e-PvSB model. A value of $F_n = 5.1 \pm 0.3$ was found for the network (for $d = 1$ there is no network and $F_n$ is therefore not defined). ....	66
Figure 48. Matrix of coefficients of determination ( $R^2$ ) of the e-PvSB model with respect to a simulated composite (with $d = 0.5$ ) for different combinations of dispersion ( $d$ ) and network factor ( $F_n$ ). Colours represent the value of the coefficient of determination, ranging from red ( $R^2 \leq 0.7$ , insufficient fitting) to green ( $R^2 = 1$ , perfect fitting), going through yellow ( $R^2 = 0.9$ , acceptable fitting). ....	67

- Figure 49. Different possible combinations of dispersion and network factor that fit the simulated composites of Figure 46 (with  $d = 0$ ,  $d = 0.5$  and  $d = 1$ ) according to the e-PvSB model. The real solutions are indicated (dashed lines). The value of  $F_{n0}$  (network factor for  $d = 0$ ) is also indicated..... 68
- Figure 50. Updated method to obtain morphological information from experimental data using the e-PvSB model. The reference network factor ( $F_{n0}$ ) includes the effects of alignment ( $a$ ), dispersion ( $d$ ) and network factor ( $F_n$ )..... 69
- Figure 51. Simulated composites with ellipsoidal fillers with different values of the alignment parameter ( $a$ ): 1, parallel to electric field (left); 1/3, random orientation (middle); and 0, perpendicular to electric field (right). ..... 69
- Figure 52. Simulated and modelled permittivity for the composite represented in Figure 51. The values of alignment (shown in the figure) and dispersion ( $d = 1$ ) were inputs to the e-PvSB model..... 70
- Figure 53. Different possible combinations of dispersion and network factor that fit the simulated composites of Figure 51 (with  $a = 1$ ,  $a = 1/3$  and  $a = 0$ ) according to the e-PvSB model. The value of  $F_{n0}$  (reference network factor) is also indicated..... 71
- Figure 54. SEM images of PLA composites with a MWNT mass concentration of 1 % and good dispersion. .... 76
- Figure 55. SEM images of PLA composites with a MWNT mass concentration of 1 % and bad dispersion. The long tubular structures observed on the bottom left corner of the image on the left are polymer structures produced during the sample fracturing. .... 76
- Figure 56. SEM images of PLA composites with a CB mass concentration of 1 % and good dispersion. .... 77
- Figure 57. SEM images of PLA composites with a CB mass concentration of 1 % and bad dispersion. .... 77
- Figure 58. TOM images of PLA composites with a MWNT mass concentration of 1 % and good dispersion: (left) original image and (right) image after computer analysis to detect agglomerates..... 78

- Figure 59. TOM images of PLA composites with a MWNT mass concentration of 1 % and bad dispersion: (left) original image and (right) image after computer analysis to detect agglomerates..... 78
- Figure 60. TOM images of PLA composites with a CB mass concentration of 1 % and good dispersion: (left) original image and (right) image after computer analysis to detect agglomerates..... 79
- Figure 61. TOM images of PLA composites with a CB mass concentration of 1 % and bad dispersion: (left) original image and (right) image after computer analysis to detect agglomerates..... 79
- Figure 62. Dielectric spectra of PLA and PLA composites with 0.1 % MWNT and 0.1 % CB mass concentrations and good dispersion. .... 80
- Figure 63. Measured permittivity of PLA composites with MWNT and CB, with good and bad dispersion, for different volume concentrations. Error bars are the standard deviation of 4 samples and are visible when the error is larger than the marker size. Lines are a visual guidance. .... 81
- Figure 64. Different possible combinations of dispersion  $d$  (vertical axis) and network factor  $F_n$  (horizontal axis) that describe the measured permittivity of the PLA/MWNT composites of Figure 63. .... 82
- Figure 65. Measured (squares) and modelled (lines) permittivity of PLA/MWNT composites, with good and bad dispersion, for different volume fractions. Error bars are the standard deviation of 4 samples and are visible when the error is larger than the marker size. .... 83
- Figure 66. Different possible combinations of dispersion (vertical axis) and network factor (horizontal axis) that describe the measured permittivity of the PLA/CB composites of Figure 63. .... 84
- Figure 67. Measured (circles) and modelled (lines) permittivity of PLA/CB composites, with good and bad dispersion, for different volume concentrations. Error bars are the standard deviation of 4 samples and are visible when the error is larger than the marker size. .... 85

Figure 68. Time evolution of permittivity and conductivity at 1 MHz of an epoxy resin with a SWNT mass concentration of 0.005 %. Different voltages were applied over a distance of 2 mm.....	88
Figure 69. Time evolution of permittivity and conductivity at 1 MHz during the curing of epoxy composites with a SWNT mass concentration of 0.005 % under 100 V (electric field treatment) and 20 mV.....	89
Figure 70. Time evolution of permittivity and conductivity at 1 MHz during the curing of epoxy without SWNTs. ....	90
Figure 71. Dielectric spectra of non-aligned composites for SWNT mass concentrations between 0.0005 % and 0.01 %. The spectra of unfilled epoxy (white) and an aligned epoxy/CB composite are also included. Data are split in two plots to visualize the different magnitudes of $\epsilon'$ (a logarithm scale would hide important features).....	91
Figure 72. Dielectric spectra of aligned composites for SWNT mass concentrations between 0.0005 % and 0.01 %. The spectrum of a composite of epoxy/MWNT (purple) after electrical treatment is also included. ....	91
Figure 73. Permittivity at 10 kHz for aligned (squares) and non-aligned (circles) epoxy/SWNT composites. Error bars are the standard deviation of 4 samples and are visible when the error is larger than the marker size. Lines are a visual guidance. ....	93
Figure 74. Conductivity at 1 Hz for aligned (squares) and non-aligned (circles) epoxy/SWNT composites. Error bars are the standard deviation of 4 samples and are visible when the error is larger than the marker size. Lines are a visual guidance. ....	94
Figure 75. Measured (squares and circles) and modelled (lines) permittivity of aligned and non-aligned composites for different volume concentrations. ....	95
Figure 76. Matrix of coefficients of determination ( $R^2$ ) of the e-PvSB model with respect to a simulated composite (Figure 46, $\mathbf{d} = \mathbf{0}$ ) for different combinations of dispersion ( $\mathbf{d}$ ) and network factor ( $\mathbf{F}_n$ ). ....	114

- Figure 77. Matrix of coefficients of determination ( $R^2$ ) of the e-PvSB model with respect to a simulated composite (Figure 46,  $d = 1$ ) for different combinations of dispersion ( $d$ ) and network factor ( $F_n$ ). ..... 115
- Figure 78. Matrix of coefficients of determination ( $R^2$ ) of the e-PvSB model with respect to PLA/MWNT composites with good dispersion for different combinations of dispersion ( $d$ ) and network factor ( $F_n$ ). ..... 115
- Figure 79. Matrix of coefficients of determination ( $R^2$ ) of the e-PvSB model with respect to PLA/MWNT composites with bad dispersion for different combinations of dispersion ( $d$ ) and network factor ( $F_n$ ). ..... 116
- Figure 80. Matrix of coefficients of determination ( $R^2$ ) of the e-PvSB model with respect to PLA/CB composites with good dispersion for different combinations of dispersion ( $d$ ) and network factor ( $F_n$ ). ..... 116
- Figure 81. Matrix of coefficients of determination ( $R^2$ ) of the e-PvSB model with respect to PLA/CB composites with bad dispersion for different combinations of dispersion ( $d$ ) and network factor ( $F_n$ ). ..... 117
- Figure 82. Conductivity spectra of two aligned composites with a significant different in DC conductivity (low-frequency limit). The values of conductivity at 1 MHz do not represent that different. .... 118
- Figure 83. Conductivity spectra of non-aligned composites for SWNT mass concentrations between 0.0005 % and 0.01 %. The spectra of unfilled epoxy (black) and an aligned epoxy/CB composite are also included. The DC conductivity cannot be determined for the samples without a low-frequency plateau. .... 118

## List of Tables

Table 1. Comparison of different experimental methods in the frame of the linear response theory [22].	6
Table 2. Relationship among the four basic immittance functions. $\mu = j\omega C_0$ with $C_0$ (empty dielectric cell's capacitance) = $\epsilon_0 A/d_e$ for a parallel plate capacitor with distance between electrodes $d_e$ and area $A$ .	8
Table 3. Depolarization factors for specific geometries.	23
Table 4. Convention for parallel and perpendicular orientation for ellipsoids of revolution, with respect to an electric field in the vertical direction.	25
Table 5. Representation of the equivalent ellipsoid and their respective value of the network factor for different networks of prolate ellipsoids ( $AR = 5$ ): (a) 8 vertical fillers in a vertical arrangement (b) 8 horizontal fillers in a vertical arrangement (c) an isolated vertical filler (d) 8 vertical fillers in a horizontal arrangement (e) 8 horizontal fillers in a horizontal arrangement. The equivalent ellipsoid of (a) is not to scale due its large aspect ratio.	61
Table 6. Representation of the equivalent ellipsoid and their respective value of the network factor for different networks of spheres: (a) 9 fillers in a vertical chain (b) 9 fillers in a vertical plane (c) an isolated filler (d) 9 fillers in a horizontal plane (e) 9 fillers in a horizontal chain.	62
Table 7. Effective ellipsoids corresponding to each degree of alignment.	71